

# Durham E-Theses

---

## *Light sheet adaptive optics microscope for 3D live imaging*

BOURGENOT, CYRIL,JULES,TUGDUAL

### How to cite:

---

BOURGENOT, CYRIL,JULES,TUGDUAL (2013) *Light sheet adaptive optics microscope for 3D live imaging*, Durham theses, Durham University. Available at Durham E-Theses Online:  
<http://etheses.dur.ac.uk/7713/>

### Use policy

---

The full-text may be used and/or reproduced, and given to third parties in any format or medium, without prior permission or charge, for personal research or study, educational, or not-for-profit purposes provided that:

- a full bibliographic reference is made to the original source
- a [link](#) is made to the metadata record in Durham E-Theses
- the full-text is not changed in any way

The full-text must not be sold in any format or medium without the formal permission of the copyright holders.

Please consult the [full Durham E-Theses policy](#) for further details.

# Light sheet adaptive optics microscope for 3D live imaging

Cyril Bourgenot

A Thesis presented for the degree of  
Doctor of Philosophy



Centre for Advanced Instrumentation  
Department of Physics  
Durham University  
England

March 2013

# **Light sheet adaptive optics microscope for 3D live imaging**

**Cyril Bourgenot**

Submitted for the degree of Doctor of Philosophy

March 2013

## **Abstract**

Optical microscopy is still the main research tool for many biological studies. Indeed with the advent of genetic manipulation and specifically, the use of fluorescent protein expressing in animals and plants it has actually seen a renaissance in the past ten years, in particular with the development of novel techniques such as CARS, PALM, STORM, STED and SPIM. In all of microscopy methods one has to look through the sample at some point. The sample thus adds an additional and uncontrolled optical path, which leads to aberrations in the final image. Adaptive optics (AO) is a way of removing these unwanted aberrations which can cause image degradation and even potentially artifacts within the image. This thesis is concerned with the implementation of AO in non scanning microscopes and presents some novel methods both in wavefront sensed and sensorless configurations. A first implementation of AO on the emission path of a light sheet microscope is also presented.

# Declaration

The work in this thesis is based on research carried out at the Centre for Advanced Instrumentation, the Department of Physics, University of Durham, England. No part of this thesis has been submitted elsewhere for any other degree or qualification and it is the sole work of the author unless referenced to the contrary in the text. All samples were used in accordance with UK Home Office rules. Some of the work presented in this thesis has been published in journals - the relevant publications are listed below.

## Publications

### Journal

- C. Bourgenot, C. D. Saunter, G. D. Love, J. M. Girkin, “Comparison of closed loop and sensorless adaptive optics in widefield optical microscopy,” *J. Eur. Opt. Soc., Rapid Publ.*, vol. 8, 2013.
- C. Bourgenot, C. D. Saunter, J. M. Taylor, J. M. Girkin, and G. D. Love, “3D adaptive optics in a light sheet microscope,” *Opt. Express*, vol. 20, pp. 13252–61, 2012.

### Conference Proceedings

- C. Bourgenot, C. D. Saunter, J. M. Girkin, and G. D. Love, “Light sheet adaptive optics microscope for 3D live imaging,” *Proc. SPIE*, vol. 8589, 2013.
- C. D. Saunter, C. Bourgenot, J. M. Girkin, and G. D. Love, “Closed loop adaptive optics with a laser guide star for biological light microscopy,” *Proc. SPIE*, vol. 8253, 2012.
- C. Bourgenot, C. D. Saunter, J. M. Girkin, and G. D. Love, “Adaptive optics for wide-field microscopy,” *Proc. SPIE*, vol. 7904, 2011.



**Copyright © 2013 by Cyril Bourgenot.**

The copyright of this thesis rests with the author. No quotation from it should be published without the prior written consent and information derived from it should be acknowledged.

# Acknowledgements

Most of all I would like to thank my supervisors John M. Girkin and Gordon D. Love for their support and guidance throughout the three and a half years work leading to this thesis. I have been inspired by their infectious and inexhaustible energy.

Many thanks also to Ray Sharples, who was my first contact here in Durham and offered me the opportunity to work in the Centre of Advance Instrumentation (CFAI). Very special thanks to Chris Saunter, whose passion and commitment for Python programming language has been very helpful, and Jonny Taylor for his stimulating discussion and ideas.

I would like to acknowledge funding from the Engineering and Physical Sciences Research Council, without which, none of this would have been possible.

A very special thank you to Amanda, for your love and support.

Finally, I would like to dedicate this doctoral thesis to my adorable and wondrous daughters, Adeline et Mélina, whose happiness and energy have been delightful diversions.

*A ma famille, je vous remercie chaleureusement pour vos encouragements et votre soutien, tant moral que gastronomique, qui a rendu la vie d'un expatrié Franc-Comtois, un peu plus douce.*

# Contents

<b>Declaration</b>	<b>iii</b>
<b>Acknowledgements</b>	<b>v</b>
<b>1 Introduction</b>	<b>1</b>
1.1 Synopsis . . . . .	4
<b>2 Theory of image formation</b>	<b>6</b>
2.1 Introduction . . . . .	6
2.2 Elements of diffraction theory . . . . .	7
2.2.1 Rayleigh-Sommerfeld Formula . . . . .	7
2.2.2 Diffraction in the Fresnel approximation . . . . .	8
2.2.3 Intensity distribution at the focus of a lens - Scalar approximation . . . . .	10
2.2.4 The vectorial approach, Richards-Wolf vector field equations	13
2.2.5 Image formation in incoherent systems . . . . .	14
2.3 Modal decomposition of the wavefront . . . . .	15
2.3.1 Zernike polynomials . . . . .	15
2.3.2 Lukosz polynomials . . . . .	17
2.4 Representation of optical quality . . . . .	19

2.4.1	PSF . . . . .	19
2.4.2	OTF . . . . .	20
2.5	Representation of image quality . . . . .	23
2.5.1	Metrics used in focusing techniques . . . . .	24
2.5.2	Metrics used in AO systems with extended object optimi- sation . . . . .	30
<b>3</b>	<b>AO techniques applied to microscopy</b>	<b>33</b>
3.1	Source of image degradation in microscopy . . . . .	34
3.1.1	The out-of-focus parts of the sample . . . . .	34
3.1.2	Aberrations in microscopy . . . . .	36
3.2	Adaptive optics in microscopy . . . . .	41
3.2.1	Active phase optical elements for wavefront shaping . . .	42
3.2.2	Direct wavefront sensing . . . . .	46
3.2.3	Sensorless adaptive optics . . . . .	52
<b>4</b>	<b>AO Brightfield transmission microscope</b>	<b>61</b>
4.1	Introduction . . . . .	61
4.1.1	Test images . . . . .	62
4.1.2	Image sharpness metric . . . . .	63
4.2	Analysis and comparison of the metrics with simulation . . . . .	65
4.2.1	Metrics as a function of blur level . . . . .	66
4.2.2	Metrics as a function of image content . . . . .	67
4.2.3	Metrics as a function of noise . . . . .	71
4.3	Experimental comparison of the 5 sharpness metric . . . . .	77
4.3.1	Optical setup . . . . .	77
4.3.2	Simplex optimisation configurations . . . . .	78
4.3.3	Measurement of the metric relative improvement . . . . .	81

4.3.4	Comparison of optimisation performances for different metrics . . . . .	84
<b>5</b>	<b>Closed loop widefield microscope</b>	<b>88</b>
5.1	Introduction . . . . .	88
5.1.1	The double path effect . . . . .	90
5.1.2	Ghost reflection reduction . . . . .	92
5.1.3	Speckle wavefront sensor spots reduction . . . . .	94
5.2	Optical configuration . . . . .	95
5.2.1	Simulation of the effect of the confocal pinhole . . . . .	97
5.2.2	Improving spot motion measurement using correlation centroiding . . . . .	100
5.3	Experiment description . . . . .	101
5.3.1	Results . . . . .	102
5.3.2	Comparison of sensed and sensorless configuration . . .	104
5.3.3	Conclusion . . . . .	108
<b>6</b>	<b>Adaptive optics SPIM</b>	<b>109</b>
6.1	Introduction . . . . .	109
6.2	Source of aberration in a SPIM . . . . .	112
6.2.1	Astigmatism induced by the sample holder . . . . .	116
6.2.2	Defocus induced by the sample holder . . . . .	117
6.3	Experimental set-up . . . . .	120
6.4	Aberration measurement using fluorescent beads in a glass pipette	122
6.5	Experimental results . . . . .	125
6.5.1	Aberration correction in zebrafish placed in a glass pipette	125
6.5.2	Aberration correction in zebrafish when placed in an index-matched polymer tube . . . . .	128

6.6	Dynamic correction of aberration in a live zebrafish heart . . . .	131
6.6.1	Implementation . . . . .	132
6.6.2	Metric sensitivity to image variation . . . . .	133
6.6.3	Results . . . . .	136
6.7	Conclusion . . . . .	139
<b>7</b>	<b>Conclusion</b>	<b>141</b>
7.1	Summary . . . . .	141
7.2	Future work . . . . .	143
7.2.1	Implementation of AO on the illumination path of a SPIM	143
7.2.2	the combined use of structured illumination with AO . . .	146
7.2.3	Shadow reduction with a static optical device . . . . .	149
7.2.4	A reversible SPIM . . . . .	150
7.2.5	The use of the light sheet to create a localised artificial guide star for direct wavefront sensing . . . . .	150
	<b>Annexes</b>	<b>153</b>
	<b>A Step by step simplex optimisation in a 2D configuration</b>	<b>154</b>
	<b>Bibliography</b>	<b>157</b>

# List of Figures

2.1	Diffraction at an aperture in a plane screen . . . . .	9
2.2	Wavefront corrector in a 2f configuration. . . . .	11
2.3	first 15 Zernike modes with the dual indexation . . . . .	16
2.4	12 Lukosz polynomials (4-15). . . . .	19
2.5	Simulated lateral and axial normalised PSF of an aberration-free and aberrated system. . . . .	20
2.6	Comparison of the aberration free and aberrated MTF. . . . .	22
2.7	Blur effect on the histogram . . . . .	26
2.8	Illustration of the metric based on the energy of the image gradient	27
2.9	Principle of a 2D Haar wavelet decomposition . . . . .	28
2.10	Example of the effect of multiple decomposition on a 1D spectrum	29
3.1	Refractive index mismatch at a planar interface ( $n_2 < n_1$ ). . . . .	37
3.2	Aberrations caused by a refractive index mismatch at a planar interface . . . . .	39
3.3	Sample holder techniques used in light sheet microscopy. Picture explained in the text. . . . .	41
3.4	Electrostatic membrane technology . . . . .	43
3.5	Magnetic continuous membrane . . . . .	44

3.6	Piezoelectric DM technology . . . . .	45
3.7	MEMS technology . . . . .	45
3.8	Direct wavefront sensing configurations . . . . .	47
3.9	Shack-Hartmann wavefront sensor, sensing a plane wave (top) and an aberrated wave (bottom) . . . . .	48
3.10	Wavefront sensor modal reconstruction . . . . .	49
3.11	phase retrieval simulation example. . . . .	54
3.12	Simplex algorithm organisation chart. The best value corre- sponds here to a minimum. . . . .	56
3.13	Simulation of a modal simplex optimisation . . . . .	58
3.14	Simulation of a modal PN optimisation . . . . .	60
4.1	Images used in the simulation . . . . .	64
4.2	Sharpness metric variation with level of defocus. . . . .	68
4.3	Sharpness metric variation with image content . . . . .	69
4.4	metric dispersion with image content, as per eq. (4.1), as a func- tion of PSF RMS radius . . . . .	70
4.5	Blur and Noise effect on the image histogram. . . . .	73
4.6	Effect of Noise on the image sharpness metric . . . . .	74
4.7	Sensitivity to blur, in presence of noise, assessed in Figures 4.6(a) to 4.6(e). . . . .	76
4.8	A wavefront sensorless AO transmission microscope with a bright- field illumination. . . . .	78
4.9	Before and after images . . . . .	80
4.10	Comparison of different optimisation scheme based on the sim- plex algorithm using the standard deviation metric . . . . .	82
4.11	Optimised wavefront map and modal coefficients . . . . .	82
4.12	metric relative improvement comparison for the 5 different metrics	83



4.13 Typical Before and after image . . . . .	84
4.14 Comparison of metric relative improvement . . . . .	85
4.15 Zernike modal coefficient per metrics . . . . .	86
4.16 Before and after optimisation profiles . . . . .	87
5.1 Principle of the double path effect occurring in the case of a reflected focused beam . . . . .	92
5.2 Illustration of the use of the back scattering light as a laser guide star for wavefront sensing . . . . .	93
5.3 Ghost reflection reduction methods . . . . .	94
5.4 Closed-loop AO transmission microscope . . . . .	95
5.5 Effect on a wave phase and intensity by a $850\ \mu m$ pinhole . . . . .	99
5.6 Effect of the confocal pinhole on the WFS spot . . . . .	100
5.7 Image of the sample used in the experiment . . . . .	102
5.8 Closed-loop stability check . . . . .	103
5.9 Metric value and RMS wavefront recorded during the closed-loop	104
5.10 Optimised images comparison between sensed and sensorless configurations . . . . .	105
5.11 Sensed and sensorless configurations optimisation speed com- parison . . . . .	105
5.12 Astronomy and microscopy spot elongation effect analogy . . . . .	107
6.1 Principle of SPIM . . . . .	111
6.2 Tube geometry used to hold the zebrafish. . . . .	113
6.3 Aberration created at the centre of the cylindrical tube . . . . .	114
6.4 Optical and mechanical parameters contributing to the SPIM aberrations . . . . .	115
6.5 Variation of astigmatism in the tube . . . . .	117

6.6	Variation of astigmatism with the tube parameters . . . . .	118
6.7	Variation of defocus in the tube . . . . .	119
6.8	Variation of defocus with the tube parameter . . . . .	121
6.9	Optical Configuration showing the AO SPIM . . . . .	121
6.10	Typical optimisation of the image of the beads in a borosilicate tube . . . . .	123
6.11	Variation of the metric during the 4 optimisation runs . . . . .	123
6.12	Comparison of measured and simulated defocus and astigmatism with depth . . . . .	124
6.13	Optimisation on zebrafish in a glass borosilicate pipette . . . . .	126
6.14	Comparison of the normalised metric variation with depth in a borosilicate tube . . . . .	127
6.15	Zernike mode amplitude at different depth . . . . .	128
6.16	Optimisation on zebrafish in a refractive index matching FEP mounting tube . . . . .	129
6.17	Comparison of the normalised metric variation with depth in a borosilicate tube . . . . .	130
6.18	Zernike mode amplitude at different depths in the FEP tube . . .	130
6.19	Example of normalised metric variation with or without synchro- nisation . . . . .	133
6.20	Heart synchronisation module in association with AO . . . . .	134
6.21	Statistical analysis of the modal coefficient over 101 runs . . . . .	135
6.22	Live heart AO optimisation with synchronisation when imaged in a glass tube. . . . .	137
6.23	Live heart AO optimisation with synchronisation when imaged in a FEP tube . . . . .	138
7.1	Solution for high lateral and axial resolution on SPIM . . . . .	145

7.2	Tip and tilt correction of the illumination . . . . .	147
7.3	implementation of HiLo on a non-scanning light sheet microscope	148
7.4	Reversible SPIM . . . . .	151
7.5	Suggestion of direct wavefront sensing in a SPIM . . . . .	151

# List of Tables

4.1	Metrics used in the simulation and experimental part of this chapter. . . . .	66
6.1	Modal amplitude standard deviation measured in Figure 6.21 for the 5 selected metrics. . . . .	134

# Chapter 1

## Introduction

Optical microscopy and astronomy have always played a leading role in the development of optical systems and this tradition continues to this day. In both fields the ultimate diffraction limit of an imaging system is rarely reached as aberrations in the optical system perturb the image. Generally in modern systems these aberrations are neither due to the optical components nor their alignment, being instead induced by the medium through which the instrument has to operate. In the case of astronomy this is the atmosphere, and in the case of optical microscopy the sample through which you are imaging. In both classes of instrument the optical paths contain changes in the local refractive index of the material, which affects the light path and wavefront of the light reaching the detector leading to a loss of spatial resolution and contrast in the image. In microscopy these wavefront aberrations become more significant with depth into the sample, limiting high resolution imaging to shallow depths.

Over the last ten years there has been significant growth in the development and application of adaptive optics methods within optical microscopy to overcome these limitations on the imaging depth and resolution in biological samples. This

interest has partly been fuelled by the development of novel optical microscopy methods, but also in the significant reduction in cost of adaptive optical elements such that they are no longer only within reach of highly funded optical telescopes. The challenge of improved imaging in microscopy, although having clear similarities with astronomical observations, also has a number of significant differences. Crucially in the astronomical case the aberrations are rapidly time varying whereas in most microscopy cases, even for in vivo imaging, the sample variations change less rapidly in time. Thus in the field of microscopy the main route being followed uses an optimisation methodology based upon an image metric, rather than actually sampling the aberrations within the sample in real time, as is generally done in astronomy. This thesis is concerned with the implementation of adaptive optics in microscopy, and both methods (image or wavefront sensing based optimisation) are addressed throughout the chapters. The work presented here, although involving a large variety of techniques and different type of microscopes, has a common theme which is the implementation of AO techniques into non scanning point systems for the optimisation on extended objects.

The research described in this thesis contains the following key results:

1. A numerical and experimental analysis of 5 different metrics when used on typical microscope images, shows that sharpness metrics present a different degree of sensitivity to aberration, noise, and image content. This is confirmed in the experiment chapter 4.
2. The convergence of a Nelder-Mead simplex optimisation algorithm in a sensorless AO set-up can be sped up when (chapter 4):
  - The aberration is expressed as a set of modes and when a limited number of modes is used as the optimisation variables, rather than

the mirror actuators.

- the starting point of the optimisation is approximated with an aberration composed of low order modes with random amplitude.
3. when low order aberration affects an image composed of simple feature, the choice of the metric does not appear to be critical, and optimisation performed with different metrics leads to the same optimised image (chapter 4).
  4. In a closed loop AO system, backscattered light from the sample can be used as an artificial guide star. Depth discrimination is achieved with the help of a confocal pinhole placed in front of the wavefront sensor. The use of an independent laser probe for the guide star generation, allows its positioning anywhere in the field of view (assuming the observed region of the sample presents enough backscattered light) affording a larger flexibility compared to other techniques such as fluorescent beads (chapter 5).
  5. The use of image optimisation to define the null position for the wavefront sensor, allows a calibration in situ without the need to remove the sample (chapter 5).
  6. The comparison of sensorless and wavefront sensed AO configuration on the same sample images has been performed (chapter 5).
  7. The use of modal sensorless AO on the imaging path of a light sheet microscope, demonstrates the improvements in image quality whilst recording a 3D z-stack on an ex-vivo zebrafish (chapter 6).
  8. The dynamic correction of aberrations in a live zebrafish heart has been demonstrated using modal sensorless AO with the help of real-time heart synchronisation techniques, which allow a controlled image acquisition at a specific position in the heart cycle (chapter 6).

9. A numerical and experimental analysis of aberration created by a glass tube has been performed, which shows that defocus and astigmatism are the main contributors and, in particular, that distortion effects of the light sheet contribute to defocus on the imaging path (chapter 6).

## 1.1 Synopsis

This thesis is presented in the following way:

- Chapter 2 summarises the theoretical background behind the mechanism of image formation, which is necessary to understand the effect of wavefront correction on the image. The representation of optical and image quality are discussed and the concept of image sharpness metric is introduced. Zernike and Lukosz polynomials which are at the heart of the modal optimisation scheme are also defined.
- Chapter 3 describes the cause of aberration in microscopy, and presents different AO methods implemented for their correction. We give a summary of the deformable mirror technologies available, and discuss the sensed and sensorless approach. In the sensed method discussion, we describe the Shack-Hartmann wavefront sensor and, explain the wavefront reconstruction as well as the the control technique used later in the experimental part in chapter 4. Finally, on the sensorless subject, we limit our description to algorithms later used in the thesis: the Nelder-Mead algorithm (used in Chapter 3 and 4) and the PN modal algorithm (used in chapter 5).
- Chapter 4 numerically and experimentally compares 5 different image metrics when applied to images with various levels of aberration, noise and structure. The experimental part describes a brightfield transmission AO



microscope, and the 5 metrics are compared using a sensorless approach based on the Nelder-Mead simplex algorithm.

- Chapter 5 presents a closed-loop sensed version of the brightfield transmission microscope described in the previous chapter. Backscattered light from the sample is used as an artificial guide star to provide a feedback signal to the wavefront corrector. The depth discrimination is achieved with the help of a confocal pinhole. A simulation on the effect of this pinhole on the phase and amplitude of the wave is given, and assesses the limitation of AO correction for this particular set-up. Finally, the sensed and sensorless approach are compared, and advantages and limitations in both cases are discussed.
- Chapter 6 reports on the use of AO applied onto the imaging path of a single plane illumination microscope (SPIM), demonstrating significant improvement in the image quality of a live GFP-labelled transgenic zebrafish embryo heart using a modal, wavefront sensorless approach and a heart synchronisation method. These experimental results are linked to a computational model showing that significant aberrations are produced by the tube holding the sample in addition to the aberration from the biological sample itself.

## Chapter 2

# Theory of image formation

### 2.1 Introduction

It is universally recognised that the fundamental limit in imaging systems is diffraction. In microscopy, both lateral and axial resolutions are of significant importance and aimed to be diffraction limited. However, when imaging in most of the biological samples, especially deep samples, sample-induced aberrations deteriorate, often critically, the system's performances. The use of Adaptive Optics (AO) offers a way of restoring the optimal image quality by correcting this distortion. The aim of adaptive optics is to improve the image quality of optical systems and get as close as possible to the diffraction limit, by correcting the wavefront distortion.

This chapter provides some of the theoretical tools, which describe the mathematical transformations from the corrector (in essence, the deformable mirror (DM)) to the image plane at the focus of the microscope objective. It is not meant to be extensive and the reader will be directed to some references for more details about the theory. The aim is to supply the theoretical basis, which

will be used throughout the thesis. This chapter is divided into four parts.

The first part summarises the theoretical background behind the mechanism of image formation in the presence of a wavefront corrector. In particular, we compute the image intensity of a point source for a monochromatic illumination at the focus of a lens for a given phase aberration and discuss the case of extended objects. The second part describes two ways of expressing the phase aberration using convenient orthogonal polynomial sets (Zernike and Lukosz). These 2 polynomial sets will be repeatedly employed in the subsequent chapters. The third part details the quantities used to represent system optical quality. With optical quality criteria defined, we will then discuss the image quality criteria in the fourth part, and the different ways of measuring them. In particular, the concept of image sharpness metric will be introduced.

## 2.2 Elements of diffraction theory

### 2.2.1 Rayleigh-Sommerfeld Formula

Huygens in 1690, suggested a model based on wave theory to describe light propagation. He stated in his *Traité de la lumière* [1], that: *"each element of a wave-front may be regarded as the centre of a secondary disturbance which gives rise to spherical wavelets."* and that *"the position of the wave-front at any later time is the envelope of all such wavelets."* However, at the time it was stated, this model was not able to describe diffraction effects. Later, in 1816, Fresnel supplemented Huygens' construction by specifying that the secondary wavelets were mutually interfering leading to diffraction patterns at the observation plane. This has become known as the Huygens-Fresnel principle, and it has been regarded as the cornerstone of wave theory.

The analytical description of diffraction effects was pushed a step further, when

Kirchhoff suggested a mathematical review of the Huygens-Fresnel principle. From the Green theorem and the wave equation, Kirchhoff derived the Fresnel-Kirchhoff integral theorem(1882) and with few assumptions, established an expression of the diffracted field named as the Fresnel-Kirchhoff diffraction formula [2]. However, even if the use of this model has shown accurate predictions in accordance with the experiments, it relies on mathematical inconsistencies, which prompted physicists to improve the model.

Sommerfeld derived a diffraction integral from the Fresnel-Kirchhoff integral theorem, which removed the mathematical ambiguities encountered by the Fresnel-Kirchhoff diffraction formula,

$$U(P) = -\frac{i}{\lambda} \iint_S U(P') \frac{e^{ikP'P}}{P'P} \cos(\vec{n}, \overrightarrow{P'P}) ds, \quad (2.1)$$

where  $U$  is the scalar complex field,  $k = \frac{2\pi}{\lambda}$ ,  $\vec{n}$  is the normal to the diffractive aperture and is pointing in the opposite direction of  $P$ .  $P'$  is a point located on the aperture,  $P$  is the point where the field amplitude is calculated as shown on Figure 2.1, and  $S$  is the area of the aperture opening. The integral gives the value of the complex amplitude at  $P$ , as a function only dependent on the amplitude at  $P'$ .

### 2.2.2 Diffraction in the Fresnel approximation

From the formula 2.1, several approximations can be made, which lead to a much simpler expression. The first one consists in approximating the cosine to 1 in Eq. 2.1. It is justified in [3] by the fact that Eq. 2.1 is based on the scalar theory of wave, which inherently considers small angles of diffraction.

The second approximation is made on the evaluation of  $P'P$ , as shown on Figure 2.1. The distance  $P'P$  can be expressed as a function of  $P'$  and  $P$  coordinates

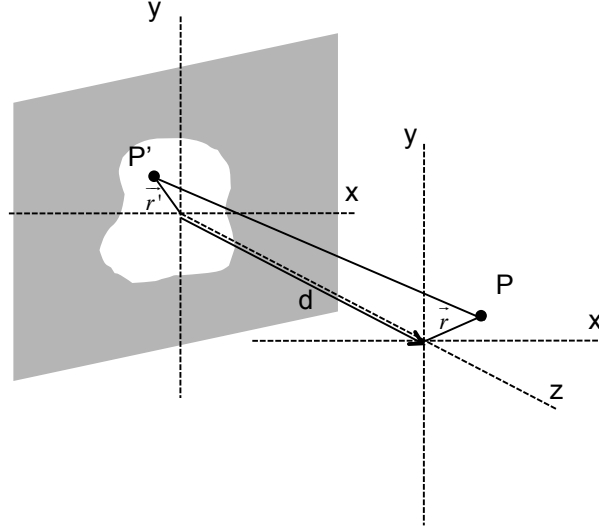


Figure 2.1: Diffraction at an aperture in a plane screen

respectively  $(x', y', 0)$  and  $(x, y, d)$ , so

$$P'P = \sqrt{(x - x')^2 + (y - y')^2 + d^2},$$

$$P'P = d\sqrt{1 + \frac{r^2}{d^2} + \frac{r'^2}{d^2} - 2\frac{xx' + yy'}{d^2}}, \quad (2.2)$$

with  $r^2 = x^2 + y^2$  and  $r'^2 = x'^2 + y'^2$ .

The Eq. 2.2 is expanded as

$$P'P = d\left(1 + \frac{r^2}{2d^2} + \frac{r'^2}{2d^2} - \frac{xx' + yy'}{d^2} + \epsilon\right),$$

with  $\epsilon$  being the high order terms of the binomial expansion of the square root in Eq. 2.2. Under the Fresnel diffraction regime, the  $\epsilon$  term is very small and is omitted<sup>1</sup>. With this approximation, the Rayleigh-Sommerfeld diffraction

---

<sup>1</sup>It is easy to show that this assumption is valid if and only if  $\frac{(r^2 - r'^2)^2}{\lambda d^3} \ll 1$  which is true if:  $\sqrt{r^2 - r'^2} \ll d$ ,  $\lambda \ll d$ , and  $\sqrt{r^2 - r'^2} \gg \lambda$ . All following experiments and simulations

integral becomes:

$$U(x, y, d) = -\frac{i}{\lambda d} U_0 e^{ik \frac{r^2}{2d}} \int_{-\infty}^{+\infty} \int U(x', y', 0) e^{ik \frac{r'^2}{2d}} e^{-ik \frac{xx' + yy'}{d}} dx' dy'. \quad (2.3)$$

The finite limit of the aperture has been incorporated in the definition of  $U(x', y', 0)$  and the integral boundaries have been extended to  $-\infty$  and  $+\infty$ . As a result, the integral 2.3 can be expressed in the form of a Fourier Transform:

$$U(x, y, d) = -i\lambda d U_0 e^{ik \frac{r^2}{2d}} \mathcal{F} \left\{ U(\mu, \eta, 0) e^{i\pi\lambda d(\mu^2 + \eta^2)} \right\}, \quad (2.4)$$

where  $\mu$  and  $\eta$  are respectively  $\frac{x'}{\lambda d}$  and  $\frac{y'}{\lambda d}$ .

In the next section, we will compute the amplitude at the focus of a lens in a "2f configuration" for a given incoming wavefront at the pupil plane.

### 2.2.3 Intensity distribution at the focus of a lens - Scalar approximation

In this section, we calculate the intensity distribution at the focus of the lens when a specific wavefront is generated by a wavefront corrector (a deformable mirror (DM) for example) placed at a distance  $d$  from the lens. The optical configuration is represented in Fig. 2.2. The wavefront corrector is placed in the plane  $\Sigma_{DM}$  and the lens is in the plane  $\Sigma_L$ . The image is made in the plane  $\Sigma_I$ . The distance between  $\Sigma_{DM}$  and  $\Sigma_L$  is  $d$ , and is  $f$  between  $\Sigma_L$  and  $\Sigma_I$ .

We consider in this configuration, that the diameter of the lens is large enough to avoid vignetting effects in the field of view. If we define the phase function created by the DM as  $\Phi_{DM}$  and the pupil function of the system as  $P(x', y')$  ( $=1$  in the aperture and  $=0$  elsewhere), then the complex amplitude of  $\overline{\phantom{x}}$  will be done under this approximation.

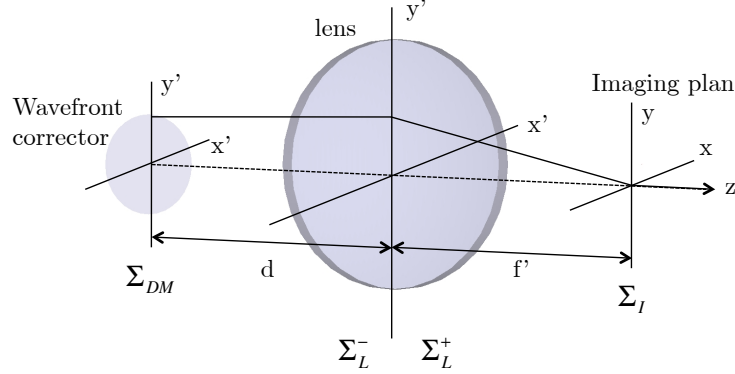


Figure 2.2: Wavefront corrector in a 2f configuration.

a normal incidence monochromatic plane wave after reflection on the DM is

$$U_{\Sigma_{DM}}(x', y') = U_0 P(x', y') e^{ik\Phi_{DM}}. \quad (2.5)$$

The amplitude of the field at the focus of the lens is [3]:

$$U_{\Sigma_I}(x, y) = A \frac{e^{i \frac{k}{2f'} \left(1 - \frac{d}{f'}\right) (x^2 + y^2)}}{i\lambda f'} \iint_{-\infty}^{+\infty} U_{\Sigma_{DM}}(x', y') e^{-i \frac{2\pi}{\lambda f'} (xx' + yy')} dx' dy'. \quad (2.6)$$

Preferably, we will consider 2f configuration ( $d = f'$ ), where the DM is placed at the distance  $f'$  of the lens. In such a configuration, the quadratic phase in the first exponential of Eq. 2.6 is cancelled, which gives a simpler expression. Furthermore, as the DM is placed at the distance  $f'$  of the lens, the system is telecentric which offers the advantage of magnification invariance with defocus.

The field amplitude at the imaging plane of a system for a point source, is also called the amplitude point spread function and is defined, for the system

described on Fig 2.2, by

$$h(x, y) = U_{\Sigma_I}(x, y) = \frac{A}{i\lambda f'} \iint_{-\infty}^{+\infty} U_{\Sigma_{DM}}(x', y') e^{-i\frac{2\pi}{\lambda f'}(xx' + yy')} dx' dy', \quad (2.7)$$

$$h(x, y) = -iAU_0\lambda f' \mathcal{F}\{Pe^{ik\Phi_{DM}}\}.$$

With the change of variable so  $(\mu, \eta) = (\frac{x'}{\lambda f'}, \frac{y'}{\lambda f'})$ , the amplitude point spread function of the system clearly appears to be the Fourier transform of the wave amplitude after reflection on the DM.

In the following, we will limit our discussion to incoherent illumination systems and will be interested in obtaining an expression of the intensity. The intensity at the focus of the lens is given by the modulus squared of the amplitude point spread function:

$$I_{\Sigma_I}(x, y) = |h(x, y)|^2 = h(x, y)h^*(x, y), \quad (2.8)$$

where  $h^*$  is the conjugate of  $h$ .

We have seen in this section that a phase corrector working in a 2f configuration, is an ideal optical configuration. It has the advantage of being telecentric (i.e. image size invariant with defocus), and the calculation of the diffraction pattern is just the Fourier transform of the product of the pupil function and the phase function created by the phase corrector. This result is valid under the regime of the scalar diffraction. The next section broaches the more general vectorial diffraction theory and gives an analytical formulation of the optical field at the focus of a high NA microscope objective for an unpolarised input beam.



### 2.2.4 The vectorial approach, Richards-Wolf vector field equations

We mention here this analysis by Richards and Wolf [4], here, with the view to extend our discussion and refer to a more complete (but also more complex) diffraction model. This model is, in fact not limited to the small angle approximation (scalar theory) but is valid for all angles in the imaging plane (up to 90 degree) and also takes into account the linear polarisation of the incoming wave. We will limit our discussion here, to an unpolarised incoming wave (which will be the case throughout this document), so the electric field is integrated over all possible polarisation orientations. The time average energy density for a point P, located at the object plane of a high NA microscope objective, when the incoming wave is unpolarised:

$$I(u, v) = \frac{A^2}{16\pi} \{ |I_0|^2 + 2|I_1|^2 + |I_2|^2 \}, \quad (2.9)$$

with:

$$I_0(u, v) = \int_0^\alpha \cos^{\frac{1}{2}} \theta \sin \theta (1 + \cos \theta) J_0 \left( \frac{v \sin \theta}{\sin \alpha} \right) e^{iu \cos \theta / \sin^2 \alpha} d\theta,$$

$$I_1(u, v) = \int_0^\alpha \cos^{\frac{1}{2}} \theta \sin^2 \theta J_1 \left( \frac{v \sin \theta}{\sin \alpha} \right) e^{iu \cos \theta / \sin^2 \alpha} d\theta,$$

$$I_2(u, v) = \int_0^\alpha \cos^{\frac{1}{2}} \theta \sin \theta (1 - \cos \theta) J_2 \left( \frac{v \sin \theta}{\sin \alpha} \right) e^{iu \cos \theta / \sin^2 \alpha} d\theta.$$

$A = \frac{\pi f l_0}{\lambda}$  is a constant,  $f$  is the focal length, and  $l_0$  is the incoming wave amplitude.  $J_0, J_1, J_2$  are respectively the Bessel function of the first kind and order 0, 1, 2,  $\alpha$  is angular semi-aperture on the image side, and  $u, v$  the optical

coordinate such that:

$$u = kz \sin^2 \alpha,$$

$$v = k\sqrt{x^2 + y^2} \sin \alpha.$$

In the following, the scalar approximation will be used for the calculation of the PSF shape at the focus of the microscope objective. For all types of microscope considered in this work, the imaging beam will be unpolarised. The minor residual difference in PSF shape computed with the scalar and the vectorial model in the case of an unpolarised beam is small enough to justify the use of the scalar theory [4, 3, 5].

### 2.2.5 Image formation in incoherent systems

In incoherent illumination systems such as conventional microscopy, the image is obtained with the intensity convolution integral [3]:

$$\begin{aligned} I_i(x, y) &= \iint_{-\infty}^{+\infty} |h(x - \mu, y - \eta)|^2 I_g(\mu, \eta) d\mu d\eta, \\ I_i(x, y) &= PSF * I_g(x, y), \end{aligned} \tag{2.10}$$

where  $h(x, y)$  is the amplitude point spread function system corresponding to the expression 2.7 in the case of the AO system working in a 2f configuration. The quantity  $|h(x, y)|^2$ , is the intensity point spread function, is also defined as the Point spread function (PSF).  $I_g(x, y)$  is the ideal image intensity produced by the magnification of the optical system.  $I_i(x, y)$  is the image intensity at the imaging plane.

## 2.3 Modal decomposition of the wavefront

In this section, we discuss how the wavefront can be decomposed as a sum of individual functions called modes. This is particularly interesting in AO, where a system with  $N$  variables ( $N$  being the number of mirror actuators) can be finally reduced and approximated to  $M$  variables ( $M$  being the number of modes, with  $M < N$ ). Here, we will discuss the advantage of using two types of decomposition: The Zernike polynomials in section 2.3.1 and the Lukosz polynomials 2.3.2.

### 2.3.1 Zernike polynomials

The Zernike polynomials are a set of orthogonal functions defined on the unit circle used to describe the wavefront for systems with circular aperture. The wavefront is expressed as

$$\Phi(\rho, \theta) = \sum_{j=0}^{+\infty} a_j Z_j(\rho, \theta),$$

where  $a_j$  is the mode amplitude, and  $Z_j$  is the mode function. The mode indexation can be done in 2 ways either using the dual index  $(n, m)$  or using the single index  $j$ . They are a convenient way of describing aberrations in optical systems. First proposed by Zernike in 1934, they were reformulated in 1976 by Noll [6] so, for each mode, the mean is zero and the variance is minimal and normalised to 1. For a wavefront expressed with  $N$  modes, the total wavefront variance is easily calculated:

$$\sigma^2 = \sum_{j=0}^N a_j^2.$$

The mode functions are defined (according to the dual index  $(n, m)$ ) by:

$$Z_n^m(\rho, \theta) = \begin{cases} \sqrt{n+1}R_n^m(\rho)\sqrt{2}\cos m\theta & \text{for } m > 0 \\ \sqrt{n+1}R_n^{|m|}(\rho)\sqrt{2}\sin |m|\theta & \text{for } m < 0 \\ \sqrt{n+1}R_n^0(\rho) & \text{for } m = 0, \end{cases} \quad (2.11)$$

for value of  $n$  and  $m$  always integral, and satisfying:  $|m| \leq n$  and  $n - m = \text{even}$ .

$R_n^m$  is the radial component:

$$R_n^m(\rho) = \sum_{s=0}^{\frac{n-m}{2}} \frac{(-1)^s (n-s)!}{s! \left[\frac{n+m}{2} - s\right]! \left[\frac{n-m}{2} - s\right]!} \rho^{n-2s}. \quad (2.12)$$

The Figure 2.3, gives a representation of the first 15 Zernike modes, with both indexations.

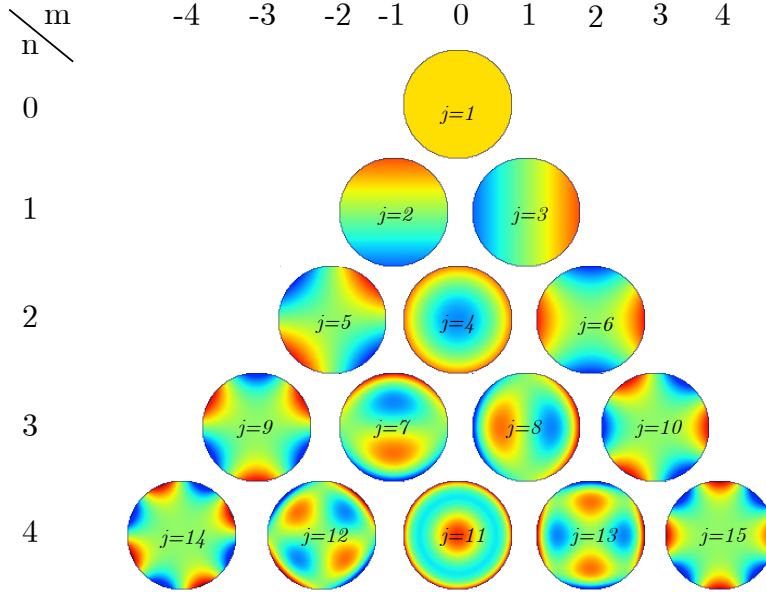


Figure 2.3: first 15 Zernike modes with the dual indexation

Zernike modes are orthogonal according to the inner product relation:

$$\frac{1}{\pi} \iint P(\rho) Z_{j_1} Z_{j_2} \rho d\rho d\theta = \delta_{j_1 j_2},$$

where  $\delta_{j_1 j_2}$  is the Kronecker symbol and  $P(\rho)$  is the pupil function ( $P = 1$  in the aperture and  $P = 0$  elsewhere).

### 2.3.2 Lukosz polynomials

The Lukosz polynomials were first derived by Lukosz [7] in 1963 and later independently by Braat [8], are a complementary to the Zernike polynomials to describe aberrations in an optical system with a circular aperture. The wavefront is expressed as

$$\Phi(\rho, \theta) = \sum_{j=2}^{\infty} b_j L_j(\rho, \theta),$$

where  $b_j$  is the mode amplitude,  $L_j$  is the mode function, and  $j$  is the same index as for the Zernike polynomial. We have seen in the section 2.3.1, that each Zernike mode is contributing independently to the wavefront variance. In the case of the Lukosz polynomial, each mode contributes independently to the rms transverse aberration. The rms spot radius  $\epsilon_r$  is defined in [9]:

$$\epsilon_r^2 = 2 \left( \langle x_e - \langle x_e \rangle^2 \rangle + \langle y_e - \langle y_e \rangle^2 \rangle \right),$$

where  $x_e$  and  $y_e$  are the transverse aberrations along x and y axis:

$$\begin{aligned} x_e &= -\frac{\lambda}{NA} \frac{\partial W(x, y)}{\partial x}, \\ y_e &= -\frac{\lambda}{NA} \frac{\partial W(x, y)}{\partial y}. \end{aligned} \tag{2.13}$$

$NA$  is the numerical aperture,  $\lambda$  the wavelength and  $W$  is the phase aberration.

The advantage of using such modes for the description of aberration in an

optical system is that, as orthogonalizing the transverse aberration, they are ideal to study the transition from physical to geometrical optics when large aberrations are present. Because the transverse aberrations as expressed in the eq. (2.13), do not take into account diffraction effects, the use of these modes have to be restricted to severe aberrations regime.

For a wavefront expressed with a set of Lukosz polynomials, the rms spot radius in the image plane can then be calculated with the sum of the amplitude of the modes:

$$\epsilon_r^2 = \left( \frac{\lambda}{NA} \right)^2 \sum_i b_i^2.$$

The Lukosz mode functions (defined with the dual index  $(n, m)$ ) are [10]:

$$L_n^m(\rho, \theta) = B_n^m(\rho) \begin{cases} \cos(m\theta) & m \geq 0 \\ \sin(m\theta) & m < 0, \end{cases}$$

with

$$B_n^m(\rho) = \begin{cases} \frac{1}{2\sqrt{n}} [R_n^0(\rho) - R_{n-2}^0(\rho)] & \text{for } n \neq m = 0 \\ \frac{1}{\sqrt{2n}} [R_n^m(\rho) - R_{n-2}^m(\rho)] & \text{for } n \neq m \neq 0 \\ \frac{1}{\sqrt{n}} R_n^m(\rho) & \text{for } m = n \neq 0 \\ 1 & \text{for } m = n = 0. \end{cases} \quad (2.14)$$

Figure 2.4, gives a representation of 12 Lukosz modes (4-15). The piston, tip and tilt modes which respectively correspond to the indexes:  $(0, 0)$ ,  $(1, -1)$  and  $(1, 1)$  have no effect on the geometrical spot radius and hence are not displayed.

In the next section, we will define the parameters used for the description of optical quality.

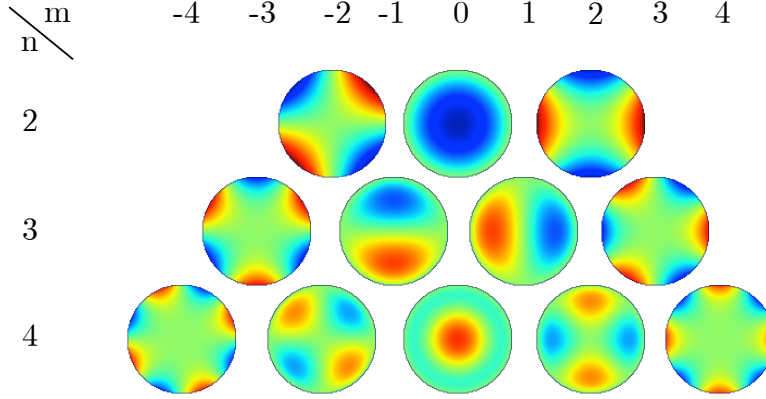


Figure 2.4: 12 Lukosz polynomials (4-15).

## 2.4 Representation of optical quality

### 2.4.1 PSF

The Point Spread Function (PSF) is the response of an imaging system to a point source or point object. In an imaging system, the PSF is a direct representation of the optical quality. In microscopy, and in particular optical sectioning microscopy, both the lateral and axial PSF are of interest. For example, in optical sectioning epi-illumination microscopy such as confocal or 2 photon, the length along the optical axis of the PSF defines the thickness of the section. In an aberration free system with a circular aperture and uniform amplitude, the PSF in the imaging plane is an Airy disk as displayed in Fig 2.5(a). The diameter of the first dark ring is the usual criterion defining the resolution and is  $\phi_A = 2.44 \frac{\lambda}{2NA}$  where  $NA$  is the numerical aperture of the beam and  $\lambda$  the wavelength. The Fig. 2.5(b) is the axial section of the Airy disc. In a non aberrated widefield system, the axial resolution is given by the elongation of the Airy disc along the optical axis. This longitudinal dimension, again defined by the distance between the two points of first zero intensity, is given by  $\Delta_A = \frac{4\lambda}{NA^2}$ .

Fig 2.5(c) and 2.5(d) are respectively the lateral and axial PSF of the same system in presence of aberrations (0.94 radians of spherical aberration and coma). In the computer generated example, the system is limited by a circular aperture of diameter 2mm with a focal length of 128mm, and the wavelength is 500nm.

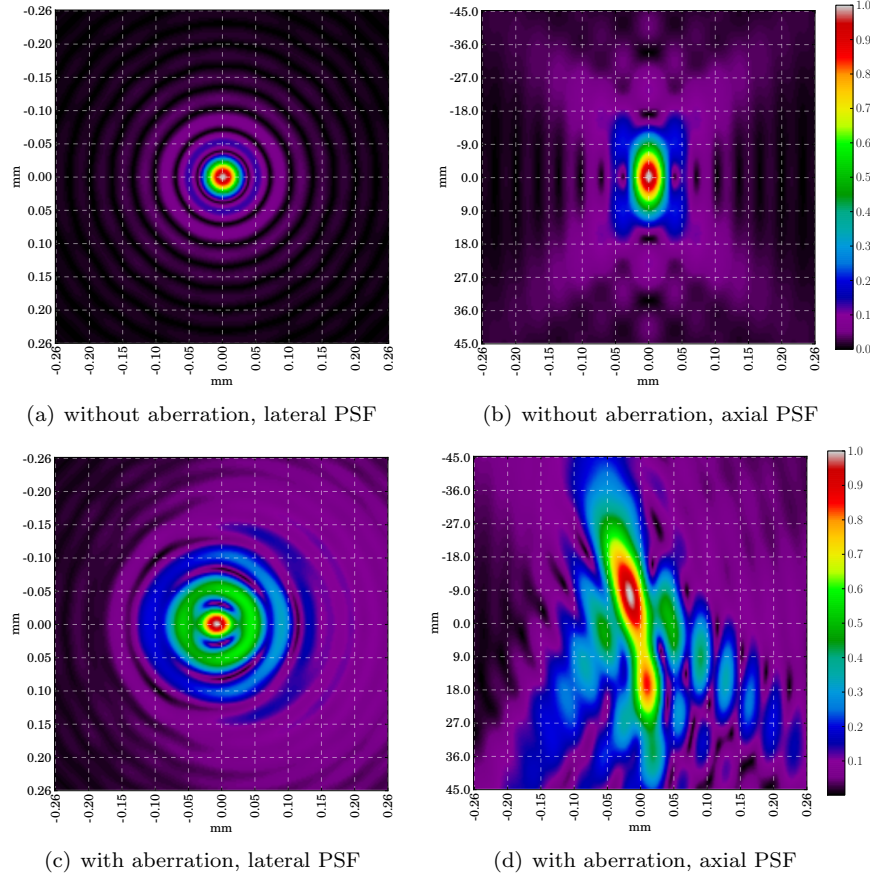


Figure 2.5: Simulated lateral and axial normalised PSF of an aberration-free and aberrated system.

### 2.4.2 OTF

The optical transfer function (OTF) gives an accurate picture of the optical performance as it describes how the spatial frequencies in the object plane are



transmitted to the image plane. In an incoherent system, the OTF (function  $\mathcal{H}$ ) is given by [3]:

$$\mathcal{H} = \frac{\int_{-\infty}^{+\infty} \int_{-\infty}^{+\infty} |h(x, y)|^2 e^{-i2\pi(\mu x + \eta y)} dx dy}{\int_{-\infty}^{+\infty} \int_{-\infty}^{+\infty} |h(x, y)|^2 dx dy}. \quad (2.15)$$

The Modulation Transfer Function (MTF) is the modulus of the OTF:  $|\mathcal{H}|$  and the Phase Transfer Function (PTF) is:

$$PTF = \arctan \left( \frac{\Im(\mathcal{H})}{\Re(\mathcal{H})} \right),$$

where  $\Im$  and  $\Re$  are respectively the imaginary and real part of  $\mathcal{H}$ . The OTF can also be written as:

$$\mathcal{H} = \text{MTF} \cdot e^{i\text{PTF}}.$$

The MTF describes how the spatial frequencies are attenuated by the optical system, while the PTF gives information on how these spatial frequencies will recombine at the image plane with the possibility of phase reversal artifacts leading to contrast inversion. The cut off frequency corresponds to the maximum spatial frequency which can be transmitted by the system and is  $f_c = \frac{2NA}{\lambda}$ .

Fig. 2.6(a) represents the MTF without aberration and 2.6(b) the MTF in the same aberrated system as the one discussed in the section 2.4.1. The spatial frequencies of the system are normalised to the cut off frequency. The effect of the aberration on the MTF tends to shrink the function and reduce the maximum transmissible spatial frequency, which is roughly 30% of the cut-off frequency calculated for the diffraction limited system.

We have discussed in this section, the use of different criteria to quantify

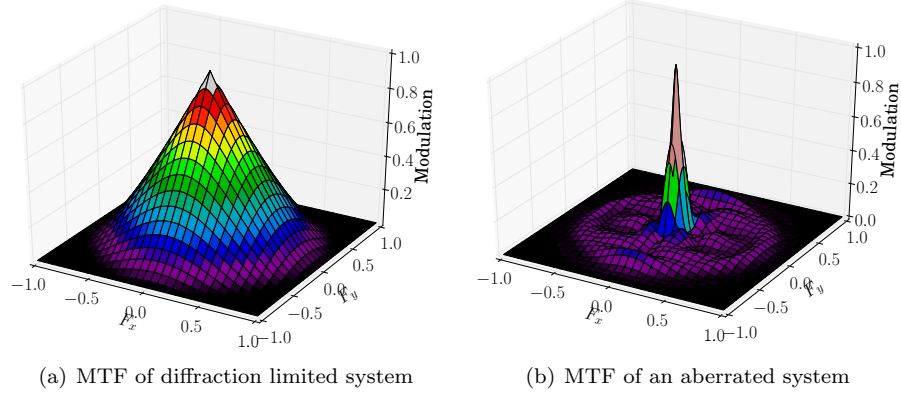


Figure 2.6: Comparison of the aberration free and aberrated MTF.

the system optical quality. Their determinations are made possible by a direct wavefront measurement. When the wavefront can be directly measured in an operating optical system, it yields an ideal representation of the optical quality and enables real time correction of aberration using AO (this will be discussed in more details in the next Chapter, and the reader will be referred to this chapter for the complete definition of AO and aberrations). This is the case in astronomical AO, where the wavefront is measured using a natural or artificial beacon which acts as a point source which is used for wavefront sensing. However, there are cases where the wavefront cannot be directly measured (in microscopy for example) and the optical quality of a system has to be assessed by an other way such as using evaluation based on the image. This particular technique uses sharpness metric applied onto the image to quantify the optical quality. In the next section, we will describe these metrics and their implementations in AO microscopy systems.

## 2.5 Representation of image quality

In this section we introduce the concept of an image sharpness metric as an alternative function to measure image quality and hence general optical quality of a system. So far, we have discussed optical quality criteria derived from the wavefront, such as the PSF and the OTF. When the wavefront is not accessible, other information has to be employed to evaluate the system optical quality based on the sharpness measurement of the image. Image sharpness metrics are functions giving a measurement of the blur level on the form of a scalar. As autofocus instruments employ such functions in their estimation of focus, the sharpness metrics have been widely investigated and discussed in literature over the past 40 years. For AO applications, as well as focus measurement, one will look for image sharpness metric with particular characteristics [11]:

- The metric will have only one extremum (maximum or minimum point) and this extremum will be obtained for aberration-free images. Typically in AO systems, the metric will reach an extremum when the active component correction will match the aberration present in the system.
- Monotonicity: The metric will exhibit some continuous variations on each side of the extremum.
- Effective range and sensitivity: the image sharpness metric will give sufficient variation over a large range of blur amplitude and be sensitive to small blur variations.
- The image processing leading to the computation of the image metric must be fast enough so that the aberration will not change, nor the object move, in the course of an optimisation run.
- Robustness: Finally the metric must exhibit a consistent behaviour on images with various content or noise.

Extending the use of these metrics from focus measurement to AO systems is relatively straightforward but brings slightly more complexity by adding further dimensions to the system. In focus measurement, the metric is a function of a single variable, which is the level of defocus. In AO, it becomes a function of  $N$  variables ( $N$  being the number of actuators or modes). The purpose of this section is to give an overview of the type of metric used for optimisation on images of extended object. Metrics discussed in the following section are especially interesting, because they have either been successfully experimented for focus measurement but not yet tested on AO set-up, or designed and used on AO set-up.

### 2.5.1 Metrics used in focusing techniques

Focus measurement is a method used to determine, from an image sequence, the relative blurring between images due to defocus. Two commonly used image sharpness metrics have been proposed in [12] and demonstrated to be monotonic with respect to the level of blur. This demonstration has been undertaken assuming that no noise was present. These two metrics are image variance, and energy of the image gradient. More recently, focus measurement based on 2 dimensional wavelet transform (2DWT) have been investigated and we will present one of them here.

#### Image variance

This metric is based on the energy of the image:

$$M = \frac{1}{N} \sum_{(x,y)} [I(x,y) - \langle I \rangle]^2, \quad (2.16)$$

where  $I(x,y)$  is the intensity at the pixel  $(x,y)$ ,  $\langle I \rangle$  is the average intensity of the image, and  $N$  is the number of pixels in the image. This function

tends to increase when the values of the pixel intensity deviate from the image mean. The effect of such a metric on the image histogram is to stretch it so the dark features gets darker and the bright features get brighter. The effect of 1 radian of simulated defocus is given in Figure 2.7. The histogram of the in-focus Durham cathedral image 2.7(a) is stretching over a wider area than the blurred image 2.7(b). The metric value calculated for the defocused image normalised to the perfect image, is calculated with Eq. 2.16, and is about 0.64. The standard deviation of the image can also be used as an image sharpness metric. It corresponds to the square root of Eq. 2.16 and adds slightly more weight to the dark features in the image.

### Energy of Image gradient

The second type of metric is based on the calculation of the energy of the image gradient. The metric is defined by:

$$M = \sum_{(x,y)} \left[ \left( \frac{\partial I(x,y)}{\partial x} \right)^2 + \left( \frac{\partial I(x,y)}{\partial y} \right)^2 \right]. \quad (2.17)$$

Figure 2.8, represents the sum of the square of the first derivative along x and y of the images 2.7(a) and 2.7(b). Subbarao in [12] also showed that the effect of the metric 2.17 was similar to applying a high pass filter in the Fourier domain:

$$M = \sum_{\mu,\eta} (\mu^2 + \eta^2) |\tilde{I}(\mu, \eta)|^2,$$

where  $(\mu, \eta)$  are the spatial frequencies, and  $\tilde{I}(\mu, \eta)$  is the Fourier transform of the image  $I(x,y)$ .

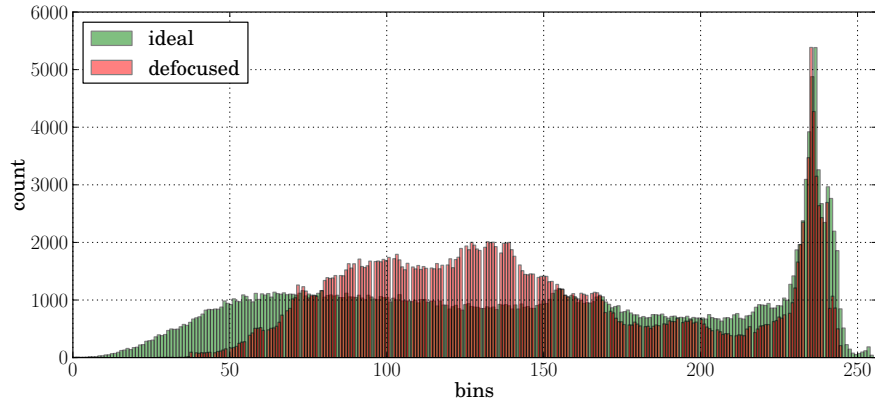
The energy of the image gradient is also computable using a convolution involving two kernels:



(a) ideal Image, normalised metric = 1



(b) Blurred image in presence of 1 radian of defocus, normalised metric = 0.64



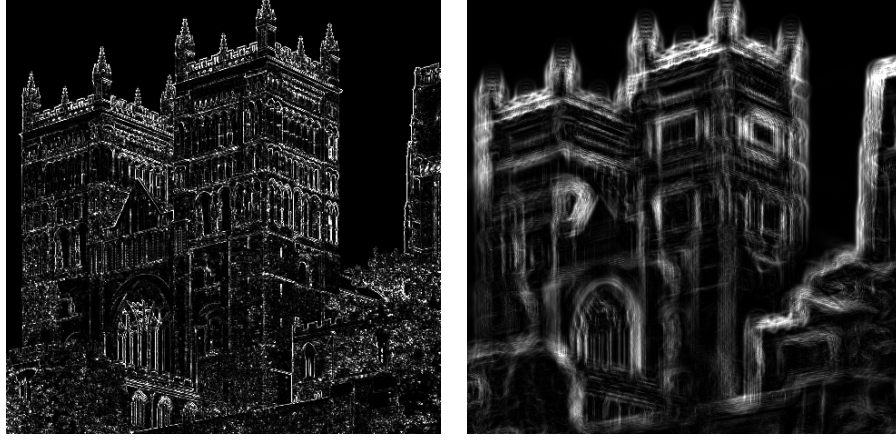
(c) Histogram of Images 2.7(a) and 2.7(b) respectively in green and red

Figure 2.7: Blur effect on the histogram

$$S_x = \begin{bmatrix} -1 & 0 & +1 \\ -2 & 0 & +2 \\ -1 & 0 & +1 \end{bmatrix} \quad S_y = \begin{bmatrix} -1 & -2 & -1 \\ 0 & 0 & 0 \\ +1 & +2 & +1 \end{bmatrix},$$

so Eq. 2.17 can be approximated by the following expression:

$$M = (S_x * I)^2 + (S_y * I)^2. \quad (2.18)$$



(a) Sobel filter applied to the in-focus image 1.17. Normalised metric = 1  
 (b) Sobel filter applied to the defocused image of Figure 2.7(b). The normalised metric value is 0.0026.

Figure 2.8: Illustration of the metric based on the energy of the image gradient

This operation, which is commonly used in image processing, is nearly equivalent to applying a Sobel filter. The Sobel filter is actually taking the square root of the Eq. 2.18.

The next section explains the use of a 2D wavelet transform as a metric.

### 2D wavelet transform technique

The two-dimensional (2D) wavelet transform is commonly used in image processing for various applications such as denoising, image compression or edge detection. It has also been used recently as a focus measurement [13, 14]. Unlike Fourier transform where the location in the image of a specific frequency is lost, the wavelet transform gives access to both the location on the image and the frequency amplitude. The 2D one level wavelet decomposition is explained in Figure 2.9 with the simple Haar wavelet. The input image <sup>1</sup> (top left) defined by the function  $I(x, y)$ , is first vertically convolved respectively with the half band low pass filter L and half band high pass filter H. In both cases, half of

---

<sup>1</sup>The image is the same as the one in Figure 2.7(a) and is given in false colour for clarity

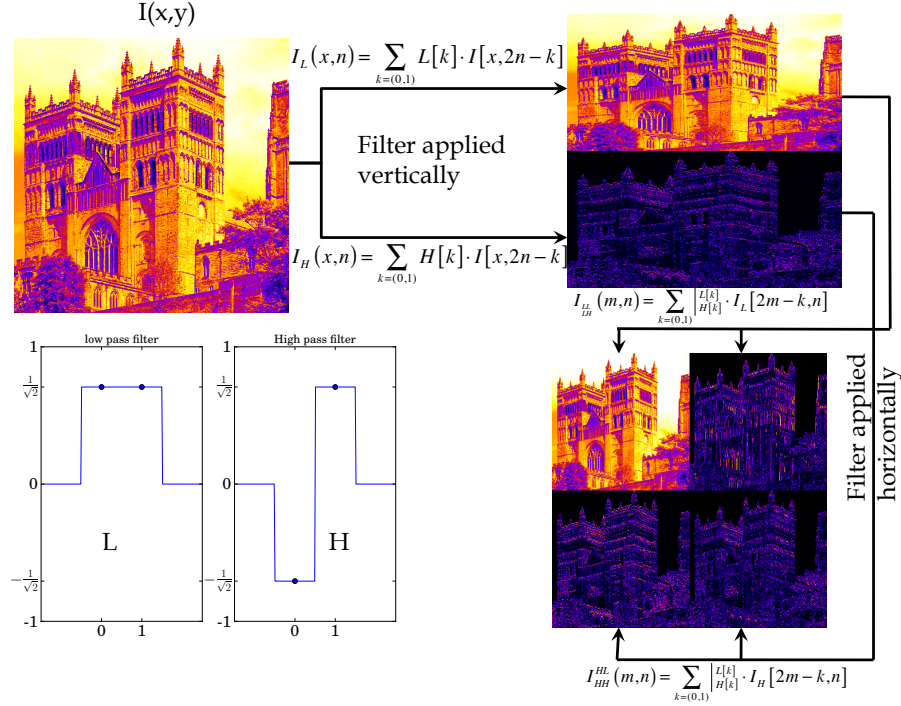


Figure 2.9: Illustration of a one level 2D wavelet transform using the Haar wavelet (low pass and high pass filter represented on the bottom left). The 2D discrete wavelet transform is the result of a convolution with a low and high pass filter and a downsampling by a factor of 2. To begin with, both filters are applied vertically, then horizontally resulting in 4 subimages.

the spatial frequency has been removed, so according to the Nyquist theorem, half of the sample can also be discarded, which is expressed in the equation by the factor 2. The top right image stores the result of the processing by the low pass filter (top - the image function is  $I_L(x,n)$ ) and the high pass filter (bottom - the image function is  $I_H(x,n)$ ). The same process is then applied horizontally. A low and high pass filters are simultaneously applied to  $I_L(x,n)$  respectively leading to 2 subimages  $I_{LL}$  and  $I_{LH}$ . The same low and high pass filters are then applied to  $I_H(x,n)$  leading also to 2 subimages  $I_{HL}$  and  $I_{HH}$ . The result of a 2D one level wavelet decomposition is an array of 4 sub-images,  $I_{LL}$ ,  $I_{LH}$ ,



$I_{HL}$ , and  $I_{HH}$ .  $I_{LL}$  is the approximation coefficient.  $I_{HL}$ ,  $I_{LH}$  and  $I_{HH}$  are respectively the horizontal detail, vertical detail and diagonal detail of the original image. A two level wavelet decomposition consists of then applying the same one level decomposition twice, by reapplying the decomposition on  $I_{LL}$ .

The detailed images contain information about the image high spatial frequencies content, hence the sharpness. Depending on the level of decomposition, these detailed images address specific ranges of spatial frequencies. The highest spatial frequencies are represented in the first level detailed images, and with increasing level of decomposition, the lowest spatial frequencies are then accessed. Figure 2.10 illustrates this principle, using a 1D example.

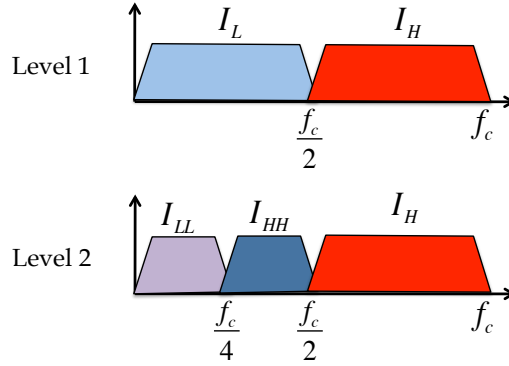


Figure 2.10: Example of the effect of multiple decomposition on a 1D spectrum. The first decomposition (top row) has divided the spectrum in two and each spatial frequency content is now localised on each sub image  $I_L$  and  $I_H$ . The second decomposition is applied to the approximated image so the resulting range of low frequencies is subsequently divided in two, leading to three distinctive ranges of spatial frequencies and their associated images.

The noise present in the original image is mitigated by the decomposition process due to the low pass filtering. In [14], the metric calculated on the highest level of decomposition is shown to remain monotonic on images containing larger levels of noise. The proposed image sharpness metric takes the following form:

$$M = \sqrt{\sum_{(x,y)} \frac{LH_n^2(x,y) + HL_n^2(x,y) + HH_n^2(x,y)}{LL_n^2(x,y)}}, \quad (2.19)$$

where  $n$  is the decomposition depth and HL, LH, HH are respectively the horizontal, vertical, diagonal detailed images and LL is the approximated image. The simulation performed in [14], shows that the metric remains monotonic in presence of noise up to a standard deviation of 30, after a decomposition of level 2.

All metrics described in this section, which have been used in focus measurement techniques will be used later within the simulation part of chapter 4.

### 2.5.2 Metrics used in AO systems with extended object optimisation

Finally, we now present metrics which have been used on AO systems.

#### The intensity square metric

The use of image sharpness metrics in adaptive phase correction devices was first proposed by Muller and Buffington in 1974 [15] with the view to optimise images of astronomical objects and was then experimentally studied in [16]. The monotonicity of some of the 8 metrics has been subsequently proved in the absence of noise.

The intensity squared metric, suggested by Muller and Buffington, is widely used in astronomical AO systems for correction of non-common path aberrations [17, 18] on spot like images:

$$M = \frac{\sum_{(x,y)} I^2(x,y)}{\left(\sum_{(x,y)} I(x,y)\right)^2}. \quad (2.20)$$

This metric will be used latter in the simulation and experimental tests described in chapter 4.

### Non linear point transformation

In [19], Fienup and Miller have taken the analysis further by looking, in particular, at metrics of the form of the sum over a non-linear point transformation described by

$$M = \sum_{x,y} I(x,y)^\beta, \quad (2.21)$$

such as power law, logarithm, with the view to using them on synthetic-aperture-radar images (SAR).  $I(x,y)$  is the intensity of the image at pixel  $(x,y)$ , and  $\beta$  is the power. The paper demonstrates that image sharpness metrics behave differently on different types of images and that their behaviour is tightly linked to the second derivative of the nonlinear point transformation.

For  $\beta = 2$ , the second derivative is constant. The metric will tend then to stretch the image histogram with equal weight to both the low and high values of  $I$ . For  $\beta > 2$ , the metric will give much more weight to stretching the image histogram to a larger value of  $I$ , and hence will work better on bright features on dark background. Conversely, for  $\beta < 2 \wedge \beta \neq 0$ , the metric will tend to emphasise darkening shadows. This paper also highlights that noise affects the metric monotonicity.

### Low spatial frequencies

In [10], an image sharpness metric based on the low spatial frequency content of an image has been used in an AO incoherent transmission microscope. Although the metric was based only on low spatial frequency information, the experiment showed improvement in all spatial frequencies because of the removal of the phase aberration achieved during the optimisation. The metric takes the form:

$$M = \int_{\xi=0}^{2\pi} \int_{m=M_1}^{M_2} S(m) m dm d\xi, \quad (2.22)$$

where  $S$  is the image spectral density,  $m$  and  $\xi$  are the polar coordinate in the spatial frequency domain.  $M_1$  and  $M_2$  are the radial spatial frequencies, which constitute the boundary of the integral and are considered to be small with respect to the cut-off frequency of the system.

### High Spatial frequencies

In [20], Walker compares some Fourier based image sharpness metrics with the intensity square metric given by Eq. 2.20 on various type of images in coherent and incoherent illumination systems. The blur variation was achieved by artificially adding defocus to the optical set-up. A Fourier based metric, emphasising the high spatial frequency content in an image is suggested:

$$M = \frac{\sum_{(x,y)} |\mathcal{F}[I(x,y)]_{masked}|}{\sum_{(x,y)} |\mathcal{F}[I(x,y)]_{unmasked}|}. \quad (2.23)$$

$|\mathcal{F}[I(x,y)]|$  describes the power spectral density (PSD) in the image (where  $\mathcal{F}$  denotes the Fourier transform). The masked PSD is obtained by setting values contained in a 5 x 5 pixels square mask located at the centre of the 2D PSD to zero.

This metric is used latter in the simulation and experimental tests described in chapter 4.

## Chapter 3

# Adaptive optics techniques applied to microscopy

Optical microscopy remains the key research tool for many biological studies. Within this general term, optical microscopy gathers a range of different imaging techniques whose common goal is to deliver highly resolved images of biological specimens and processes. Microscope objectives are designed to be aberration free when imaging in a well-defined and ideal condition. These conditions imply the presence of an homogenous refractive index medium between the imaging plane and the microscope objective frontal lens, and that this refractive index is the same as the immersion one, defined in the microscope objective design. This is of course, rarely the case because biological samples consist of multiple layers with various refractive indices and shapes. Furthermore, images of intact organs and live tissues require deeper imaging. These differences from the ideal condition create optical aberrations, which contribute in the deterioration of the image contrast and resolution. Over the last 15 years, there has been significant growth in the development and application of adaptive optics methods

within optical microscopy to overcome the limitation on the imaging depth and resolution in biological samples. This interest has been fed primarily, by the development of novel optical microscopy methods, making it possible to image deeper into the biological samples. Another reason is the significant reduction in cost of adaptive optical elements, which has galvanised the development of adaptive optics in commercial systems.

The pioneering application in this field was for beam scanned optically sectioning microscopy such as confocal [21], and non linear microscopy such as multi photon [22] and multi-harmonic microscopes [23, 24]. Optical sectioning modalities enabled deeper imaging but in return were affected by depth-induced aberration and AO allowed a significant improvement in the image quality. Recently, AO systems have found new challenges in the field of super-Resolution microscopes, with implementation for STED [25], STORM [26], and structured illumination [27].

This chapter is divided in two sections. In the first section, we describe the main source of image degradation in optical microscopy and define the need for AO systems. In the second section, we discuss AO in microscopy, its implementation and application.

## 3.1 Source of image degradation in microscopy

### 3.1.1 The out-of-focus parts of the sample

In a widefield microscope, the main source of image deterioration comes from the out of focus part of the sample being illuminated and then re-imaged appearing blurred, on top of the sharp region of interest in the focal plane of the microscope objective. The usual method to get rid of this effect is to physically, or optically section the sample. In the first case, the section is obtained with the destruction

of the sample and limits its application to an ex-vivo sample. Furthermore, the minimal thickness achievable is limited by the mechanical process of the sectioning.

More recently, with the invention of the confocal microscope by Minsky in 1957 [28] and the development of green fluorescent protein (GFP) in the 90s, a new branch of microscope has emerged based on optical sectioning. The advantage of optical sectioning is firstly that the sample is left intact, which makes it compatible with live imaging, and secondly that smaller section thickness is achievable. Optical sectioning microscopes are usually based on the following methods:

- Confocal microscopy [28, 29]: A scanned point source for illumination associated with a confocal pinhole detection. This is the case in confocal microscopes, where the sample is excited within the cone of the illumination and the emitted light, out of the imaging plane is carefully rejected by the confocal pinhole.
- Multi-photon microscopy [30, 31]: A scanned point source for illumination associated with a photomultiplier tube as a detector. The multi-photon technique is based on a non-linear process: Two excitation photons are absorbed at the same time inducing the emission of a photon with a half wavelength<sup>1</sup>. As this process requires a high density of excitation photons, the process occurs only at the focal point of microscope objective in a small volume, where the beam is focused.
- Light sheet illumination microscopy [32]: In a widefield microscope, a light sheet selectively excites a slice of the sample at the focal plane of a microscope objective placed perpendicular to the illumination sheet,

---

<sup>1</sup>The emission wavelength is in fact not exactly half of the excitation, due to loss of energy through relaxation in the lower vibrational energy states

thus enabling an entire optical section to be recorded in a single camera exposure. This specific microscope technique will be discussed in Chapter 6.

- Structured illumination [33]: In a widefield microscope, a structured excitation light with a regular pattern (a grid for example) is superimposed onto the sample structure. The grid is seen in focus only at the imaging plane of the microscope and the out of focus part of both the grid and the sample are seen, on the camera as a blurred background which does not change with depth. The optical sectioning is achieved by eliminating the background through an arithmetical combination of 3 images<sup>1</sup>, on which the grid has been shifted by  $\frac{2\pi}{3}$ .

Once the out-of-focus parts of the sample are no longer imaged, the resolution is ultimately limited by optical aberrations originated along the optical path.

### 3.1.2 Aberrations in microscopy

The cause of aberration in microscopy has been widely discussed and analysed [34, 35]. In this chapter, we will give an overview of their origin.

High numerical microscope objectives are very complex systems consisting of numerous elements and advanced synthetic glass. Depending on the price, a range of correction and specifications are available from the simple achromatic lens, axially corrected for two wavelengths and for spherical aberration, up to plan aprochromat corrected for up to 5 wavelengths and multiple aberrations. However, these high quality microscope objectives are designed to work in restricted conditions such as specified wavelength, temperature, immersion medium refractive index and field of view. The use of these microscope objectives outside

---

<sup>1</sup>3 images is the minimum number of images involved in the reconstruction. It is possible, of course, to use a larger number of images.



their design specification can lead to aberrations, which can limit the contrast and resolution.

### Refractive index mismatch

One of the most common aberrations, which regularly occurs when imaging deeply into biological samples, is the refractive index mismatch (Figure 3.1). It happens when the normally aberration free converging light in the vicinity of the focus travels through an interface with a refractive index different from the immersions. This effect has been studied in detail for the particular case of a planar interface [36, 21, 37].

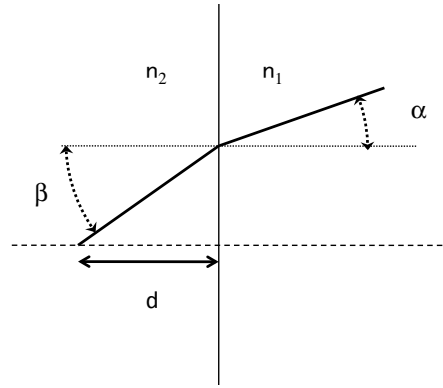


Figure 3.1: Refractive index mismatch at a planar interface ( $n_2 < n_1$ ).

The phase aberration induced by a refractive index mismatch in a planar configuration, for microscope objectives obeying the sine condition, is calculated in [21], and is

$$\Phi(d, \rho) = \left( \sqrt{\frac{1}{\sin^2(\beta)} - \rho^2} - \sqrt{\frac{1}{\sin^2(\alpha)} - \rho^2} \right) dn_1 \sin \alpha, \quad (3.1)$$

where  $\alpha$  is the maximum angle determined by the numerical angle of the microscope objective, and  $\beta$  is the refracted angle of  $\alpha$  through a planar interface, in a

refractive index medium  $n_2$ .  $\rho$  is the normalised radius. On Figure 3.2, a simulation of the phase aberration created by a refractive index mismatch ( $n_1 = 1.5$  (typically oil index) and  $n_2 = 1.3$  (typically water index)) is represented for different NA, when imaging at a depth of 200 microns. For small NA, the phase aberrations has a parabolic shape, as the defocus is the main aberration. For a large NA, the phase aberration displays a higher order variation, as spherical aberration becomes predominant.

This planar configuration has been very well characterised both theoretically and experimentally, and such image distortion typically occurs on microscopes using coverslips. As the sample lies generally in a water medium behind the coverslip, this effect is often observed when using a high numerical aperture objective lens with oil immersion. The use of microscope objectives with an adjustable collar, which have been initially designed for correcting the spherical aberration induced by the coverslip thickness variation also offers a way of correcting refractive index mismatch [38].

When the interface is not plane, for example in light sheet microscopy which aims to image entire live specimen, the refractive index mismatch induces other types of aberrations depending on the geometry. In [39], the aberration created by a cylindrical glass pipette in a water immersion medium has been theoretically and experimentally studied. Astigmatism is in this configuration, the main aberration.

### **Sample induced aberrations**

Sample induced aberrations are, with scattering, among the main limitations in optical sectioning microscopy. They are created by the heterogenous structure from which the sample is composed. Each layer through which light travels, with its specific refractive index and shape contributes to the wavefront distortion. In [40], specimen induced aberration have been characterised and measured for

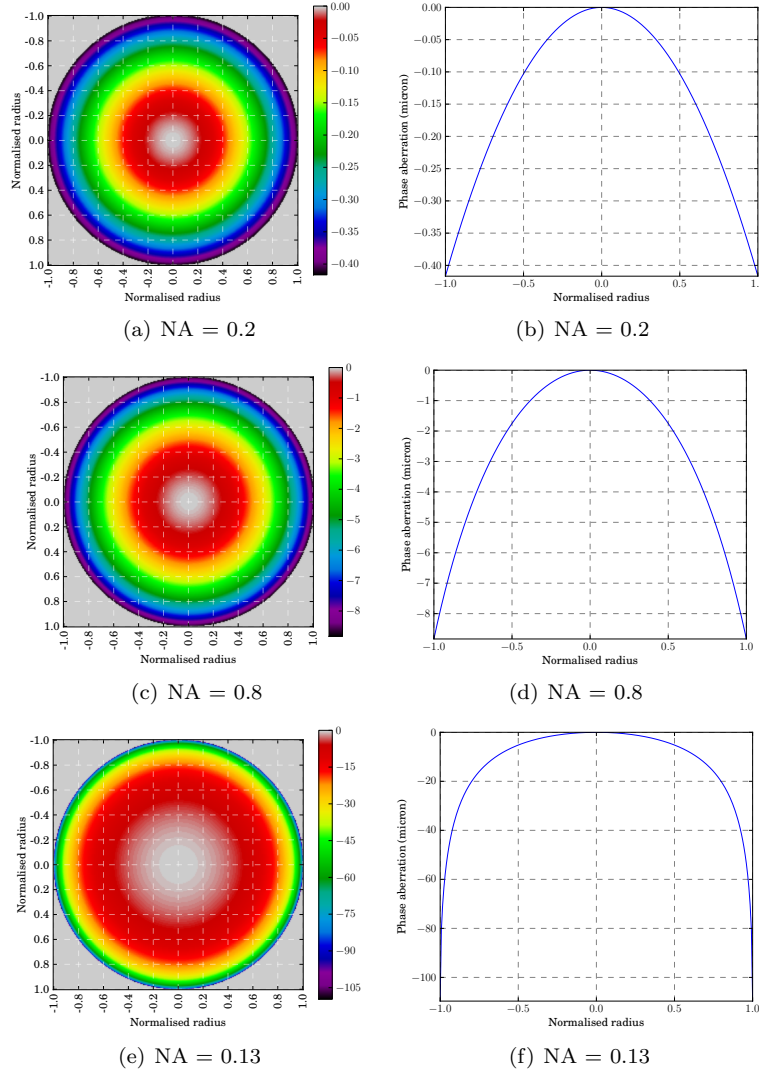


Figure 3.2: effect on Phase of refractive index mismatch at a planar interface for  $n_1 = 1.5$  et  $n_2 = 1.3$  at 200 microns depth for NA =0.2, 0.8 and 1.3. Colour bars represents the phase aberration in microns.

a range of 6 biological samples (including C elegans, rats and mice tissues), using a phase step interferometer. The aberration has been expressed in term of Zernike modes. It is shown that a correction of low order Zernike modes only (up to the 12<sup>th</sup> or 18<sup>th</sup> modes) can significantly improve the signal and

the resolution even if it only remains a partial correction. It shows as well, that the aberrated phase function varies significantly with the position in the specimen, which in other terms means that the isoplanatic patch is small. In [39], the variation of sample-induced aberrations has been characterised with depth and corrected with AO in an ex-vivo Zebrafish embryo pectoral fin. In [41], aberrations are corrected, at different depths in the terminal pharyngeal bulb of a *C. elegans* sample. In [37], Booth and Wilson suggest strategies for the correction of aberrations created by human skin which is composed of 3 layers of various refractive indexes. In [42], aberrations created by mouse brain tissues have been measured and corrected using AO. In [43], aberrations created by the same live sample have been quantified and corrected.

### **Sample holder aberrations**

In mounting configuration using coverslips, aberrations are often created by the coverslip. As mentioned before, any difference in the coverslip thickness with respect to its expected and designed thickness, produces defocus and spherical aberration. Another coverslip related aberration has been discussed in [44], which mostly affects the water immersion microscope objectives. The tilt of the coverslip generates an asymmetry of the PSF, which is particularly detrimental for 3D deconvolution.

With the emergence of light sheet microscopes, which aim to image entire living specimens, the traditional coverslip and microscope slide have been put in the background and new sample holder techniques have been designed. Great effort has been made in designing a sample holder, which gives full access to the sample, with a limited number of optical or mechanical interface into the beam. An inventory of these new holding techniques has been discussed in [45].

Figure 3.3(A) represents the optimal way of holding the specimen, by hooking or clipping it in front of the objective. This configuration does not, of course,

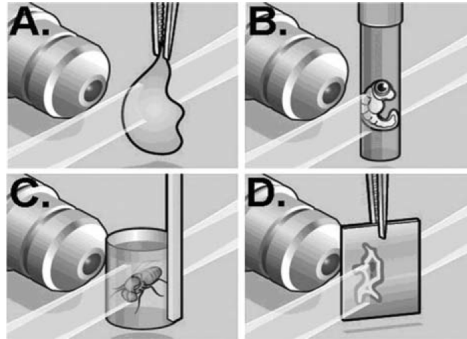


Figure 3.3: Sample holder techniques used in light sheet microscopy. Picture explained in the text.

present any sample holder induced aberrations and can be applied to a limited range of selected samples only. In Figure 3.3(B), the specimen is embedded in a gelling agent such as agarose. In Figure 3.3(C), the specimen is placed in a chamber made of agarose or transparent polymer. Then, Figure 3.3(D) shows the case when the sample is sandwiched between 2 coverslips and tilted at  $45^\circ$ .

These techniques (Figure 3.3 (B,C,D)) are prone to sample holder induced aberrations [46]. In such cases, aberrations can be generated due to the difference in refractive index between the holder and the immersion medium. Agarose has refractive index very close to water, but the small difference can generate image distortion.

In the next section, we will discuss the solutions carried out for the active correction of these aberrations.

## 3.2 Adaptive optics in microscopy

With the increasing interest in *in-vivo* imaging, fully functioning tissues and organs are now imaged at a high resolution with a view to ultimately observe every single cell, as they develop or interact. As optical sections are produced deeper in the sample, the resolution is more affected by aberrations. Adaptive

optics is an essential tool to correct these aberrations and enables high quality images. In this section, we will have first an overview of the different active optical components enabling wavefront correction. We will subsequently discuss closed-loop (also referred to direct wavefront sensing) and wavefront sensorless configurations and present how these techniques have been implemented in microscopy.

### 3.2.1 Active phase optical elements for wavefront shaping

The active phase optical elements used in microscopy are divided into two main families:

- The deformable mirror (DM).
- The spatial light modulators (SLM).

Due to their achromaticity, high reflectivity and speed, DMs are generally preferred. A wide range of DM are now commercially available at a relatively low cost. In the next subsection, we will describe the different technologies available.

#### Electrostatic Continuous membrane mirror

A thin conductive and reflective membrane placed above the actuators is used as a mirror. It is electrostatically deformed when a voltage difference is applied between the actuator and the surface. The force applied to the surface is:

$$F_i = \frac{\epsilon_0}{2} \left( \frac{V_i}{d} \right)^2, \quad (3.2)$$

where  $F_i$  is the force applied onto the membrane by the  $i^{th}$  actuator,  $\epsilon_0$  is the dielectric constant,  $d$  is the distance between the actuator and the surface, and  $V_j$  is the voltage of the  $i^{th}$  actuator. The electrostatic force is proportional to the

square of the voltage. For this reason, only attraction forces can be generated. When the actuators are placed under the membrane (as illustrated on Figure 3.4(a)), then the mirror's surface can only be pulled. To create mirror surface displacement in both directions, a bias voltage has to be applied on all actuators beforehand, so the mirror shape corresponding to the starting position is not flat, but concave. Another solution is to use a "Push and Pull" electrostatic mirror, where a transparent set of electrodes is additionally placed above the mirror's surface as depicted in 3.4(b).

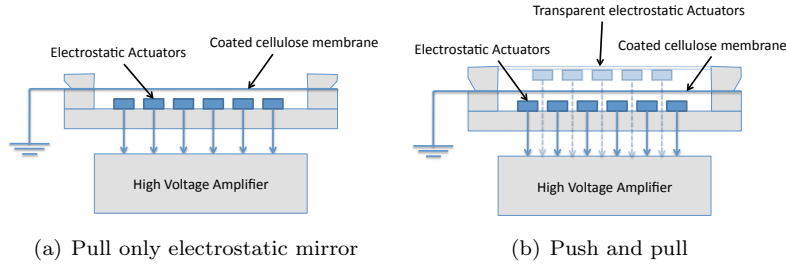


Figure 3.4: Electrostatic membrane technology

### Magnetic Continuous membrane mirror

The active mirror consists of a continuous membrane with small magnets placed at the back of the reflective surface. The membrane deformation is achieved with the help of solenoid actuators, creating a magnetic field which push and pull each magnet. The diagram is given in Figure 3.5. As opposed to Electrostatic mirrors, the force applied onto the mirror surface is, this time, proportional to the current, so both displacement directions can be achieved depending on the current direction:

$$F_i \propto \mu_0 \frac{NI_i}{l}, \quad (3.3)$$

where  $F_i$  is the force applied to the membrane by the  $i^{th}$  actuator,  $\mu_0$  is the magnetic constant,  $N$  is the number of turns and  $l$  is the solenoid length. In the experimental part of this thesis, a Mirao<sup>TM</sup> 52-e mirror (from Imaging Optics) based on this technology is used.

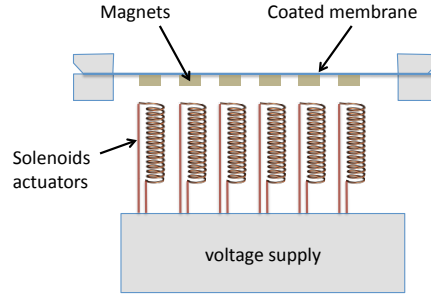


Figure 3.5: Magnetic continuous membrane

### Piezoelectric wafer mirror

Piezoelectric unimorph (Figure 3.6(a)) and bimorph (Figure 3.6(b)) wafer mirrors are formed with an array of electrodes which are respectively attached to a single sheet or sandwiched between 2 sheets of piezoelectric material (with opposite polarity). When a voltage is applied to the electrode, then the piezoelectric wafers expand or contract (depending on the voltage polarity) creating a localised bending which is proportional to the voltage. In the case of the bimorph mirrors, the deformation is amplified by the fact that when one sheet is expanding the other is retracting, creating higher spatial frequencies on the mirror's surface than for the unimorph mirror. However, piezoelectric mirrors are prone to some hysteresis, which limits the accuracy of the correction.



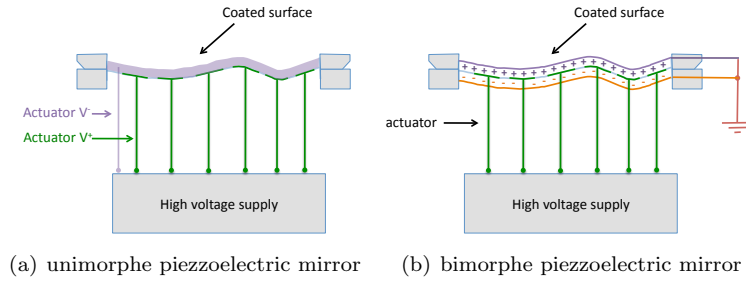


Figure 3.6: Piezoelectric DM technology

### MEMS mirror

Micro-Electro-Mechanical Systems (MEMS), due to their manufacturing process, have a greater potential to be inexpensive, and with their small size and high number of actuators, are increasingly used in microscopy. Both continuous face sheet 3.7(a) and segmented 3.7(b) technologies are possible. A metal coated thin film mirror is attached to the electrostatic membrane by silicon posts. When a voltage is applied to the mirror electrodes, the electrostatic force locally attracts the mirror membrane and creates a localised bending.

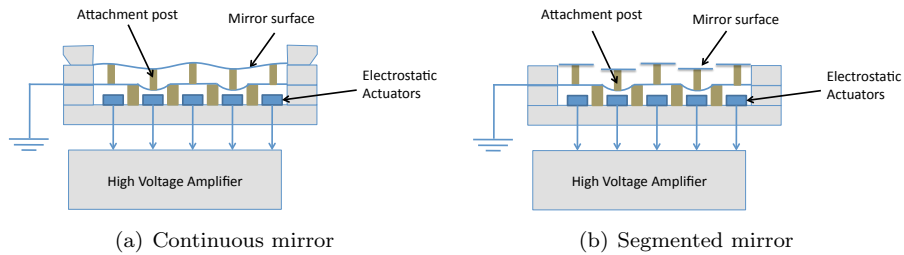


Figure 3.7: MEMS technology

### Spatial light modulators

Spatial light modulators (SLM) are the other class of active optical elements used for wavefront correction. They are made of liquid crystal micro-displays

and work in transmission or reflection. They can modulate the intensity and/or the phase of the incident beam by changes of the refractive index of each pixel. The main advantage of such devices is that the phase achieved can be much more accurate than for a deformable mirror because there is no crosstalk between the actuators. Furthermore, there is no limit on the stroke, because the phase is wrapped and the number of active elements is much higher than for the DM. On the other hand, SLM are generally slower, less efficient in terms of throughput, and are chromatic devices, which limit their wavelength range. There are two families of SLM:

- Electrically addressed SLM: The control command is addressed electronically to the SLM by way of voltages applied onto the different pixels.
- Optically addressed SLM: The control command is addressed to the SLM with an 2D irradiance map projected onto its active area. The change of refractive index is a function of the local intensity.

The next two sections describe AO configurations traditionally used in microscopy.

### 3.2.2 Direct wavefront sensing

In direct wavefront sensing, the wavefront is measured and the information from this measurement is used to apply a compensative shape onto the mirror. Depending if the wavefront sensor is placed before or after the DM, the system is said to be in Open-Loop (Figure 3.8(a)) or Closed-Loop (Figure 3.8(b)).

Astronomical AO uses mostly direct wavefront sensing because natural or artificial stars can be used as a point source for the wavefront sensor. Furthermore, the optimisation is very fast as it requires, in theory, only one measurement to achieve a correction which makes it appropriate for correcting fast changing atmospheric aberrations. In microscopy, direct wavefront sensing has also been

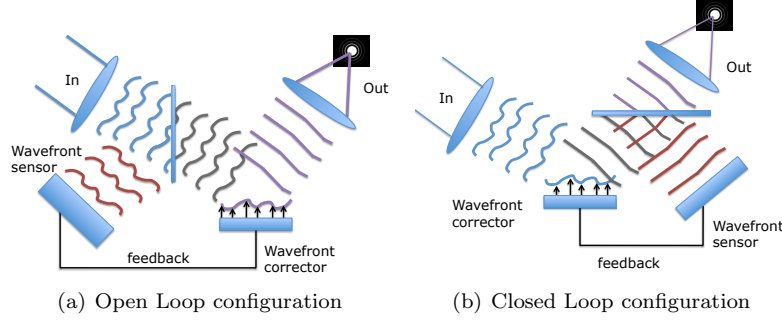


Figure 3.8: Direct wavefront sensing configurations

employed, and a description of an experiment using the backscattered light from the sample will be given in chapter 5. In direct wavefront sensing, the wavefront sensor is at the heart of the system and sets the global performances. It is crucial to understand its specifications and how, from a measurement of spot motion, the wavefront information can be recovered and the control signal of the DM obtained. The next section will discuss the WFS control and reconstruction algorithm.

### Wavefront sensor

We will limit our discussion to the Shack-Hartmann wavefront sensor (SHWFS), which is used throughout this document.

The SHWFS is composed of a microlens array and a CCD sensor located at the focus of the microlenses. Figure 3.9 gives the principle of the SHWFS. The microlens array divides the system aperture into subapertures, which locally measure the gradient of the wavefront through the spot's displacement on the CCD, which is proportional to the focal length,  $f$ , and the local wavefront gradient  $\theta_x$ :

$$\Delta x = f \tan \theta_x = \frac{\lambda f}{2\pi S} \int_{subaperture} \frac{\partial \Phi(\vec{r})}{\partial r_x} d\vec{r}.$$

$S$  is the subaperture area,  $\vec{r}$  is the vector describing the position in the subaper-

ture,  $\Phi$  is the phase.

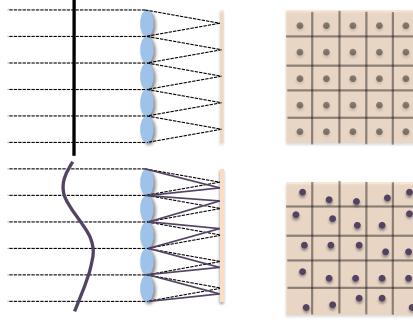


Figure 3.9: Shack-Hartmann wavefront sensor, sensing a plane wave (top) and an aberrated wave (bottom)

The centroid within the subaperture along both axes, is given by

$$(c_x, c_y) = \left( \frac{\sum_{i,j=1}^{N_x, N_y} i \cdot I(i, j)}{\sum_{i,j=1}^{N_x, N_y} I(i, j)}, \frac{\sum_{i,j=1}^{N_x, N_y} j \cdot I(i, j)}{\sum_{i,j=1}^{N_x, N_y} I(i, j)} \right), \quad (3.4)$$

where  $N_x$  and  $N_y$  are the number of pixels respectively along the x and y axis of the subaperture,  $I(x, y)$  is the intensity at the pixel  $(x, y)$ .

### Wavefront modal reconstruction

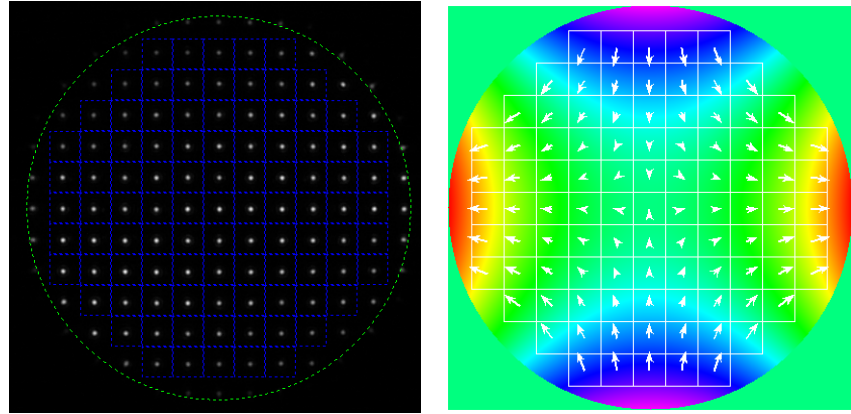
From the centroid measurement using eq. (3.4), it is possible to obtain an estimation of the phase using a reconstruction method. There are a few different methods but here, we will limit our discussion to the one employed later in chapter 5, referred to as "modal reconstruction", which uses a set of Zernike or Lukosz polynomial to approximate the wavefront.

If  $s$  is the interleaved  $x$  and  $y$  centroids vector (dimension  $2k$ ), which is in essence, the output data from a WFS, then the mode amplitude vector  $a$  (dimension  $N$ ) is computed as:

$$\mathbf{a} = \mathbf{G}^{-1} \mathbf{s}.$$

$\mathbf{G}^{-1}$  is the inverse the wavefront sensor response  $\mathbf{G}$  (dimension  $(N, 2k)$ ). The evaluation of  $\mathbf{G}$  is done through a "numerical" calibration, which is illustrated in Figure 3.10. For each mode with unitary amplitude, the theoretical spot deviation in both x and y directions is assessed given the WFS parameters (sub-aperture geometry, focal length, pitch) and the resulting WFS spot position vector is then stored in the column of  $\mathbf{G}$ .

Figure 3.10(a) shows a typical WFS image and geometry. The green circle defines the unit pupil on which the Zernike or Lukosz polynomials are calculated. Each blue square represents a subaperture. Figure 3.10(b) shows how the calibration computes, for an optical mode with an unitary amplitude - here astigmatism, the theoretical spot deviation that the WFS would record. The modal optimisation scheme experimentally implemented in chapter 6, uses this method for the DM calibration, in view to generate either Zernike or Lukosz modes.



(a) wavefront sensor spots and configura- (b) Calculation of the x and y spot centroid  
tion on the Zernike mode (2,2)

Figure 3.10: Wavefront sensor modal reconstruction

### Interaction and control matrices

In direct wavefront sensing, the correction is based on the wavefront measurement, and enabled by addressing the DM with the appropriate signal. The control matrix, which defines the mirror-sensor system interaction, links the wavefront sensor signals to the mirror actuator's signals. The control matrix is defined by

$$\mathbf{x} = \mathbf{C}\mathbf{s}, \quad (3.5)$$

where  $\mathbf{s}$  is the wavefront sensor signals vector  $x$  and  $y$  interleaved spot centroids (dimension  $2k$ ),  $\mathbf{x}$  is the vector of actuators control signals (dimension  $M$ ), and  $\mathbf{C}$  is the  $2k * M$  control matrix.

The control matrix is usually not directly assessed, but rather obtained by calculating the pseudo inverse of the interaction matrix  $\mathbf{B}$ . The interaction matrix  $\mathbf{B}$  links the mirror actuators signals to the wavefront sensor signals:

$$\mathbf{x} = \mathbf{C}\mathbf{s} = \mathbf{B}^+\mathbf{s}. \quad (3.6)$$

The interaction matrix is computed during the system calibration, by sequentially poking each mirror actuator individually with a reference voltage value, and measuring the corresponding response on the wavefront sensor. Each column of the interaction matrix corresponds to the measurement of the  $x$  and  $y$  interleaved spot centroids. The advantage of this method is that it is done *in-situ*, so the calibration takes into account all possible alignment errors in the system.

All matrix inverses (WFS response, interaction, etc...) are obtained through the singular value decomposition (SVD) [47]. The SVD of the interaction ma-

trix, for example, is a product of three matrices

$$\mathbf{B} = \mathbf{U}\mathbf{\Lambda}\mathbf{V}^T, \quad (3.7)$$

where  $\mathbf{V}$  is a  $M \times M$  orthogonal matrix whose column form a complete orthogonal basis for the set of mirror controls modes. The symbol  $^T$  refers to the transpose.  $\mathbf{U}$  is an  $2k \times 2k$  orthogonal matrix and gives an indication on how the WFS is able to sense those modes. Each column of  $\mathbf{U}$  forms the wavefront sensor modes. Finally,  $\mathbf{\Lambda}$  is a  $2k \times M$  diagonal matrix and the values on its diagonal represents the singular value of  $\mathbf{B}$ . Once  $\mathbf{B}$  is decomposed as in eq. (3.7), the control matrix is then simply obtained by

$$\mathbf{C} = \mathbf{V}\mathbf{\Lambda}^+\mathbf{U}^T,$$

where  $\mathbf{\Lambda}^+$  is the pseudoinverse of  $\mathbf{\Lambda}$ , and stores on its diagonal, the inverse of the  $\mathbf{\Lambda}$  elements.

The closed loop experiment implemented in a bright field microscope later described in chapter 5, uses this evaluation of the control matrix.

### Implementation of wavefront sensed AO configurations in microscopy

The various implementations mainly differ by the way "the artificial star" is generated. In [48, 42], fluorescent beads have been used respectively on a wide-field and confocal microscope. The bead supplies a point-like source for the wavefront sensor. As a practical and easy solution for wavefront sensing, it has some drawbacks such as:

- The bead microinjection in the negative pressure protocol which limit the potential application for in vivo imaging.

- The random location of the beads within the sample, does not allow a complete correction of the aberration. The correction is limited to the area where the bead can be found.

A non invasive solution using a nonlinear guide star has been proposed in [41] in a 2 photon microscope. In this paper, the 2 photon excitation spot creates a localised fluorescent beacon onto the sample which is used subsequently by the WFS. The DM placed on the excitation path corrects for the sample aberrations, which are measured on the emission path. This method removes the disadvantages of beads, but at the price of increased complexity. In [49], the centrosomes, which are a particular sub-diffraction feature in the sample cell are fluorescently labelled, and used as artificial guide stars in a confocal microscope. In [50], the backscattered light from the sample of a two-photon excitation beam is used as an artificial guide star. Finally, Interferometric methods, using laser coherence gating to select the imaging plane depth, has been reported in [51]. The phase information is extracted via a four-step phase-shifting interferometry.

### 3.2.3 Sensorless adaptive optics

As the aberration created by the biological sample does not vary quickly with time, the use of an optimisation methodology based upon an image metric, which inherently takes more time, rather than actually sampling the aberrations within the sample in real time has been favoured on most of the AO microscopy implementations because it is simpler. In sensorless AO, the determination of the optimum mirror shape is not based on a direct wavefront measurement but through post-processing on multiple images:

- either by recovering the aberrated phase from images of point-like objects, this method is called phase retrieval.



- or by comparing the sharpness of each image when acquired with a different mirror shape. Then, assuming that the metric exhibits a single extremum and is monotonic on each side of the extremum, a search algorithm is used to find the mirror shape corresponding to this extremum.

### Phase retrieval technique

Using a phase retrieval algorithm [52, 53], the phase and intensity distribution in the pupil can be recovered from defocused PSFs [52] and then used as input to a calibrated DM. However, the images need to be of point-like objects otherwise, for extended object images, the knowledge of the object function is also required, which is rarely the case<sup>1</sup>. As a result, this method is more a complementary technique to the direct wavefront sensing, because when imaging point-like objects, one can then simply replace the camera with a WFS and perform direct wavefront sensing. Phase retrieval technique finds some applications in some particular cases, for example in systems where the insertion of a WFS is problematic.

The algorithm suggested in [52, 53] where phase and intensity in the pupil can be recovered is in fact, an extension of the Gerchberg-Saxton algorithm [54], where phase only is recovered from a known intensity distribution in the pupil. Figure 3.11 shows a simulation of the phase retrieval optimisation technique.

The top row shows the approximated amplitude and phase of the wave in the objective pupil, used as a starting point of the optimisation and the 3 corresponding PSFs respectively defocused by -1 wave, in focus, and defocused by +1 wave in the microscope objective imaging plane. The plot in blue shows the convergence from the starting position to the solution. The Gaussian amplitude of the wave and its phase has been determined in about 150 iterations from a

---

<sup>1</sup>If neither the object nor the PSF are known, blind deconvolution can be used but this is another area which is not covered in this thesis.

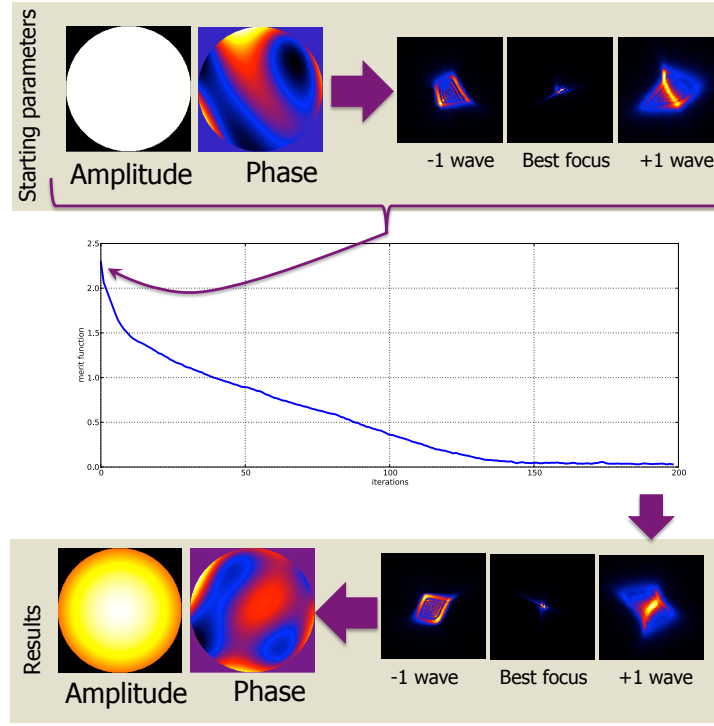


Figure 3.11: phase retrieval optimisation example. From the starting phase and uniform amplitude, the PSF is computed and then compared to the measured one. At each iteration, the algorithm computes a new phase and amplitude based on the intensity PSF. The merit function decreases accordingly, until it reaches a plateau indicating that the computed intensity PSF is the same as the measured one (within a given tolerance)

top-hat amplitude distribution and a random phase.

### Sharpness metrics and search algorithm

Most of AO sensorless configurations are based on image optimisation using a specific search algorithm and a sharpness metric. It is an iterative process whose principle is to measure and compare the sharpness of different images corresponding to different mirror shapes, and based on this comparison, compute the ideal shape of the mirror. In [55] a genetic algorithm is used with a metric representing the two photon signal returning from the sample. In [56], some of

the image sharpness metric proposed by Muller and Buffington is used with a Nelder-Mead simplex algorithm on extended object images.

We have seen in chapter 2, that the choice of image sharpness is important for the optimisation performance. In [57], search algorithms including "Genetic", "hill climbing", and "Stochastic Gradient descent" algorithms have been compared and investigated. It is shown that the algorithm is also a crucial contributor in the optimisation time and performance, and that its choice has to be made carefully. The reader is referred to this paper for a wider discussion about them. Here, only simplex and modal optimisation algorithms are used in the experimental part of the thesis.

### Simplex Algorithm

The simplex algorithm was originally proposed by Nelder and Mead [15] in 1965.

It allows the minimisation of a function of  $N$  variables, in our case, the image sharpness metric function. The variables are in our case, either the mirror actuators or the mirror modes.  $N + 1$  evaluation of the function are needed as starting points for the optimisation. The  $N$  variables used during the initial evaluation are either randomly chosen or approximated. In Figure 3.12, the algorithm organisation chart is given. From an initial guessed set of  $N+1$  vectors of dimension  $N$ , the vector giving the worst metric value (corresponding to the largest value) is removed, and replaced by the reflected vector<sup>1</sup>. The metric value calculated with this new vector is then compared to the one calculated with the best of the initial guesses. If it is better (smaller), then a reflection - expansion<sup>2</sup> by a factor 2 beyond the mirrored vector and another iteration is

---

<sup>1</sup>The reflection discussed here is the mathematical transformation in a  $N$  dimensions space which consists in a point reflection of the worst vector with respect to the centre of mass of the others. The visualisation of this reflexion is not simple in a  $N$  dimension space, so the reader is referred to annexe 1 for a step by step 2D example or to the 1D example given on Figure 3.12

<sup>2</sup>this transformation corresponds to a scale symmetry by a factor 2, with respect to the centre of mass

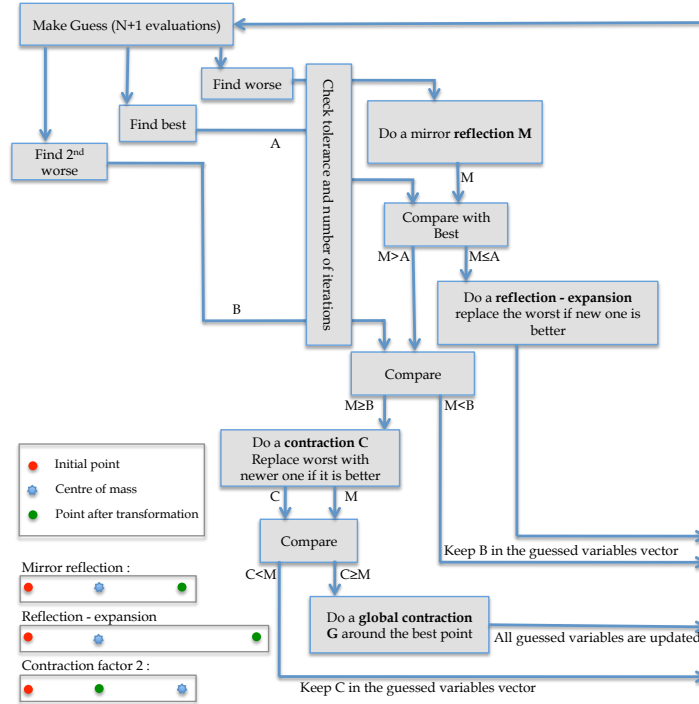


Figure 3.12: Simplex algorithm organisation chart. The best value corresponds here to a minimum.

called. If it is not better than the initial best vector, then it is compared to the initial second maximum. If the mirrored vector is better than the second maximum, it is then kept and replaces the previous worst vector, and another iteration is called. Finally, if the mirrored vector is not better than the second worst, then a 1 dimensional contraction (between the mirrored vector and the centre of mass) is achieved. If this resulting vector is better than the mirrored vector, then another iteration is called, if not, a global contraction (involving the set of  $N$  vectors) around the best vector is conducted and another iteration is then called.

A step by step optimisation example is given in Annexe 1. The optimisation is performed in a 2 dimensional space with the presence of a local minimum.

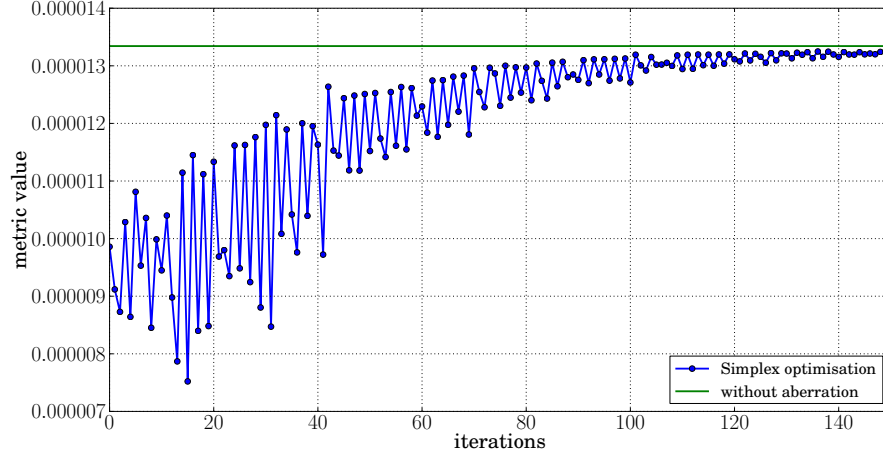
A simulation of a simplex optimisation using 12 Zernike modes amplitude as variables is given on Figure 3.13(a) with the metric being the standard deviation as described in Chapter 2. The before and after images are given respectively in Figures 3.13(b) and 3.13(c). The simulation assumes a complete and accurate reproduction, by the DM, of the specified mode. In a real optimisation (i.e. involving a DM), the convergence is also affected by the fact that the DM does not accurately reproduce the desired mode which leads to further iterations and then slightly longer optimisation time.

### Modal optimisation

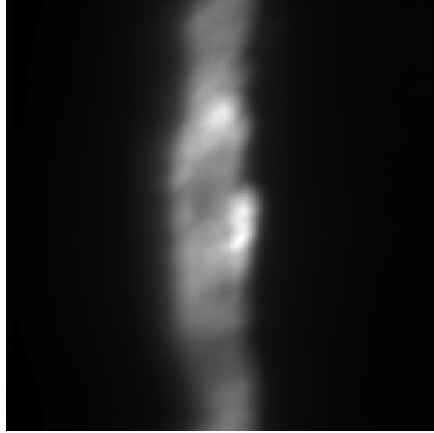
The modal optimisation was first proposed in [58] on a confocal microscope and used on various types of microscope such as multi-harmonic [23], widefield [10], and two photon microscopes [59]. The algorithm consists in sequentially generating onto the DM each of the  $N$  modes<sup>1</sup>, and for a given mode, recording  $P$  images, each of these images corresponding to a known amplitude or bias. The image sharpness metric is calculated for each of these images, and using a model, the mode amplitude maximising the sharpness function is then determined. The model of the metric variation with the aberration amplitude can be a parabola [10], the square root of a Lorentzian [59] or more simply a simple Gaussian or Lorentzian [39]. Two optimisation configurations are described in [59]. The first one is called  $[(P - 1)N] + 1$ , and consists in determining each mode amplitude one after the other without taking into account the previous optimum. The global optimised shape is assessed at the end, by taking the RMS sum of each individual mode. As the amplitude corresponding to the position 0 is used in each mode<sup>2</sup>, a single image corresponding to this position is needed (the "+1" in the name refers to this image). As a result, the total number of

<sup>1</sup>generally Zernike, Lukosz or DM mirror modes defined by the mirror geometry

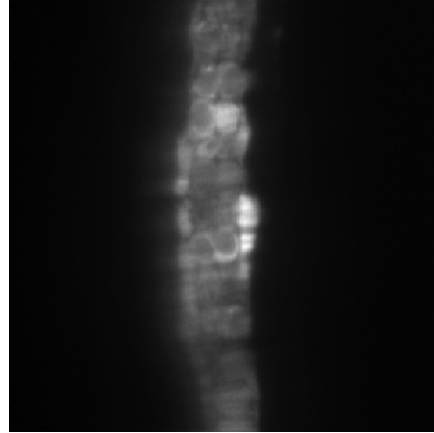
<sup>2</sup>this is possible, of course, only for an odd number of images: 3, 5, 7 ...



(a) Metric value versus number of image evaluation



(b) Simulated image before optimisation



(c) Simulated image after optimisation

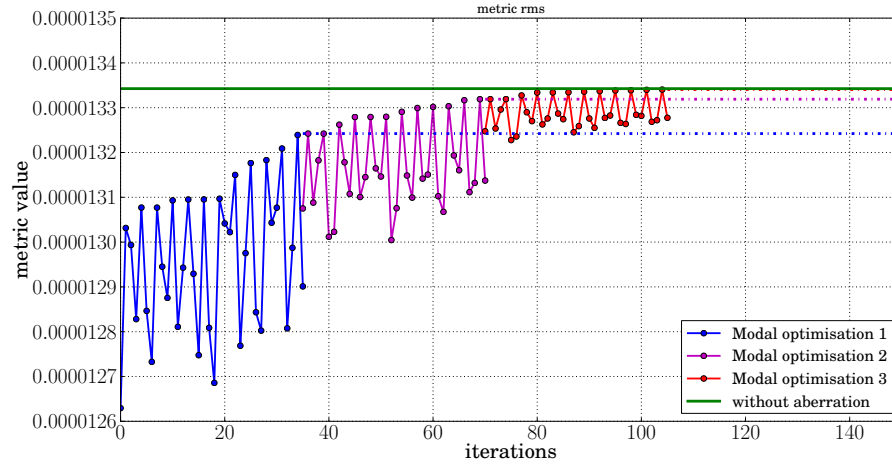
Figure 3.13: Simulation of a modal simplex optimisation

required images is (P-1) for each mode. The other configuration, called PN actually takes into account the correction calculated for the previous modes when determining the mode amplitude which maximises the metric. This configuration is actually better when it comes to real experimental set-ups because the inaccuracy in the mode reproduction by the DM is, in fact, taken into account in the optimisation process. In other terms, the intermodal crosstalk effect on

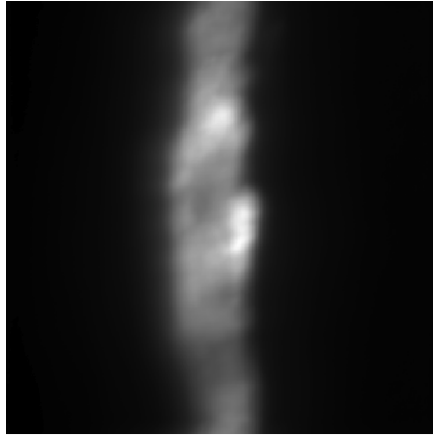
the final result is reduced. In this thesis, when "modal optimisation" will latter be mentioned, we will refer to this PN configuration.

In Figure 3.14(a), 3 consecutive modal optimisations based on 12 modes and 3 images per mode have been performed on the same aberrated image and taking into account the same wavefront distortion as the one described in 3.13. The model used was a Lorentzian.

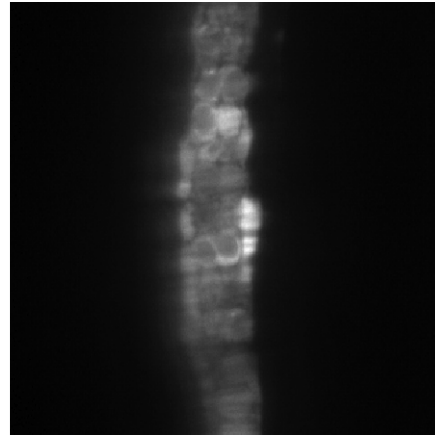
The modal optimisation, compared to the simplex appears to be faster and more accurate. Where it takes 150 iterations for the simplex to reach the optimum, which in fact leads to a metric value slightly under the one computed on the image without any aberrations, it takes only 73 iterations for the PN modal optimisation to reach the same level of correction as the simplex and 110 iterations for a complete correction. After the first optimisation run, the maximum metric value (computed on the aberration free image) is not yet reached because the model used for the metric, does not reproduce accurately enough the real variation with the level of blur.



(a) Metric value versus number of image evaluations



(b) Simulated image before optimisation



(c) Simulated image after optimisation

Figure 3.14: Simulation of a modal PN optimisation



## Chapter 4

# AO Brightfield transmission microscope

### 4.1 Introduction

Brightfield transmission microscopes are interesting because they constitute the simplest microscope architecture and, in that way, make a perfect and well-defined system to study image optimisation based on sharpness metrics.

The experimental results presented in this chapter aim to help to better understand the behaviour of image sharpness metrics and their suitability for optimisation. Although obtained on a brightfield transmission microscope, the analysis can be extended to AO fluorescence microscopes, which use the same image optimisation methodology. The main advantage of performing these tests on a non-fluorescent microscope is that there is no photobleaching issues. As a result, it was possible to conduct a large number of optimisations and follow a statistical approach without any variations induced by photobleaching effects

leading to misinterpretation.

The chapter is divided into 2 parts. In the first part, a computer simulation was used to understand the behaviour of 5 sharpness metrics when applied to a range of reference images obtained with a brightfield transmission microscope. In particular, we studied the influence of the blur level<sup>1</sup>, the image content and finally the noise level on the metric function. The second part describes some experimental results obtained with an AO brightfield transmission microscope employing a simplex algorithm for optimisation. Firstly, we investigate the effect, on the optimisation performances, of using 2 different sets of variables: either the DM actuators or the modal coefficients of the aberration produced by the mirror. Secondly, using the modal coefficient as variable, we study how the system performance is impacted by the choice of the optimisation starting points. We use, in particular, low order Zernike modes, which are likely to be part of a sample or system aberration. Finally, using experimental results obtained with the brightfield microscope, we consider the quality metric used to optimise the image and investigate whether different types of metric are more efficient than others. We confirm some of the finding obtained in the simulation part.

### 4.1.1 Test images

In the following simulation, all of the metrics are tested on some reference images and their negative. The image negatives are also produced and compared with the view of investigating the contrast reversal property of the metric. All of the 3 images are 511x511 pixels, 32 bits, and normalised between 0 and 1. They are brightfield images taken on various samples selected for their diversity in content, histogram and spatial frequency. Image 4.1(a) is a section of melanin patches of 4-5 microns of thin back-skin mouse tissue, which will be also used in

---

<sup>1</sup>blur level refers to the strength of the aberration which affects the imaging

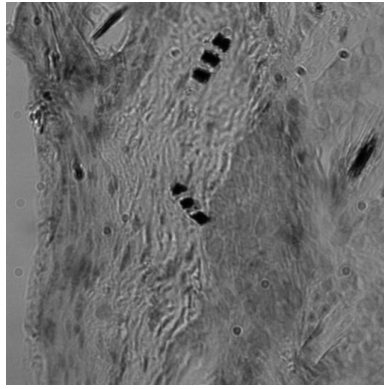
the experimental part of the chapter. Even if this sample has no real biological interest, these spots are interesting due to their high contrast. Image 4.1(c) represents the pigment patches which are present in some of zebrafish's tissues. In this case, the image has been taken from a 4-days old ex-vivo zebrafish embryo placed in a water tank container. In brightfield, the fish looks mainly transparent, except for these pigmented patches. This image is composed of 2 distinctive areas, a highly contrasted one with sharp features, and a high spatial frequency region on the right with relatively low contrast. Finally, Image 4.1(e) represents the structure at the end of the tail of the zebrafish. As for the previous image, it has also been imaged on the same zebrafish embryo. The image has a distinctive periodic pattern.

For each of the 3 images (4.1(a),4.1(c),4.1(e)), we computed the negative (4.1(b), 4.1(d),4.1(f)) and tested them in the simulation.

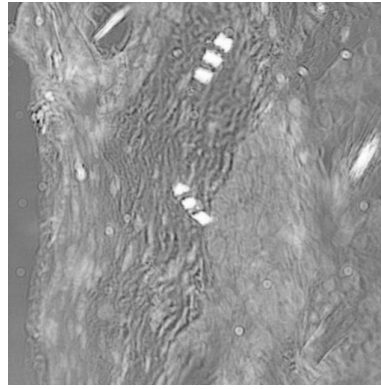
### 4.1.2 Image sharpness metric

Five metrics are used and compared in the simulation and experimental part. Metrics are given in table 4.1. All of these metrics have been previously described in chapter 2. They have also been normalised to the image total intensity, so they were insensitive to the illumination intensity variation. This characteristic is particularly important in brightfield transmission microscopes, where the total intensity of the image can change within the course of an optimisation, due to illumination fluctuations or with sample/image motion, if the DM produces tip and tilt for example. The functions were selected based on providing a range of different types of metric, whilst also covering the most common metrics.

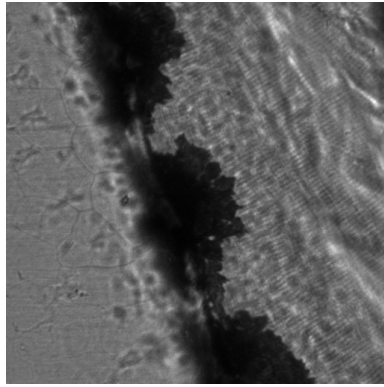
The intensity squared sharpness metric and standard deviation of the image are metrics which apply directly onto the image, without any pre-processing.  $I_p$  is



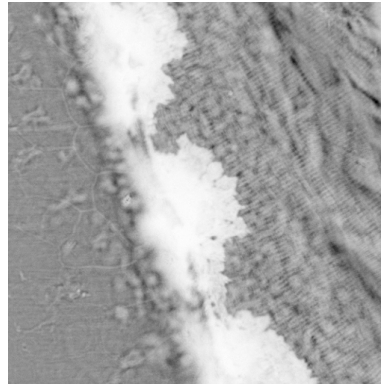
(a) patches of melanin in mouse backskin tissue



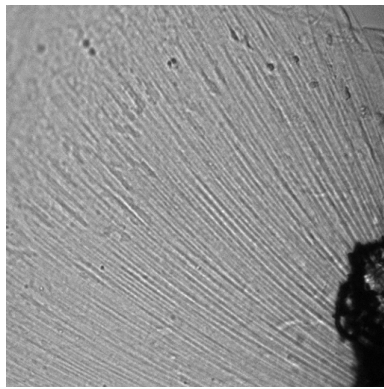
(b) Inverse of Image 4.1(a)



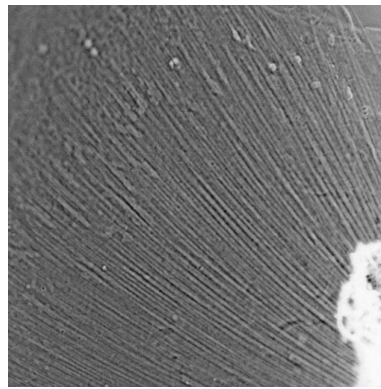
(c) pigmented tissues in a Zebrafish



(d) inverse of Image 4.1(c)



(e) Zebrafish tail structure



(f) Inverse of Image 4.1(e)

Figure 4.1: Images used in the simulation

the intensity at pixel  $p$ ,  $\langle I \rangle$  is the average grey level of the image,  $N$  is the number of pixels. The other metrics require some pre-processing of the image. The Fourier filter metric is the ratio of the high-pass filtered power spectrum over the unfiltered power spectrum of the image.  $\mathcal{F}$  is the Fourier transform symbol. The mask used in this case, is a square mask of 5 pixels centered on the spatial frequency origin. The edge detection metric based on the Sobel filter, is calculated using the first derivative of the image whose approximation is obtained by the convolution of the image with 2 ( $3 \times 3$ ) kernels,  $S_x$  and  $S_y$  given by,

$$S_x = \begin{bmatrix} -1 & 0 & +1 \\ -2 & 0 & +2 \\ -1 & 0 & +1 \end{bmatrix} \quad S_y = \begin{bmatrix} -1 & -2 & -1 \\ 0 & 0 & 0 \\ +1 & +2 & +1 \end{bmatrix}.$$

Metrics based on the wavelet filter are assessed using the python package "PyWavelets", and the wavelet used was the built-in wavelet 'db2'. The numerator gives an estimation of the high frequency content while the denominator reflects the low frequency content of the image after a 3 level decomposition calculated with the horizontal and vertical details (HL and LH).

## 4.2 Analysis and comparison of the metrics with simulation

In this section, we present results based on a computer simulation describing the behaviour of 5 sharpness metrics when tested with different level of blur, noise, and image content. Firstly, we evaluate the metric response to an increasing aberration amplitude (defocus (2,0)), and compute the associated sensitivity using a customised criteria. Secondly, the metric response to image content is

Metric name	Analytical formulation y
Intensity squared	$\frac{\sum_{pixels} I_p^2}{\left(\sum_{pixels} I_p\right)^2}$
Standard deviation	$\sqrt{\frac{\frac{1}{N} \sum_{pixel} [I_p - \langle I \rangle]^2}{\sum_{pixels} I_p}}$
Fourier Filter	$\frac{\sum_{pixel}  \mathcal{F}[I_p]_{masked} }{\sum_{pixel}  \mathcal{F}[I_p]_{unmasked} }$
Sobel Filter	$\frac{\sum_{pixels} \sqrt{(S_x * I)^2 + (S_y * I)^2}}{\sum_{pixels} I_p}$
Wavelet Filter	$\sqrt{\frac{\sum_{pixels} (LH^2 + HL^2)}{\sum_{pixels} I^2 - \sum_{pixels} (LH^2 + HL^2)}}$

Table 4.1: Metrics used in the simulation and experimental part of this chapter.

investigated. In particular, we apply the 5 metrics onto the 3 reference images and their associated negatives, and compute the dispersion in the metric value. Finally, we investigate the influence on the 5 metrics of an uniform noise applied to the reference images, and identify, by way of this, their potential performances in an AO system in presence of noise.

#### 4.2.1 Metrics as a function of blur level

In this section, we investigate how the 5 different sharpness metrics vary with the level of defocus and compare their respective sensitivity. In order to quantitatively measure the sensitivity, we analytically define it as the derivative of the metric with respect to blur. Plots on Figures 4.2(a), 4.2(c) and 4.2(e) represent the metric variation with blur respectively calculated for Figures 4.1(a), 4.1(c) and 4.1(e). The corresponding plots for sensitivity are given on Figures 4.2(b),

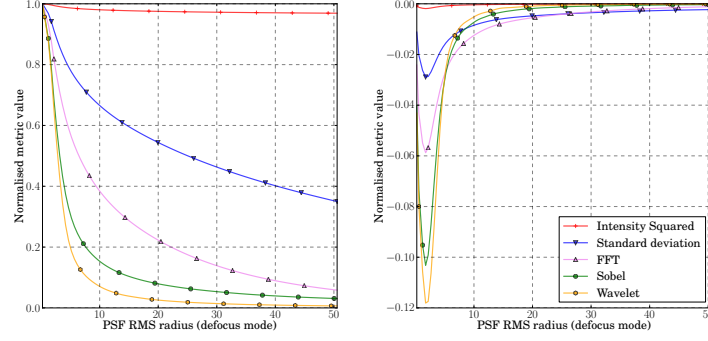
4.2(d) and 4.2(f). Plots on Figure 4.2 show that:

- There are 2 regimes: At low level of blur, for PSF RMS radii under 7 pixels, all metrics have a stronger sensitivity. For higher level of blur, beyond 7 pixels RMS, the sensitivity remains rather low.
- All metrics have their maximum sensitivity for a PSF RMS radius between 1 and 2 pixel. For this level of blur, we can expect to have the optimal metric response to aberration and hence fastest AO correction.
- Under 7 pixels RMS, edge detection metrics (i.e. Sobel and Wavelet based metrics) have the highest sensitivity.
- Beyond 7 pixels RMS, the standard deviation of the image and the Fourier filter metrics are the most sensitive and an interesting characteristic is that they keep the same level of sensitivity over a large range of blur.
- The intensity squared metric does not show very high sensitivity in any of the regimes.

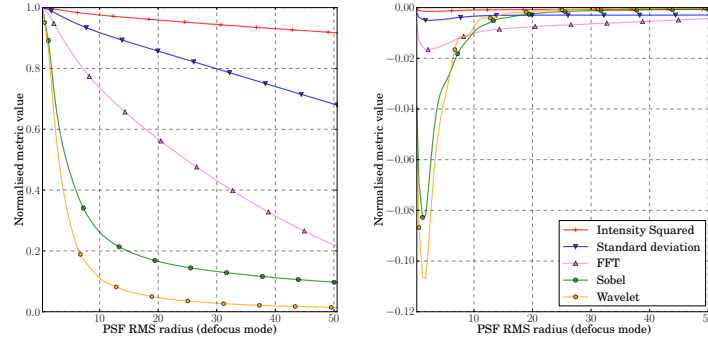
### 4.2.2 Metrics as a function of image content

In this section, the metric sensitivity to the image content is investigated. Ideally, the perfect metric exhibits the same variation on any images on which it is calculated, over a large blur range. The variation of each of the metric is investigated and compared when measured on different images. The plots are given on Figures 4.3(a) to 4.3(e).

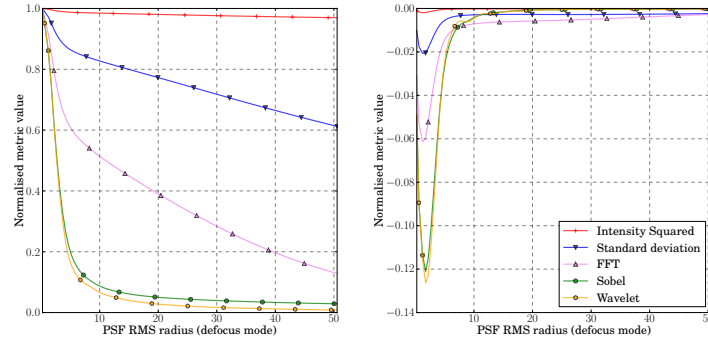
The dispersion, described by eq. (4.1), reflects the maximum deviation in the metric value when computed on the set of test images, and this deviation is also compared relative to the image blur by dividing it with the largest metric



(a) Sharpness metric variation with (b) Derivative of the plots given in the level of defocus, on Image 4.1(a) Figure 4.2(a)



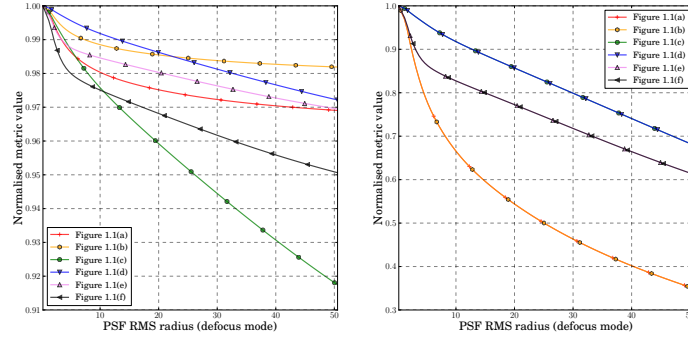
(c) Sharpness metric variation with (d) Derivative of the plots given in the level of defocus, on Image 4.1(c) Figure 4.2(c)



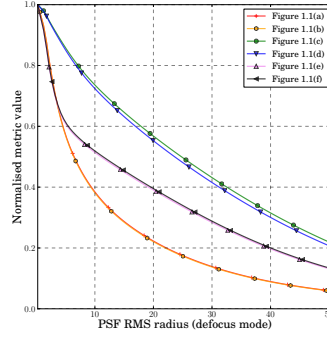
(e) Sharpness metric variation with (f) Derivative of the plots given in the level of defocus, on Image 4.1(e) Figure 4.2(e)

Figure 4.2: Sharpness metric variation with level of defocus. For comparison the Airy disc diameter is 2.44 pixels, and the RMS radius is 0.64 pixels.

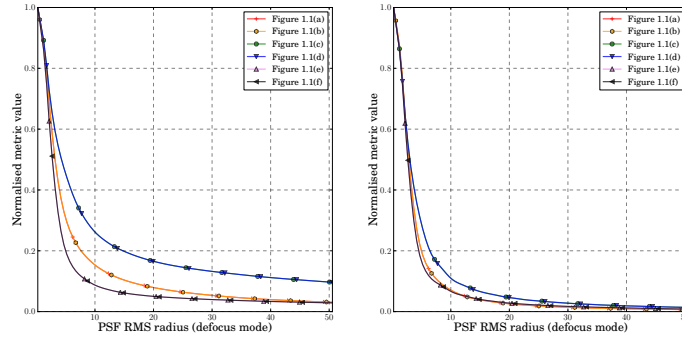




(a) Intensity squared metric variation with image content (b) Standard deviation metric variation with image content



(c) FFT metric variation with image content



(d) Sobel metric variation with image content (e) Wavelet metric variation with image content

Figure 4.3: Sharpness metric variation with image content. For comparison the Airy disc diameter is 2.44 pixels, and the RMS radius is 0.64 pixels.

variation obtained within the range of image. The dispersion is:

$$dispersion(r) = \frac{[\max(m_i(r)) - \min(m_i(r))]}{1 - \min(m_i(r))}, \quad (4.1)$$

with  $m_i(r)$  being the metric value computed on the  $i^{th}$  image at RMS radius  $r$ .  $\max(m)$  and  $\min(m)$  are respectively the maximum and the minimum metric value obtained for the set of images. This dispersion depends, of course, on the type and on the number of images considered in this simulation. We used here a limited set of images (6, including the negative) and the result may slightly differ for a larger set of images. However, given that the test images are typical of brightfield microscopes and that they cover a variety of histograms and diversity in their spatial frequency content, the results draw general tendencies on the metric behaviour with respect to image content.

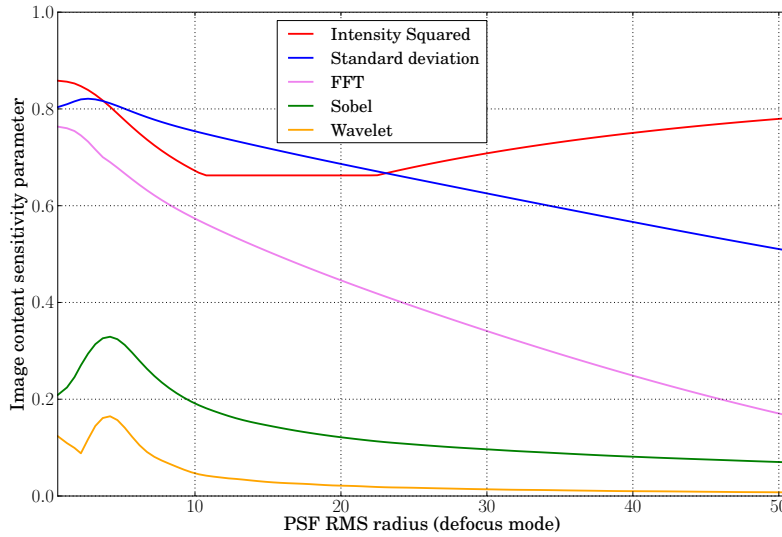


Figure 4.4: metric dispersion with image content, as per eq. (4.1), as a function of PSF RMS radius. For comparison the Airy disc diameter is 2.44 pixels, and the RMS radius is 0.64 pixels.

Figure 4.4 shows that:

- The intensity squared and standard deviation are less robust to image content variation. The dispersion remains above 50% for a PSF radius within the range [ 0-50] pixels RMS.
- The Fourier based metric is also highly sensitive to image content for low level of blur ( $< 15$  pixels RMS). Beyond this limit, the strong modulation in the image prevents the metric from being able to reveal structure in the image.
- Finally, the metric based on edge detection seems to be relatively insensitive to image content with dispersion below 50% for the full blur range [0-50] pixels RMS.

Except for intensity squared metric, all metrics are insensitive to contrast reversal. As each pixel value is real and positive, the square of the sum, in the metric analytical formulation, is always larger than the sum of the squared pixels' values. As a conclusion, the intensity square metric is not really appropriate for brightfield AO systems and more generally for complex image structures, and should be restrained to optimisation on bright spot image on a dark background.

### 4.2.3 Metrics as a function of noise

In the final part of this simulation, we investigate the effect of noise on the metric function. In a brightfield transmission microscope, the noise is usually not an issue because the illumination intensity can be adjusted. However, it is more problematic in fluorescence microscopes, where it is generally set by a number of contributors such as the number of ballistic photons reaching the detector (Poisson distribution), the presence of aberration, and the background. The discussion and the results in this section, should remain valid and relevant, for other types of microscopy including fluorescence microscopy. The aim in this

simulation, is not to reproduce the exact noise conditions in a microscope, by incorporating a realistic model<sup>1</sup>, but rather in trying to be as general as possible by applying a uniform noise over the full histogram with increasing amplitude. We are particularly interested in understanding how the noise could affect the metric function and subsequently its sensitivity to aberrations. In the following simulation, each image, which is normalised between [0-1], is then summed with an image of an uniform noise. The uniform noise has a flat histogram over the range  $[0 - \sigma]$ , where  $\sigma$  corresponds to the upper limit of the noise grey level. Noise and blur have a combined effect on the image histogram and subsequently on the metric value. Figure 4.5 illustrates how both effects separately affect the histogram. The blur tends to narrow the histogram around the average value and the noise, in our case considering uniform distribution, tends to flatten the histogram.

In Figure 4.6, the 5 normalised metrics are plotted as functions of increasing blur in presence of different level of noise in the image 4.1(a). For each noise level, a statistical evaluation of the metric based on 20 measurements is done. Each plot displays the average, with the error bars ( which are relatively small) corresponding to the standard deviation. On Figure 4.7, the metric sensitivity is shown, with a constant offset added for clarity. For each level of noise, the y axis origin is represented by a dashed line.

The addition of noise on the image leads to 2 noticeable effects. The first effect is the reduction of the metric sensitivity to blur with increasing noise. The maximum sensitivity around 3 pixels RMS is gradually decreasing until it disappears when the noise amplitude becomes similar to the highest grey level in the image. The second effect is the broadening of the error bars which reveals that, for a changing noise pattern, between 2 frames, the metric gives a different

---

<sup>1</sup>A Poisson noise distribution would not affect the bright and dark part of the image in the same ways leading to further complexity in the interpretation

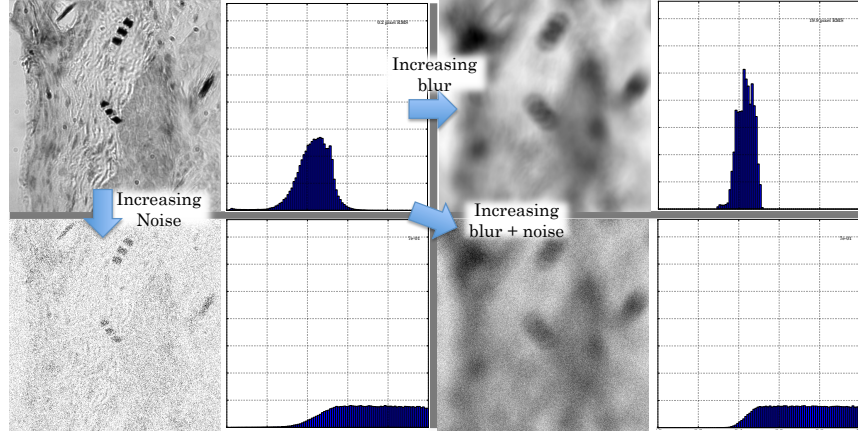


Figure 4.5: Blur and Noise effect on the image histogram. The blurring of the image has been done with a defocused PSF of 28 pixels RMS, and the noise added to the image is uniform within the grey level range  $[0, 0.7]$ . The initial image was normalised to 1. All histogram plots have a vertical axis ranging from 0 to 38200 (images are 511x511 pixels) and the horizontal axis representing the grey level, is between 0 and 1. A number of bin of 100 is used.

value leading to error in the interpretation of the N dimensional metric function inducing ultimately a failure in the optimisation.

Metric based on edge detection, such as Sobel and Wavelet are significantly sensitive to noise, as can be seen in Figures 4.6(d) and 4.6(e). Beyond 7 pixels RMS, the amplitude of the variation is strongly affected. In Figure 4.6, the normalised metric variation spans between  $[0 - 1]$  without any noise. In the presence of a low level of noise (brown plot) which affects 10% of the total dynamic, the normalised metric variation is now limited to the interval  $[0.6$  or  $0.7 - 1]$  implying that blur level beyond 7 pixels will not be easily corrected for an AO system using these metrics in these noisy conditions. The intensity squared, standard deviation and the FFT filter metrics present similar behaviours with respect to the noise. For a noise level of 30% of the initial image dynamic (orange plot), the sensitivity limit for these 3 metrics appears to be around 28

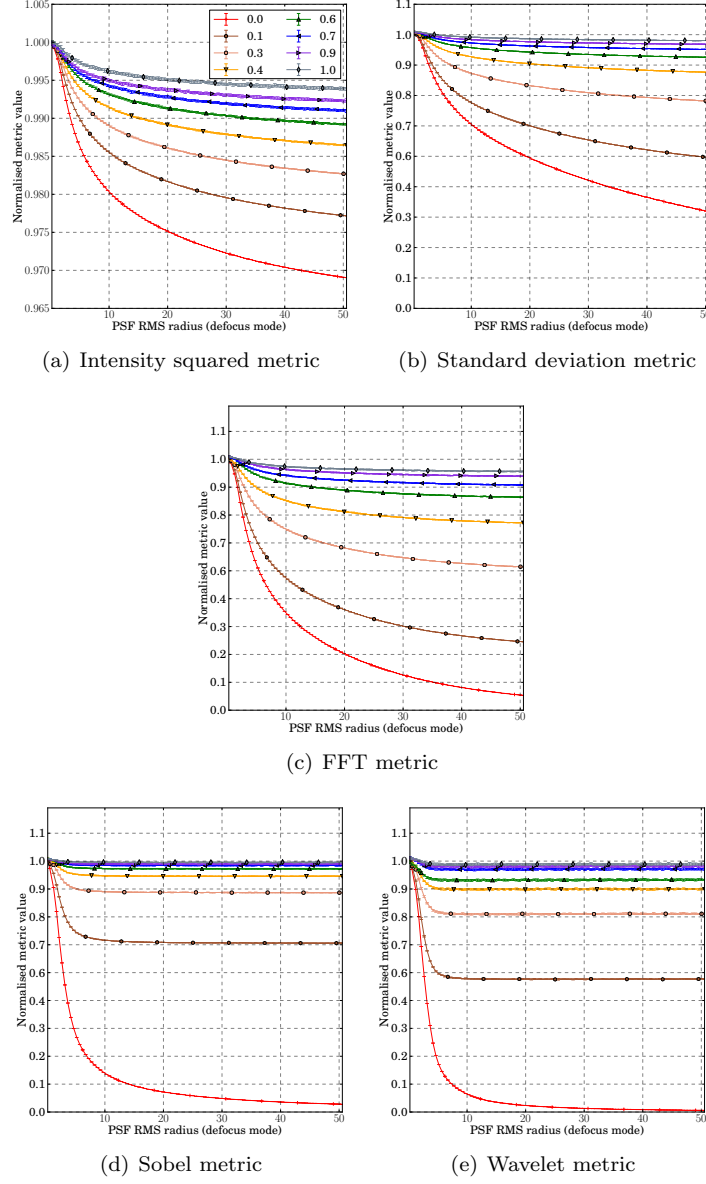


Figure 4.6: Sharpness metric variation with a uniformly distributed noise and defocus when applied to image 4.1(a). The colour code corresponds to the upper limit of the uniform distribution. For example, for one (grey plot), the noise is uniform in the grey level range  $[0 - 1]$ . The plots display the average of 20 values and the error bars correspond to the standard deviation. The error bars remain very small, with a maximum of 2% for Sobel and wavelet metrics.

pixels RMS. These metrics will be favoured for optimisation on noisy images. Finally, the effect caused by the broadening of the error bars, which reflects the frame to frame variation due to the noise, remains negligible in comparison with the loss of dynamic.

### Conclusion

This analysis by simulation of 5 commonly used metrics has revealed the different metric characteristics regarding the level of blur, image content and noise sensitivity. In particular:

- Each of the 5 selected metrics has a specific sensitivity to blur. The intensity squared metric is the less sensitive and has a maximal relative variation of less than 10% for PSF radius RMS variation up to 50 pixels. Most sensitive metrics are based on edge detection with a maximal relative variation greater than 99% for the same PSFs range.
- The maximum sensitivity for all metrics is around 2 pixel RMS. Their sensitivities tend to decrease beyond 7 pixels RMS.
- Metrics based on edge detection tend to be less sensitive to image content. This result is also experimentally confirmed in chapter 6 where it is shown that the accuracy of the wavefront measurement in presence of image motion, induced by the residual jitter in the heart synchronisation is optimal when indirectly obtained with the use of a Sobel metric. Intensity squared metric is contrast reversal and content dependent. The use of this metric is not recommended on brightfield transmission microscopes, and should be restricted to images of bright spot on dark background. The image content analysis presented here has been conducted on a limited number of images, and should be extended to a larger range of images in order to confirm the tendencies.

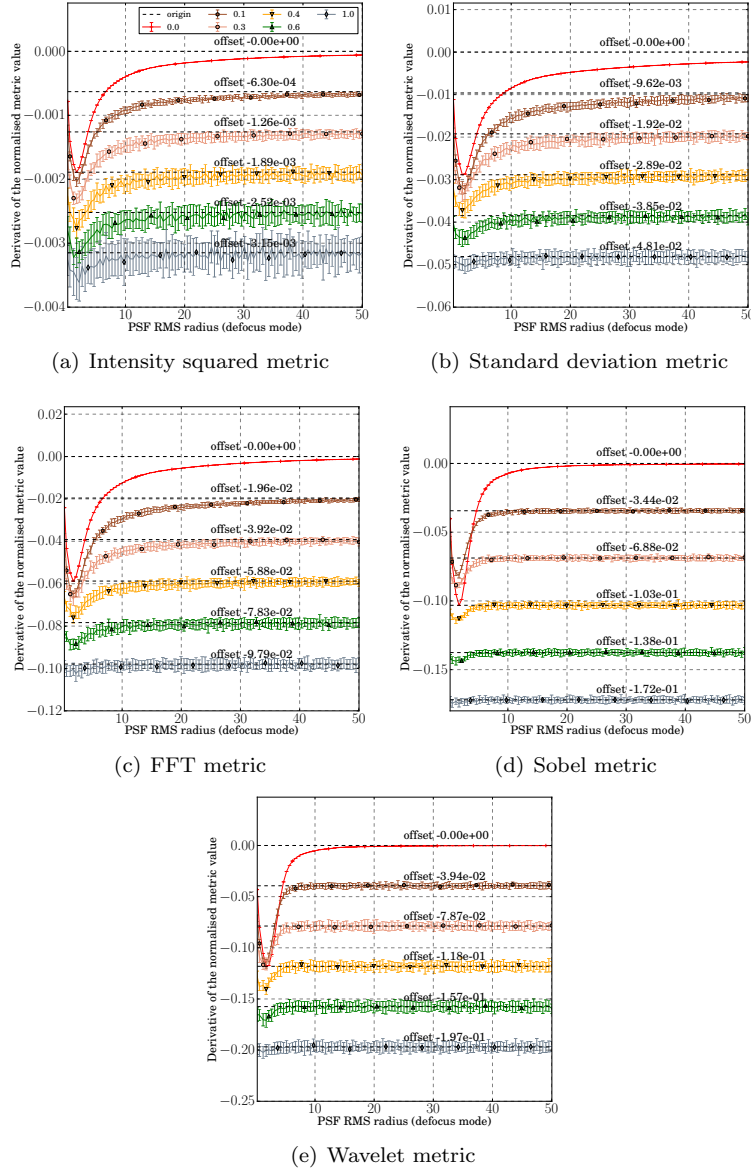


Figure 4.7: Sensitivity to blur, in presence of noise, assessed in Figures 4.6(a) to 4.6(e).

- The addition of noise to image induces a loss of image blur sensitivity. This effect is significant for metrics based on edge detection even for a small levels of noise ( $< 10\%$  of the dynamic). Beyond 7 pixels RMS of



blur, the edge detection metrics have lost all of their sensitivities and have become useless for optimisation. In the presence of noise, a Fourier filter or a standard deviation metrics will be favoured due to their large range of sensitivity and noise robustness.

### 4.3 Experimental comparison of the 5 sharpness metric

In this section, we experimentally compare the 5 metrics using AO based on image optimisation involving a simplex algorithm applied to a brightfield transmission microscope.

#### 4.3.1 Optical setup

The wavefront sensorless AO transmission microscope layout is given in Figure 4.8. A blue LED (emission peak 470nm) is used to illuminate from behind a 4-5  $\mu\text{m}$  thick mouse backskin tissue stained with hematoxylin and eosin. The skin sample is fixed in 4% PFA, dehydrated, and embedded in paraffin. 4-micrometer sections were cut with a microtome. The light is collected through a Nikon S-Plan Fluor (x40, 0.6 NA) microscope objective (MO) with a 2mm working distance, relayed onto an Imagine Optics mirao 52-e deformable mirror (DM), with 52 actuators and aperture  $\Phi = 15\text{mm}$ , via 2 lenses  $f_1 = 200\text{ mm}$  and  $f_2 = 400\text{ mm}$ , ensuring a conjugation between the microscope back aperture and DM surface. An image is formed onto a science camera (Retiga 1300 - Qimaging camera) via a  $f_3 = 200\text{mm}$  lens. Although the system works in a sensorless configuration, i.e. the DM feedback is based on the images acquired by the camera, a Shack-Hartmann wavefront sensor (WFS) is used for the mirror calibration. The WFS analyses an HeNe laser beam (632nm), which is injected

and extracted from the set-up via 2 dichroic plates ( $D_1$  and  $D_2$ ). The WFS measurement which is not used in the optimisation loop, allows the calibration of the WFS response and interaction matrices, which are then exploited to generate Zernike modes onto the DM. The WFS is conjugated with the deformable mirror via  $f_2$  and  $f'_1 = 75\text{mm}$ . The beam arriving on the wavefront sensor has been reduced to allow an optimised sampling by the microlens of the wavefront sensor in order to increase the speed of the system.

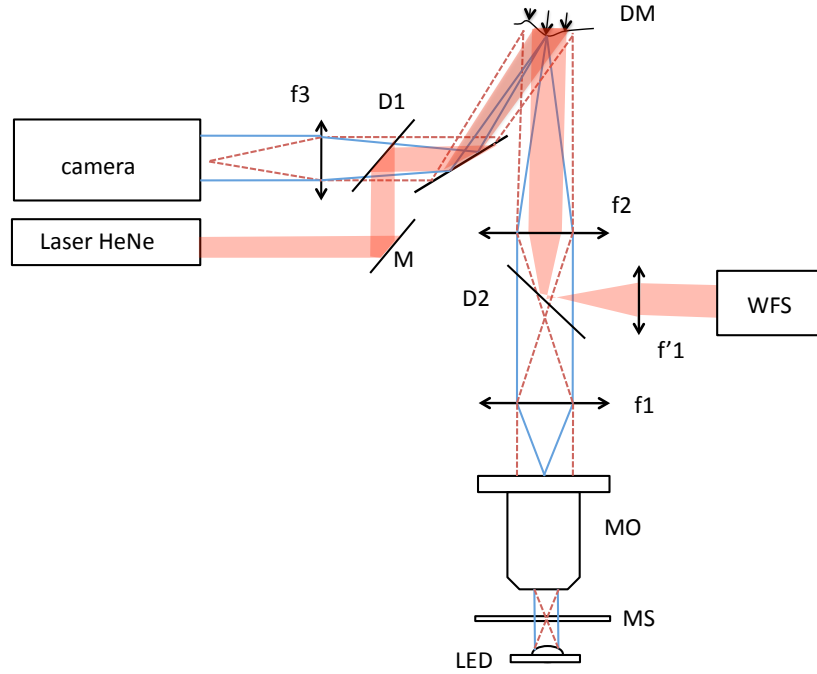


Figure 4.8: A wavefront sensorless AO transmission microscope with a bright-field illumination.

### 4.3.2 Simplex optimisation configurations

The optimisation route is set by a Nelder-Mead simplex algorithm which has been discussed in section 3.2.3. One characteristic of the simplex is that the solution of the optimisation is partly defined by the optimisation starting points.

The convergence time and performance can then vary from one optimisation to another. In this experimental part, we investigate how the choice of the starting points influences the performance and quality of the solution, and 2 optimisation configurations are compared:

- optimisation starting from totally random points
- optimisation starting from a mix of low order Zernike modes, each of them defined with a random amplitude

In addition to testing the effect of selective starting positions on the optimisation performance, we also investigate 2 sets of variables during the simplex optimisation:

- Variables being the 52 DM actuators
- Variables being the amplitude of the first 14<sup>th</sup> Zernike modes (excluding the piston)

To test these two effects (influence of starting points and variables) on the simplex performance we experimentally set up 3 simplex configurations that we tested :

1. Optimisation using the simplex with random starting points optimising on the actuator voltage's variables (later referred as type 1)
2. Optimisation using the simplex with Zernike modes as starting points optimising on the actuator voltage's variables (later referred as type 2)
3. Optimisation using the simplex with Zernike modes as starting points optimising on mode vector's variables (later referred as type 3)

By comparing configurations 1 and 2, we are able to study the influence of the starting points on the optimisation performance, as both optimisations are

run with the same type of variables. By comparing configurations 2 and 3, we can analyse the influence of the type of variables, as both optimisations are run with the same starting points.

### Implementation of the 3 configurations in a brightfield transmission microscope

The 3 configurations were experimentally tested and compared on the same image of melanin dots in back skin mouse tissue (the region of interest is the red box on Figure 4.9) using the image standard deviation metric. Ten optimisations per configuration were carried out to test the repeatability of the algorithm convergence and a statistical analysis was then performed.

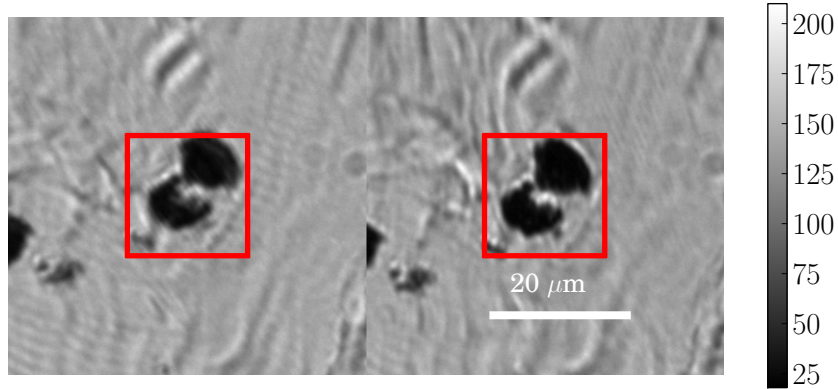


Figure 4.9: Typical optimisation with "before" image on the left and "after" image on the right. The white scale bar corresponds to 20  $\mu\text{m}$

Figure 4.10 shows, for the 3 configurations, the average of the 10 metric values at each algorithm iteration, normalised to the metric value before optimisation. The error bars correspond to the standard deviation and give a representation of the repeatability of the optimisation over 10 runs. Once the optimisation has started,  $N+1$  starting positions are computed (with  $N$  being the number of variables). For configurations based on actuator variables (type 1,

blue plot and type 2, green plot) which require inherently more starting points, this initial step takes slightly longer than for the optimisation based on modal coefficient variables (type 3, red plot) which only involve 15 variables. The type 3 configuration presents the fastest convergence in about 200 iterations. However, the metric calculated on the solution was slightly lower than the 2 other configurations. This is explained by the fact that, as less degree of freedom is left for investigation, the solution, in this case was a coarser version of the one using the actuators as variables. The modal optimisation using actuators as variable (type 2 in green) reaches a stable solution after 600 iterations. Finally, the optimisation based on random starting points and using mirror actuators as variable (type 1 in blue) reaches the highest metric value after optimisation but requires more iterations (about 800).

Figure 4.11(a) shows the typical system aberration that was corrected by the algorithm. The aberration amplitude is about 4 times as large as the diffraction limit and is mainly composed of astigmatism. In Figure 4.11(b), the first 14<sup>th</sup> Zernike coefficients are given for the 3 configurations. The tip  $(1, -1)$  and tilt  $(1, 1)$  are prevailing. The production of tip and tilt results in a shift of the image with respect to the optimisation window. On the type 1 configuration, totally random starting points were used and these random shapes included a varying amount of tip and tilt. This led to solutions with also larger amounts of tip and tilt. As no tip and tilt were added to DM starting shapes for the type 2 and type 3 configurations, both solutions have a relatively small amount of tip and tilt.

### 4.3.3 Measurement of the metric relative improvement

The simulation analysis has revealed that the 5 different metrics presented different level of relative improvement ( Figure 4.2). In Figure 4.12, the relative

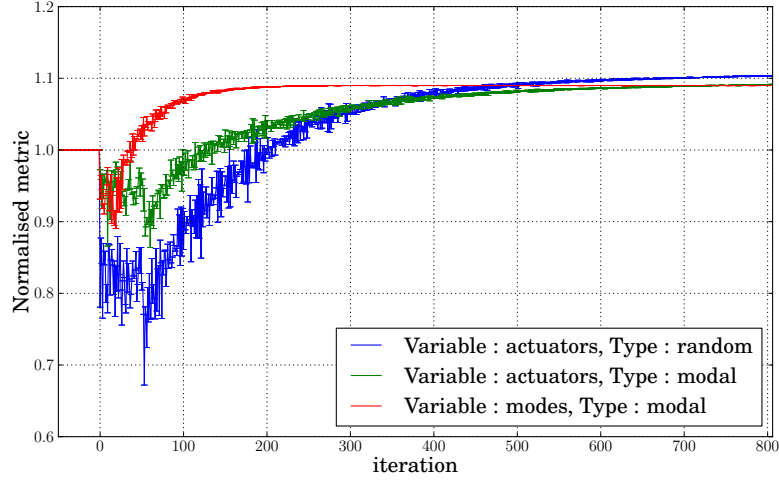
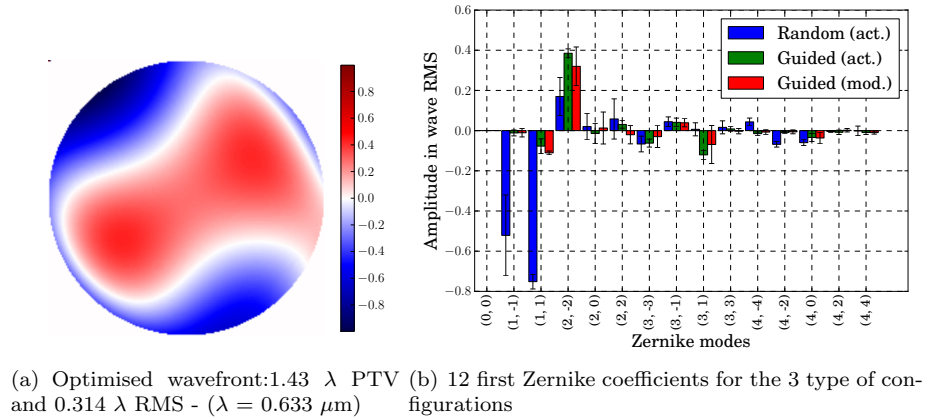


Figure 4.10: Comparison of different optimisation schemes based on the simplex algorithm using the standard deviation metric. The blue and green plots represent optimisations using mirror actuators as variables. In this configuration, we used a 52 actuators mirror. The red plot shows an optimisation considering the Zernike modes as the variables. The blue plot is using random initial voltage within the range  $\pm 5\%$  of the maximum stroke. The red and green plots are using a random set of Zernike modes including:  $(2, 0), (4, 0), (2, 2), (2, -2), (2, 2), (3, -1), (3, 1)$  each of these modes having a modal coefficient amplitude randomly chosen with a uniform distribution over the interval  $[-0.5\lambda, +0.5\lambda]$  (wave RMS).



(a) Optimised wavefront:  $1.43 \lambda$  PTV (b) 12 first Zernike coefficients for the 3 type of configurations and  $0.314 \lambda$  RMS - ( $\lambda = 0.633 \mu\text{m}$ )

Figure 4.11: Optimised wavefront map and modal coefficients

improvement of the 5 different metrics is experimentally measured and compared.

We ran 10 optimisations per metric, using the type 3 configuration. For each of the metric, the average and the standard deviation were computed.

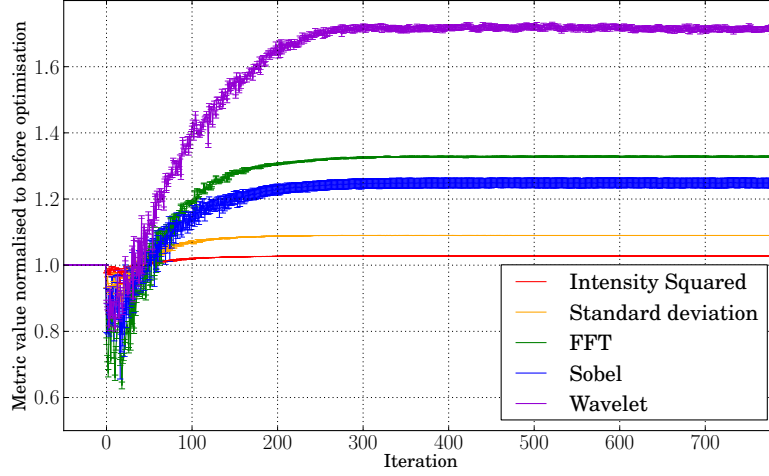


Figure 4.12: Relative improvement of the metric value for the 5 different metrics when optimising on Figure 4.9 . For all metrics, 10 optimisations have been performed and the average metric value, with its standard deviation has been plotted. All plots are normalised to the value before optimisation. The relative improvements are 2.8%, 9%, 24.8%, 32.8% and 72% respectively for the intensity squared, the standard deviation, the Sobel, the Fourier, and the wavelet based metrics.

The relative improvement is 2.8% for the intensity squared metric, 9% for the standard deviation metric, 24.8 % for the Sobel filter metric, 32.8% for the Fourier based metric, and finally 72% for the wavelet metric. The measurement of the relative improvement for each metric confirms the result of the simulation in Figure 4.2, where similar variations have been identified for PSF radii around 3 pixels RMS.

#### 4.3.4 Comparison of optimisation performances for different metrics

In this final section, we compare the sharpness after optimisation of the same image, when optimised with different metrics. To do so, 10 optimisations are run for each metric, over a small region of interest in the image (115 x 120 pixels) represented in red in Figure 4.13. In this figure, the typical before and after optimisation image are represented.

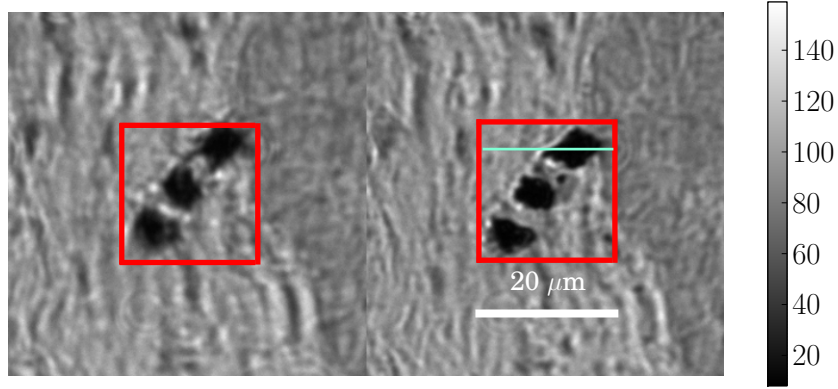


Figure 4.13: Typical Before and after image. The red square is the optimisation window, and the white scale bar corresponds to 20  $\mu\text{m}$ . The green line shows the location of the section plotted on Figure 4.16.

The average metric improvement between the image before and after the optimisation is calculated and a standard deviation is given to estimate how repeatable the optimisation is. The results, given in Figure 4.14, give the relative improvement on an optimised image with all the different metric functions. So that we could directly compare the metrics, once the image was optimised using each of the metrics, we then tested the improvement using every other metric. The horizontal axis in Figure 4.14 shows each of the metrics used for the image optimisation and, within each set of bars, the colour corresponds to metrics used for the final evaluation on the optimised image. Clearly the 5 sets of 5



vertical bars all have very different amplitudes, and this amplitude reflects the metric sensitivity as discussed previously. However, the coloured bars within each block of 5, show the 5 different metrics used to measure the sharpness in the optimised image. The height of each of the bars is very similar within each block and the relative improvement of each metric is in the same increasing order as in Figure 4.12. Although different metrics produce different percentage improvements, the overall improvement in image quality was similar in all cases. In all cases no matter which original metric was used the final metric value was the same for each metric method. When, this time the sharpness contrast of the optimised images was visually assessed, no difference was noticed between the optimised images depending on the metric used for optimisation.

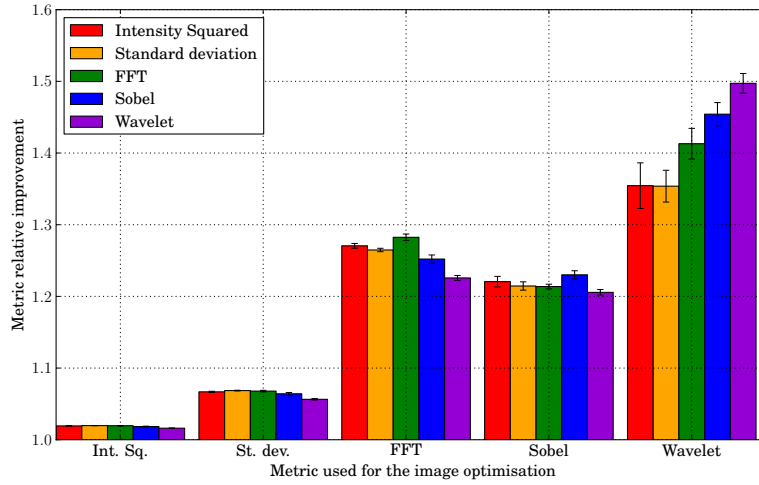


Figure 4.14: Relative improvement of the metric value for the 5 different metrics. For all metrics, 10 optimisations have been performed and the average metric value, with its standard deviation has been plotted. All plots are normalised to the value before optimisation. The horizontal axis refers to the metric which has been used for optimisation, and the colour shows the metric used for the final measurement on the optimised image.

The optimisation is also repeatable, and leads to the same mirror shape. In Figure 4.15, the mirror Zernike mode amplitudes are displayed and no large

differences can be noticed after optimising with the different metrics. The error bars correspond to the standard deviation of the amplitude after 10 optimisations (they are there to show the variation of values rather than the standard error). As for the optimisation in Figure 4.9, the main aberration is astigmatism  $(2, 2)$ . The residual focus has also been corrected.

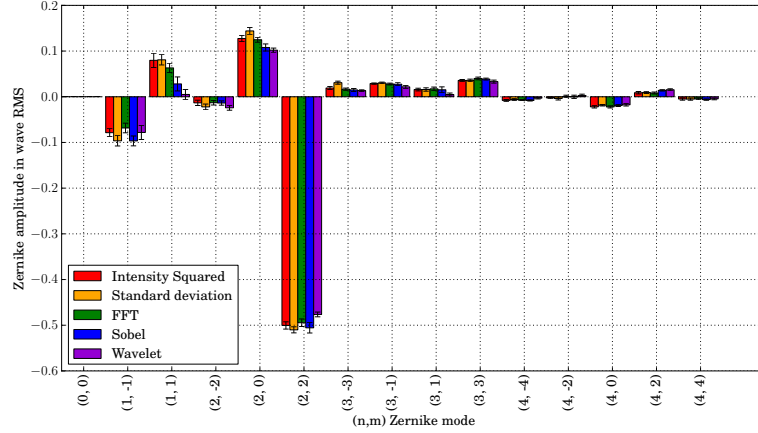


Figure 4.15: Zernike modal coefficient per metrics

A comparison of the image section is provided in Figure 4.16, and the section has been obtained at the location of the green line in Figure 4.13. The section shows a good improvement in the sharpness as the dark spot edges have become steeper. The 10 profiles before and after optimisation have been superimposed and the overlap shows how repeatable and stable the optimisation is.

## Conclusion

We have demonstrated that AO can be implemented in a wide field microscope using optimisation algorithms to determine the correct deformation to be applied to an AO mirror to remove system induced aberrations. When using a simplex algorithm, we have confirmed that the convergence speed is significantly improved when starting positions for the optimisation are carefully chosen. In

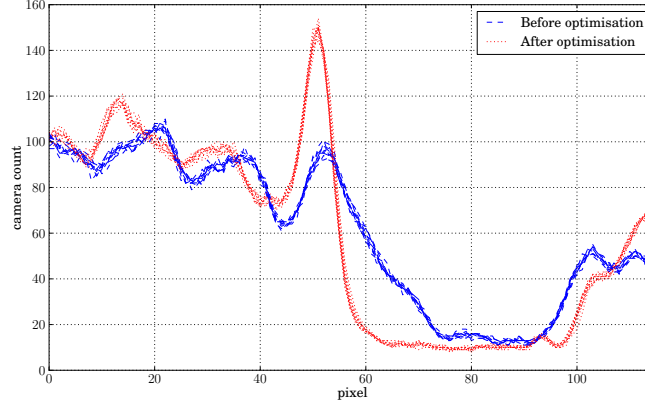


Figure 4.16: The profile before (blue line) and after (red line) optimisation performed on Figure 4.13 with the wavelet metric. The location of the profile is given on Figure 4.13 by the green line.

our case, we used a mix of low order Zernike modes as initial shape for the DM, which was more likely to be found in the phase aberration. Furthermore, we showed that the choice of modal coefficients as set of simplex variables is more opportune than using the DM actuators, because for an almost similar image quality, it leads to faster optimisation. It also offers the opportunity to remove tip, tilt and defocus, from possible solutions, as these modes would move the microscope object plane away from the sample region of interest. The experiment shows, for this particular case, all the metrics led to very similar results. When compared together, the optimised images obtained with the different metrics were very similar and no differences on visual contrast or visual sharpness were observed.

## Chapter 5

# Closed loop widefield microscope

### 5.1 Introduction

This chapter aims to experimentally compare sensorless and sensed AO configurations in a brightfield transmission microscope. In the previous chapter, we presented experimental results in a sensorless modality using a simplex algorithm and an image sharpness metric. Here, we show how this sensorless set-up can evolve to a closed loop AO microscope using light from a laser guide probe to feed the wavefront sensor. The laser can then be focused at an arbitrary position in the sample thus high resolution images from any part of the specimen can be recorded without the need for fluorescent features in the sample. We compare the operation of the system with a sensorless approach.

AO was first developed for imaging through atmospheric turbulence where light for the wavefront sensor (WFS) is gathered from either a natural or a laser

guide star. There has been much recent interest in applying these techniques to microscopy so aberrations in both the specimen and the optics can be corrected [35, 21]. Most work on microscope AO has involved image optimisation techniques, or wavefront sensorless AO [60, 23, 55]. This works extremely well, but is relatively slow and cannot easily be used on dynamic samples. More recent work has been published on full closed loop AO [48, 61, 42, 50, 51]. A major challenge for AO microscopy is obtaining a good signal for the WFS. One approach is to use a fluorescent bead within the sample [48, 42] to provide a point source, (although we note that wavefront sensing can be achieved on extended sources using correlation tracking). This type of closed loop AO is analogous to natural guide star AO, in that if the object of interest is close to the bead (axially as well as transversely) then the WFS will sense the aberrations. However, it has the drawback that one can only use the AO where there happens to be a bead. There is a further disadvantage in that the beads cannot, in general, be injected into living samples. Using light from a laser, which scatters from the specimen, is analogous to using a laser guide star, in that one can observe an arbitrary point in the sample. Light scattered from other axial positions in the sample must be rejected. This has been done using either a confocal pinhole [50] or the short spatial coherence of a pulsed Ti:Sapphire laser [51]. However, there are a number of problems with using a laser probe, which we address in this chapter. They are:

- The double path effect [62], whereby the system does not sense odd aberrations, must be corrected.
- Extra set of wavefront sensor spots coming from the reflection on various surfaces normal to the optical path.
- Null spot positions for the Shack Hartmann WFS must be defined accurately.

- Speckle noise in the WFS must be reduced.

In this chapter we demonstrate a widefield<sup>1</sup> AO corrected microscope, which uses techniques from ophthalmic AO to mitigate the double pass effect, and a vibrating mirror to reduce speckle. The system also uses wavefront sensorless AO to provide high quality nulls for the WFS, and to provide a reference to test the system.

### 5.1.1 The double path effect

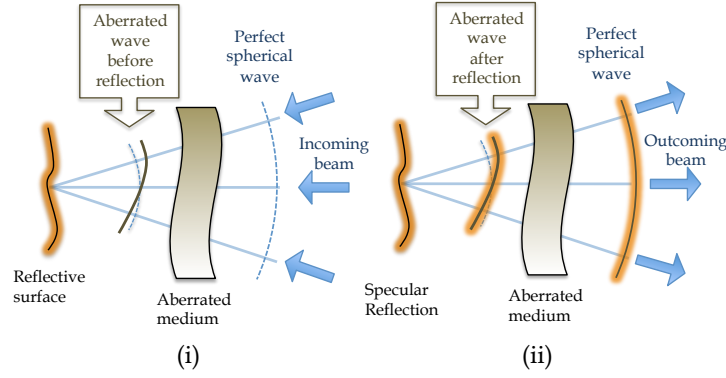
The double path effect occurs when a wavefront, distorted by an aberrated medium undergoes a reflection and a focusing, followed by a second travel through the same aberrated medium. The result is that the odd modal degree varying with aperture such as coma, trefoil etc are canceled and thus the WFS is unable to sense them. The double path effect is explained on Figure 5.1. In this figure, the problem is illustrated in the case of an odd radial degree. In Figure 5.1(a)(i), when a perfect spherical wave, in dashed blue, passes through an aberrated medium, the wavefront becomes distorted with a "coma" type aberration, represented as a deviation from the reference sphere. The top part of the wavefront has been delayed while the bottom part has moved ahead of reference sphere. The wave is then reflected by a deeper layer and we will assume here that the reflective surface is perpendicular to the optical axis, so the reflected beam is following exactly the same path as the incoming beam with an additional inversion. In Figure 5.1(a) (ii), the beam path after reflection is represented. The returning wavefront is then symmetric to the incoming one with respect to the optical axis. When travelling through the same aberrated medium, the part of the wavefront which was ahead of the reference sphere

---

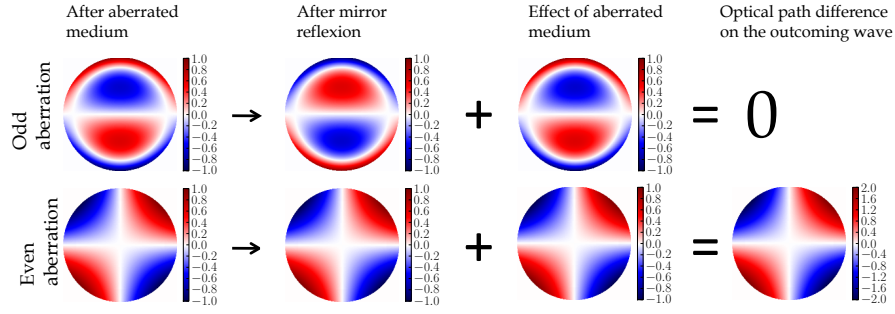
<sup>1</sup>It should be noted that we use the term widefield as defined in the microscopy community, meaning a non-beam scanned technique as opposed to widefield as defined by the AO community, which means a technique for correcting multiple heights (or depths) of atmospheric turbulence.

on the incoming way is now delayed by the aberrated medium, in the same proportion. As a result, the odd aberrations are cancelled, while the even aberrations, which are symmetric with respect to the optical axis, are doubled. In Figure 5.1(b), the odd and even aberration cases are compared and the wavefront is plotted at different locations in Figure 5.1(a). For the incoming beam, after the aberrated medium, the wavefront distortion is either coma (top line) or astigmatism (bottom line). After reflection and focusing, the wavefront is transformed to its symmetrical with respect to the optical axis, and the astigmatism (like all aberration types with an even coefficient) remains the same as before reflection. However, for odd radial degree, there is an inversion leading to a cancellation of the distortion.

This effect has been widely analysed for ophthalmic AO [62, 63] and concerns only specular reflection. In the case of elastic scattering (Rayleigh) or inelastic scattering (fluorescence), then the wavefront information from the first pass is lost and only aberrations from a single path is encoded in the outgoing wavefront. In general, depending on the sample, there is a varying proportion of specular reflection and diffused backscattering in the returned beam. Solutions have been proposed to mitigate the specular reflection. One solution is to use a small diameter laser probe, which only passes through a small portion of the pupil. On the outgoing pass [64], the scattering light which is isotropic in a  $2\pi$  space, fills the full aperture. This solution can be easily implemented on a microscope and is used in the closed-loop AO microscope described latter in this chapter. The Figure 5.2 illustrates this method, which uses a small incoming beam (the beam is not visible on the image, and located in the red square) and receives the back scattered light from the sample filling the whole aperture (green circle) as it returns.



(a) diagram of the incoming and reflected beam respectively on (i) and (ii)



(b) Illustration of the double path effect in the case of an odd (top) and even (bottom) aberration

Figure 5.1: Principle of the double path effect occurring in the case of a reflected focused beam

### 5.1.2 Ghost reflection reduction

Another issue in closed-loop AO microscopy systems using a laser guide star, is the presence of an extra set of spots on the WFS camera, generated by surfaces normal to the beam path. These additional and unwanted spots are sometimes intense, contributing to the instability and correction error of the closed loop. For example, in ophthalmic closed loop AO systems, the incoming beam is subjected to direct reflection on the cornea, which generates an extra set of intense spots on the WFS camera. A solution, which takes advantage of the cornea curvature, is to use an off-axis beam [65] which sends the reflected beam



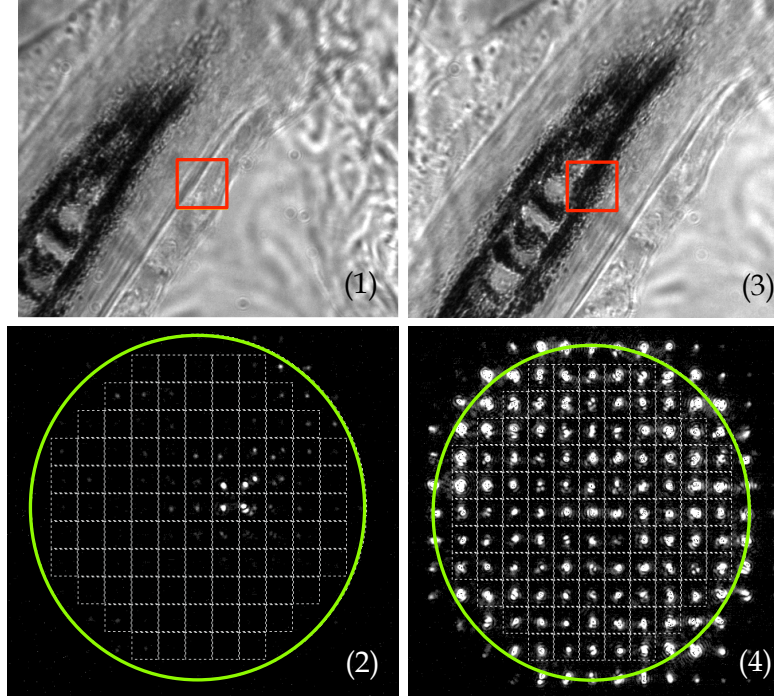
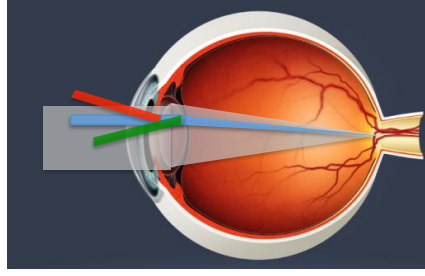


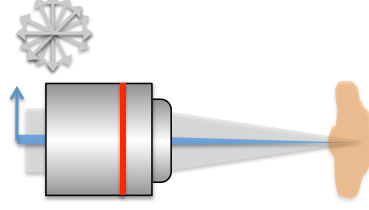
Figure 5.2: Illustration of the use of the back scattering light as a laser guide star for wavefront sensing. In (1), the beam (which is not visible) located at the centre of the red square is focused on a weakly scattered part of the sample. In (2), the wavefront sensor camera, for this position, is shown. Only a few spots corresponding to the specular reflection on the slide and the sample are present. In (3), the probe beam is now focused on a highly scattered tissue, leading, in (4), to a full covering of the WFS aperture. As no pinhole is used, the spot shape inhomogeneity is noticeable.

out of the WFS aperture (as shown in Figure 5.3(a)). In a microscope, the problem is comparable as part of the incoming probe beam is reflected from the various surfaces normal to the optical axis such as the cover slip and specimen interfaces. However, unlike ophthalmic AO cases where the stray light comes mainly from a single surface, here the beam reflection occurs all along the beam path.

We propose, here, a method using the change in light polarisation during the scattering process to discriminate the light coming from specular (direct



(a) Solution using an incoming off-axis beam. The blue beam is the incoming beams. The red and green are the reflected beams respectively on the front and rear surfaces of the crystalline, and are deflected from the pupil entrance of the wavefront sensor. The grey beam is the diffuse scattered beam created at the retina.



(b) Suggested solution using depolarisation properties of biological tissues. The linearly polarised incoming beam is focused into a biological sample. The biological tissue depolarises the beam, and the backscatter beam, in grey, is separated from the polarised incoming beam by a crossed polariser.

Figure 5.3: Ghost reflection reduction methods

reflection) and diffuse reflections (elastic scattering) as shown in Figure 5.3(b). It has been shown in [66], that the light becomes depolarised as it travels deeply through tissue. Although such a characteristic has not been observed in scattered light by the retinal surface [63, 67], it has been experimentally shown using polystyrene microspheres and biological tissues that the process increases with the optical depth. By using a polarisation beam splitter just before the back aperture of the microscope objective, the incoming linear polarised light is reflected whilst half the outgoing non-polarised light generated by the diffuse reflection is transmitted to the WFS <sup>1</sup>.

### 5.1.3 Speckle wavefront sensor spots reduction

Finally, the coherent probe beam, scattered by the tissues, creates a speckle pattern around the WFS spots, which changes from sub-aperture to sub-aperture. The disparity in the spot shape contributes to the wavefront correction error. A range of solutions have also been suggested in the literature including the use

<sup>1</sup>It has also the advantage of getting rid of the double path effect, as the specular reflection tends to conserve the polarisation state of light

of a low coherence source, an acoustic cell in [68] or a scanning mirror in [51, 65] which aim to temporally average out the residual speckle pattern around the wavefront sensor spots, creating a smooth image of them. In our closed loop AO microscope, we address this problem using a similar scanning mirror technique.

## 5.2 Optical configuration

The optical set-up is shown in Figure 5.4.

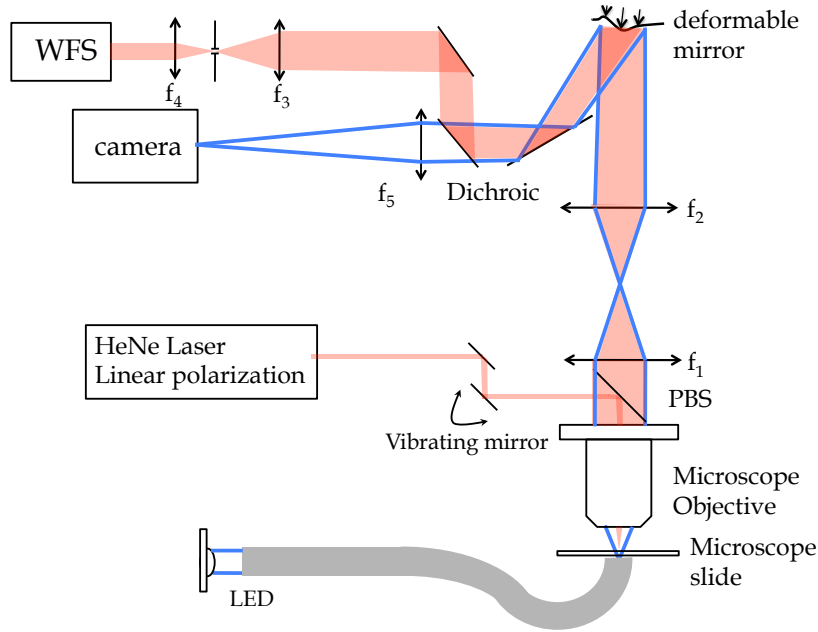


Figure 5.4: Closed-loop AO transmission microscope

The sample is a 4-5 microns thick mouse back skin tissue (C57bl6/CBA F1 mice) stained with hematoxylin and eosin. The sample is illuminated from behind by a blue LED (emission peak at 470nm) and the light is collected by a Nikon Fluor (100 times, NA 1.30) objective. We use a liquid light guide to carry the light from the LED to the sample to maximise the étendue. However, the illumination NA is less than the microscope objective collection NA and is

estimated to be 0.84. Epi-illumination was not used due to the slight complication of the laser probe coupling but could be incorporated in future designs. The back aperture of the microscope ( $\sim 5.2$  mm) is relayed through a telecentric configuration composed of 2 lenses ( $f_1 = 200$  mm and  $f_2 = 400$  mm) onto the deformable mirror (DM), which is an Imagine Optics Mirao 52-e. After the DM, a dichroic beam splitter separates the probe and the imaging light. The probe beam is incident onto a Thorlabs WFS via two lenses ( $f_3 = 400$  mm and  $f_4 = 75$  mm) working in a telecentric arrangement. The pupil of the system is sampled with 97 sub-apertures (as shown in Figure 5.2). The WFS sub-aperture dimension and focal length are respectively 0.15mm and 5mm. A confocal pinhole was placed between  $f_3$  and  $f_4$  to filter the light scattered by tissue located away from the focal plane of the microscope objective. This pinhole is a variable diaphragm whose minimum size is  $850 \mu\text{m}$ . The airy disc diameter at the pinhole plane is  $70 \mu\text{m}$ . The depth of field at the microscope objective focal plane for this pinhole size was equivalent to  $7 \mu\text{m}$  sections, which was small enough to filter the specular reflection on both sides of the 0.17 mm cover slip. The effect of the pinhole size on the transmitted wavefront is discussed in the next section. Finally, the imaging beam transmitted from the dichroic is focused onto the science camera (Q-imaging Retiga 1300) via f5 (200mm).

The HeNe laser probe (633 nm, 1.5 mm in diameter) is injected just before the objective via reflection from a polarisation beam splitter while the depolarised scattered light is transmitted by the beam splitter. The scattered light is collected over the full NA of the microscope objective. As the probe laser is highly coherent, a speckle pattern appears at the WFS camera, which produces errors in the WFS. Here we used a similar technique to the one described in [51], where the speckle was averaged through different focal positions. In our case, we transversally scanned the probe beam at a much higher frequency (120Hz)

than the frame rate of the WFS camera (10Hz), leading to a temporal averaging of the speckle pattern in the wavefront sensor camera plane.

### 5.2.1 Simulation of the effect of the confocal pinhole

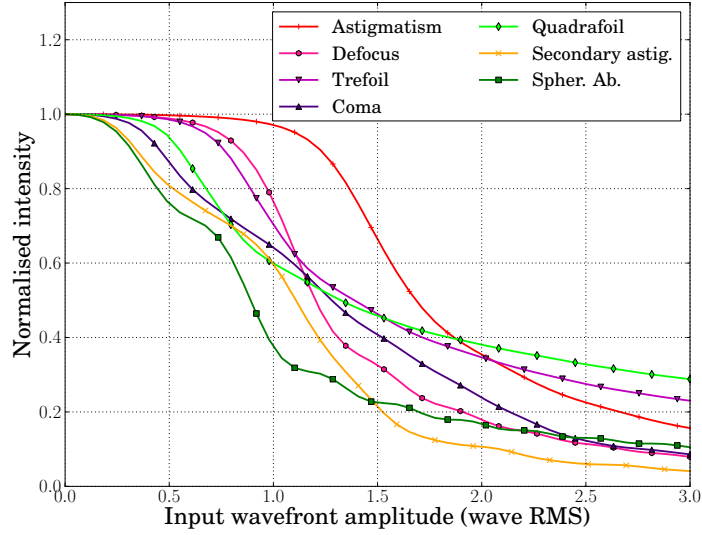
The use of a pinhole at the Fourier plane of a WFS is not new and has been already employed in astronomical AO to:

- Act as a field diaphragm when the object is extended [69]
- Reduce the error in the wavefront correction due to aliasing[70]

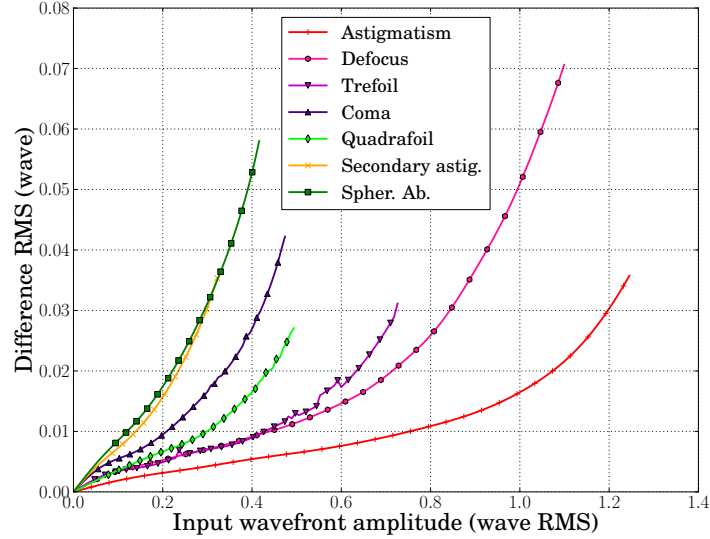
In addition, the pinhole is used here for depth discrimination, which is inherently needed in a microscope. However, the addition of a pinhole acts on both the amplitude and the phase of the transmitted field. On top of a global loss of throughput, it tends to alter the uniformity of the far field and ultimately induces a loss of the phase information carried by the wave. The pinhole behaves as a low pass spatial frequency filter. The evaluation of the pinhole effect on our experiment was assessed by simulation, involving the wave propagation through a 4f system, and a circular mask placed at the focus, for the pinhole. The propagation was made through a simple  $FFT$  and  $FFT^{-1}$  model. In Figure 5.5 the pinhole diameter was kept constant at  $850\text{ }\mu\text{m}$ , as in the experiment, and the input phase amplitude was gradually increased. The far field intensity of the beam and the transmitted phase through the pinhole was then compared to the input ones. In Figure 5.5(a), the total intensity in the exit pupil normalised to the total intensity in the entrance pupil is given for 7 Zernike modes as a function of the input phase amplitude in wave RMS. The transmitted intensity is highly dependent on the type of aberration that is considered. There is a better transmission of low order modes such as Astigmatism for example. In addition to this global throughput variation, the far-field uniformity of the beam is significantly

affected (not shown here). With increasing aberration amplitude, the illumination disparities between different regions in the pupil become critical, ultimately leading to the disappearance of spots in some of the sub-apertures. This effect contributes to loop instability or error in the correction. In Figure 5.5(b), the RMS difference between the transmitted phase and the input phase is plotted as a function of the input phase amplitude. Once propagated through the 4f system and the pinhole using FFT and inverse FFT, the wrapped phase is then unwrapped using the method described in [71]. For large aberration amplitude, the illumination heterogeneity in the pupil is potentially damaging the WFS response. For this reason, an upper limit has been placed on the maximum phase amplitude which is transmitted, and all plots have been terminated when the local intensity in the pupil was under 5% of the intensity computed without aberration. As with the throughput (Figure 5.5(a)), the low order modes are better transmitted than the high order ones. Overall, the phase error is relatively small (less than the diffraction limit) but this effect can not be ignored particularly in an open loop configuration where the system performances are tightly linked to the accuracy in the wavefront measurement.

As a result, for a given pinhole diameter and beam NA, there is a limit in the aberration amplitude which can be transmitted through the pinhole. The pinhole has to be correctly chosen so it acts as a depth discriminator and helps in suppressing the effect of extended objects due to backscattering by the neighbouring area without filtering the other aberrations, which will then be detected by the WFS and corrected by the AO. In our case for a depth discrimination of  $7\mu\text{m}$ , the maximum wavefront amplitude, which can be detected, varies from 0.3 wave RMS for secondary astigmatism up to 1.2 waves RMS for primary astigmatism.



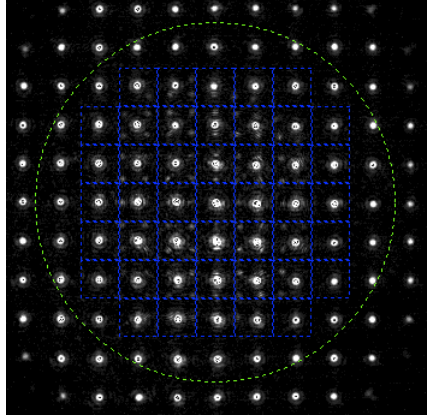
(a) Alteration of the throughput by a 850  $\mu\text{m}$  pinhole. The intensity is normalised to the intensity without any pinhole.



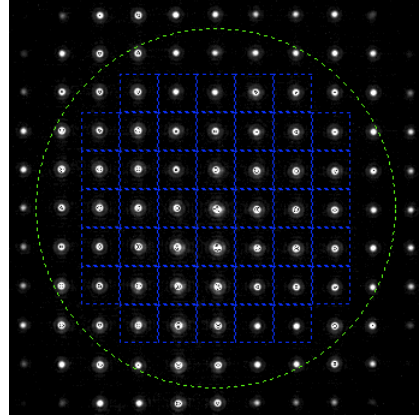
(b) Alteration of the phase by a 850  $\mu\text{m}$  pinhole. The RMS difference is between the transmitted phase through the pinhole and the phase propagated without any pinhole. All plots are terminated when the local peak intensity in the exit pupil is less than 5% of the intensity in the presence of no aberration.

Figure 5.5: Effect on a wave phase and intensity by a 850  $\mu\text{m}$  pinhole

Figures 5.6(a) and 5.6(b) show the WFS spots, as imaged by the WFS camera, when a 2mm (left) and a  $850\mu m$  (right) pinhole is placed at the focus of  $f_3$ . The pinhole clearly improves the quality of the spots, by spatially removing the high frequency details in the spot image.



(a) WFS spots using back scattering light from the sample with a large pinhole



(b) The same spots now with a small pinhole

Figure 5.6: Effect of the confocal pinhole on the WFS spot

### 5.2.2 Improving spot motion measurement using correlation centroiding

The most common WFS algorithm, as discussed in chapter 3, evaluates the centre of mass position of the spot with respect to a reference, and from this distance, calculates the local slope. This method is fast, and works well as long as the spot within the sub-aperture is not aberrated, or remains uniform. However, when the spots are no longer diffraction limited, are images of an extended object or composed of multiple spots, this wavefront sensing algorithm begins to give poor results. WFS algorithm based on "spot" correlation offers an alternative in the case of extended objects. The algorithm consists in the following:



1. If a reference position for each spot is available, then each of the spots, when sensing an aberrated wavefront, is cross-correlated with its spot in the reference position. This is the case in our experiment, as the reference spot positions were obtained after optimising the DM shape using a simplex optimisation with an image sharpness metric.
2. However, if no reference images are available, then each WFS spot is cross-correlated with the spot located at the centre of the aperture.

The position of the cross-correlation maximum in the sub-aperture can be assessed either by computing its centre of mass or by computing the location of a parabolic fit. A threshold function on the spot image has to be applied, so the background does not bias the result<sup>1</sup>. The spot's motion is measured using:

$$\Delta_i = COM \left[ I_i^{ref} \otimes I_i^{ref} \right] - COM \left[ I_i^{ab} \otimes I_i^{ref} \right]. \quad (5.1)$$

$I_i^{ref}$  and  $I_i^{ab}$  are the images of the spot in the  $i^{th}$  sub-aperture, respectively in the reference position and in presence of aberration.  $\otimes$  denotes the cross-correlation operator, and  $COM$  is the centre of mass operator.

In the following, we will be using this correlation method (eq. (5.1)) to estimate the spot position while running the closed loop.

### 5.3 Experiment description

A reference wavefront from a separate source can be used to provide a null reference position for the WFS spots, but this is prone to non-common path errors [17]. Instead we use a wavefront sensorless configuration based on image opti-

---

<sup>1</sup>The correlation of a constant background has a triangular shape with the maximum at the centre of the aperture, then creating a bias on the spot position.

misation, to define the null position and then compared sensed and sensorless operations. The reference position is then obtained by using a simplex optimisation algorithm directly on the sample, with an edge detection maximisation (Sobel Metric) as the metric. A reference wavefront is then recorded from the back scattered HeNe light, to define the reference spot locations on the Shack Hartmann WFS for the closed loop system.

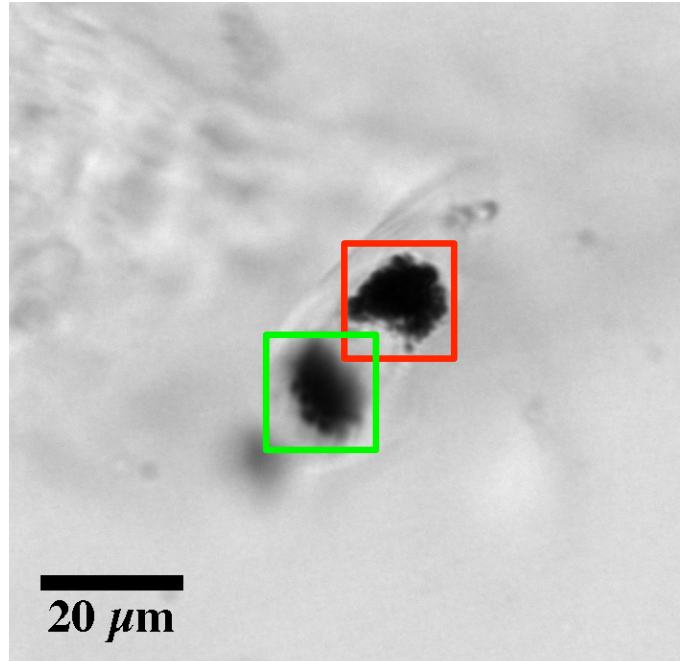


Figure 5.7: Melanin dots in a hair follicle in back mouse tissue, on which the optimisation and closed loop are run. The red square corresponds to sample 1 and the green square is sample 2. The reference wavefront is recorded on the optimised image of the sample 1.

### 5.3.1 Results

With the WFS spots recorded for this optimised configuration the loop is closed with the WFS determining the correction to be placed on the mirror aiming for the recorded optimised wavefront. The stability of the loop is then checked by

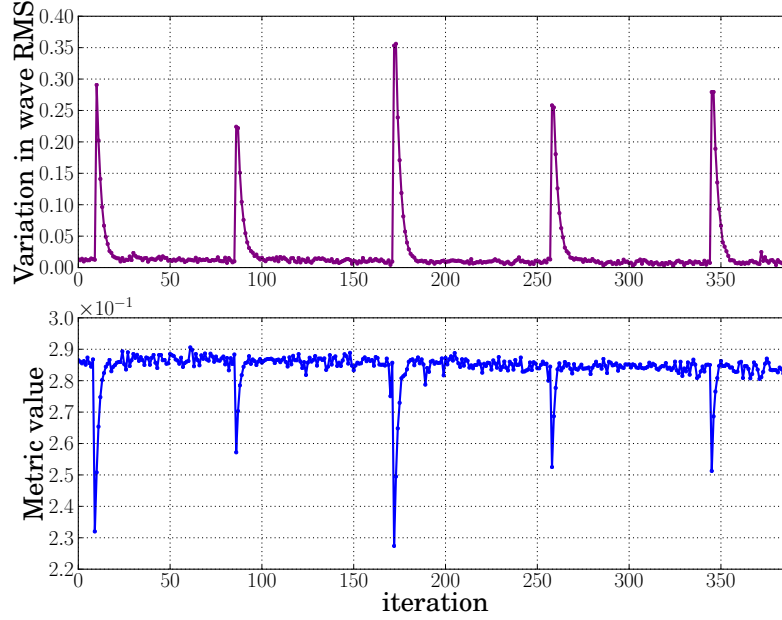


Figure 5.8: Recorded variation on the RMS wavefront (top) and metric value while the closed-loop is on for sample 1, and when 3 perturbations are generated onto the mirror.

sending random aberrations composed of a set of low order Zernike modes to the DM to perturb the system. Defocus is intentionally added to the random aberration. For each step, the RMS wavefront is recorded as well as the metric value. Figure 5.8 - top, shows the variation of the RMS wavefront for 5 perturbations when the closed loop is enabled and the bottom chart shows the metric variation during the loop. For each perturbation, the system restores the minimum wavefront error and the maximum metric value within around 5 iterations. With the stability of the loop confirmed we then open the loop and another melanin spot (sample 2) is placed in the region of interest (green box in Figure 5.7) and the laser probe is focused to the same area. No manual refocusing from sample 1 to 2 was performed, and this correction was left to the AO system. The closed loop is then re-activated on sample 2 but using the

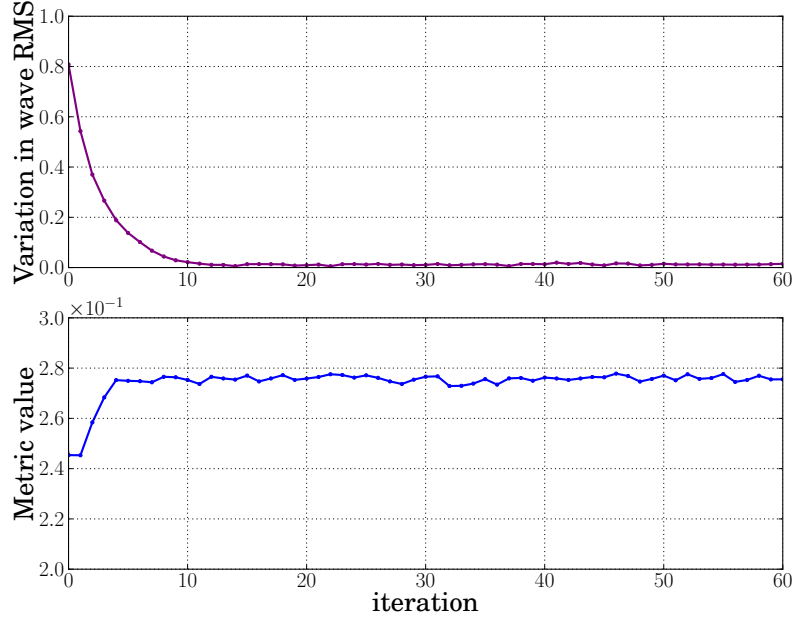


Figure 5.9: RMS wavefront (top) and metric value (bottom) when the closed loop is enabled on sample 2 using the reference wavefront recorded on sample 1.

reference wavefront recorded from sample 1. Figure 5.9 shows the wavefront RMS error (top chart) and the image sharpness value (bottom chart) quickly converging to their optimal values<sup>1</sup>. Thus we demonstrate that we can move, and subsequently observe, any arbitrary part of the object and remove resulting aberrations using the original wavefront measurement as the target for the closed loop.

### 5.3.2 Comparison of sensed and sensorless configuration

In Figure 5.11, optimisations with the closed loop and with the image sharpness metric performed on sample 2 are compared. The closed loop optimisation is

<sup>1</sup>As the melanin spot used for sample 2 is different than the one used for the calibration and the test, the absolute metric value between Figure 5.8 and Figure 5.9 cannot be directly compared.

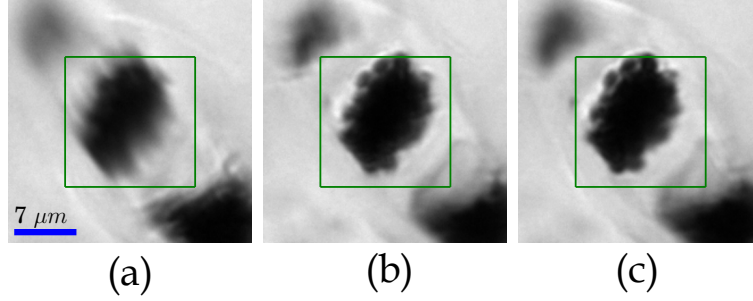


Figure 5.10: Image of sample 2 before optimisation (a), when the closed loop is ON (b) and after a sensorless optimisation (c). The green square delimits the widefield optimisation area during sensorless optimisation.

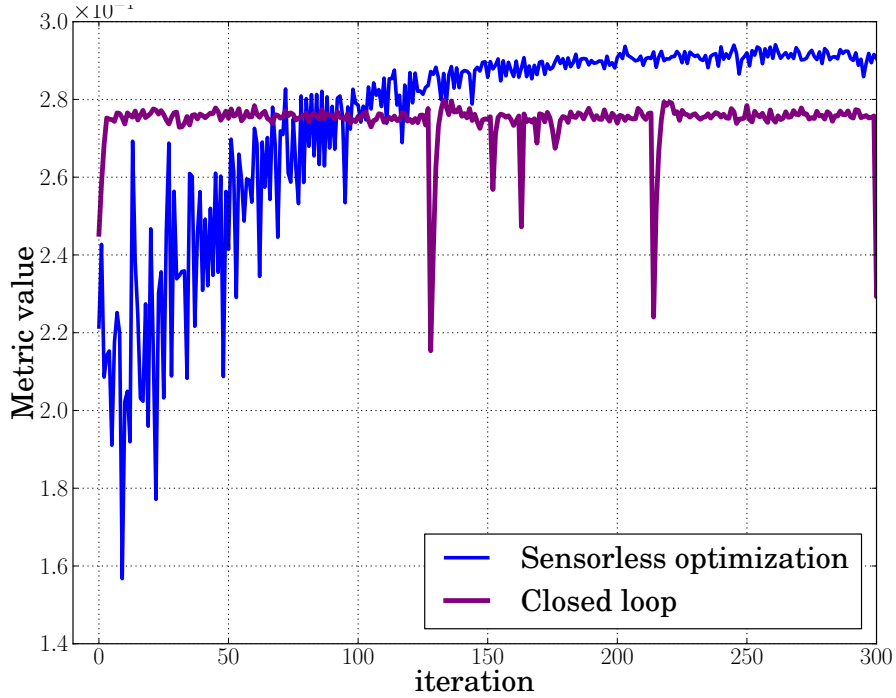


Figure 5.11: Metric value comparison while the system is optimising on sample 2 in a sensorless configuration using the simplex (shown here in blue), and in a sensed configuration (violet). After reaching the plateau, in the closed loop configuration, the stability of the system is checked by sending random aberrations onto the mirror.

very fast, typically reaching the plateau in 5 iterations. The sensorless optimisation does lead to a slightly higher metric value and thus a sharper image but this takes on average 250 iterations. On the closed loop configuration, once the metric has reached the plateau, random aberrations have been sent to the mirror to check the stability. Each time, the closed loop restores the optimal metric value within 5 iterations. Images in Figure 5.10 correspond to sample 2 when the DM is off (a), and using closed loop correction (b) and then a wavefront sensorless optimisation (c). Although, the sensorless and sensed configurations lead to very similar images, the image after optimisation with the sensorless configuration, is slightly better than the one obtained with the closed loop. This result is also confirmed by the image sharpness metric value reaching a higher level in the case of the sensorless optimisation.

The lower metric value is the result of three effects:

- Firstly, the partial sampling of the pupil by the WFS sub-apertures leads to a partial correction of the wavefront distortion. For a given pupil diameter, there are some areas, at the edge of the pupil which are not covered by a sub-aperture.
- Secondly, the sensorless image optimisation is not limited to a specific depth in the sample set by the pinhole but takes into account information also from out of focus regions. The image residual defocus is corrected, leading to higher metric value than for the confocal sensed configuration, where the defocus mode is set by the axial position of the pinhole.
- Thirdly, the contribution of the spot shape in the wavefront reconstruction error. As the 3 dimensional internal structures of the spot are used to create the beacon, the artificial star is generated at the surface of the spot and also at depth. This leads to a beacon with an elongated shape whose

intensity spatial distribution on the WFS camera is a direct representation of the sample variation in density and structure. Due to the high NA of the objective, each sub-aperture in the WFS thus receives a slightly different image of the same object, the artificial guide-star, leading to an error in the wavefront measurement impacting on the ultimate correction of the DM. A similar effect is well known in astronomy using sodium laser guide stars (LGS) [72, 73].

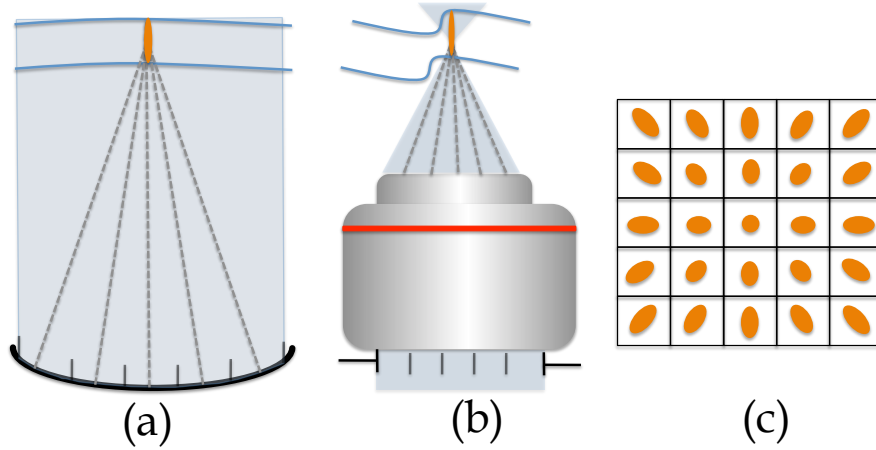


Figure 5.12: Astronomy and microscopy spot elongation effect analogy

On Figure 5.12, the spot elongation analogy with the sodium laser guide star wavefront sensing is shown. In (a), the WFS microlens array are represented onto the telescope pupil. Each sub-aperture is seeing the LGS at a specific angle which increases with the diameter of the telescope. In (b), the effect is similar in a microscope when the beam probe is focused into the sample. The LGS is created with the light backscattered from the sample tissue and each of the sub-apertures (which are uniformly distributed over the microscope pupil) are seeing the LGS with a specific angle leading to the same elongation (as represented in (c)).

### 5.3.3 Conclusion

We have demonstrated the use of partial confocal back scattered light from the sample as a reference source for a WFS in a closed loop AO microscope. We have implemented a simple optical configuration which removes the double path effect as well as the reflection from the slide, and lens surface, which would otherwise confuse the WFS by adding extra sets of spots. The system is demonstrated to operate in a true closed loop manner as we move around the sample with the WFS ensuring an optimal image. The accuracy of the loop is limited by the contribution of the spot shape to the centre of mass measurement and also by the partial covering of the pupil by the sub-apertures leaving the very edge of the pupil uncorrected. The optimisation using image sharpness metric gives slightly better results but takes significantly longer. We thus believe that both true closed loop AO and metric based optimisation have a role to play in AO in microscopy.



## Chapter 6

# Adaptive optics SPIM

### 6.1 Introduction

In this chapter, we describe the use of sensorless AO in a selective plane illumination microscope (SPIM), also known as a light-sheet microscope [74, 75].

SPIM is an attractive imaging modality due to its ability to deliver high-speed, optically sectioned images from within in vivo samples with reduced photo-damage. The sectioning is obtained by the use of a light sheet that selectively excites a slice of the sample at the focal plane of a microscope objective placed perpendicular to the illumination sheet, thus enabling an entire optical section to be recorded in a single camera exposure. The out of focus part of the sample is not illuminated and one can build up a z-stack by only scanning in one (z) dimension. Phototoxicity and bleaching are reduced because the use of a light sheet means that parts of the sample, which are not being imaged at a particular instant, are not illuminated. The principle of SPIM is illustrated on Figure 6.1. The top view represents the SPIM from a point of view placed in the microscope plane, and the bottom view shows the SPIM seen from the top.

The excitation beam is shaped as a light sheet using a cylindrical lens. The line of focus formed by the cylindrical lens is positioned at the back aperture of the illumination microscope, allowing a perfect collimation of the light sheet along the axis perpendicular to the line of focus. On the other axis of the cylindrical lens, with no optical power, the incoming plane wave of the excitation beam is left unchanged and then focused by the illumination objective in the imaging plane. The imaging objective is placed at  $90^\circ$  to the illumination axis, and collects the fluorescence light emitted by the sample.

Zebrafish are interesting biologically because they can be used as a model for human disease [32] and the development of organs such as the heart [76] as well as drug testing [77]. Our interest is in the imaging of the heart, which is further complicated by the fact that it is moving. Previously, 3D reconstruction of a living, beating heart using SPIM has been demonstrated, using real-time optical gating to record images at a consistent phase in the heart cycle [78, 79]. AO has not yet been implemented on SPIM, although alternative techniques such as post-processing deconvolution [80] or structured illumination [81] have been used to improve the contrast and resolution. From the perspective of AO, light sheet microscopy is interesting because the illumination and imaging paths are decoupled and AO can potentially be useful on both paths.

In this chapter we demonstrate a number of points. First we report on AO applied to SPIM and show significant improvement in the imaging quality of a 3D z-stack of a zebrafish embryo using a wavefront modal sensorless AO system on the imaging path. For convenience in the first part of the experiment, we use an *ex-vivo* GFP-labelled transgenic zebrafish embryo. In the second part, we apply our sensorless AO methodology to a live embryo with the aim to specifically correct aberrations in the heart. In this case, we use heart synchronisation techniques to decouple sample motions from image sharpness variations. We

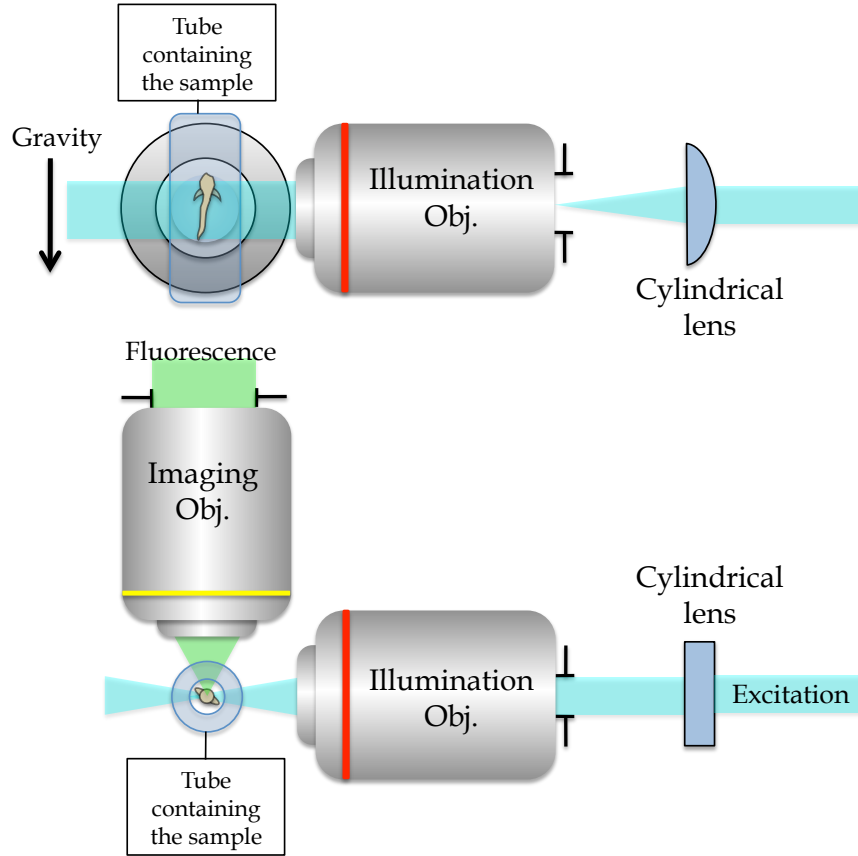


Figure 6.1: The top view represents the SPIM when placed in the plane of the microscope. In this section, the optical power of the cylindrical lens is visible. The focus of the lens is placed in the back aperture of the illumination objective. The bottom view represents the SPIM as seen from the top. The interaction of the light sheet and the sample create fluorescence which is then collected by an imaging microscope.

also show, both experimentally and computationally, that AO on the imaging path can be used to correct beam displacement on the illumination and imaging paths, as well as focus and higher order aberrations on the imaging path. Finally we quantify the aberrations as a function of depth in the sample.

The chapter is constructed as follows:

In section 6.2, we investigate how aberrations occur in a SPIM and how these aberrations vary with the different optical and geometrical parameters. In section 6.3, we describe the optical set-up we used for the AO SPIM. In section 6.4, we discuss the results obtained with fluorescent beads in order to quantify and calibrate the system. In section 6.5, we demonstrate wavefront correction on an *Ex-vivo* zebrafish sample, and show the corrected 3D reconstruction. Finally, in section 6.6, using a heart synchronisation technique presented in [78, 79], we explain how image optimisation on a live, moving heart, can be performed and demonstrate the concept with experimental results.

## 6.2 Source of aberration in a SPIM

The wavefront distortion created by a refractive index mismatch at a planar interface between 2 media of different refractive indices has been analytically modelled and discussed in [21]. This planar geometry, with no azimuthal variations, leads to symmetrical aberrations varying with depth and aperture, is well suited to conventional microscopy where the sample is placed between a slide and a coverslip. The situation is different in SPIM, where cylindrical containers for the sample are commonly used. In SPIM, and more generally in a light sheet microscope, there are two contributions:

1. **On the emission path:** the fluorescence light, emitted by the sample fluorophore, travels through the sample and sample holder. The sample's contribution is not easily predictable since it depends on its shape, size, orientation, and structure. However, if the geometry of the sample holder is well defined, it can be modelled and its contribution to the global wavefront distortion computed with a raytracing software. In the following we will consider a cylindrical glass tube such as the one used later in the experiment, and investigate how the aberration generated on the emission

path may vary with some of the optical or geometrical tube's parameters. The modal decomposition of the aberration created by this glass tube is given on Figure 6.3 for the first 12 modes. The two main aberrations are astigmatism (mode (2, 2)) and defocus (mode (2, 0)). The defocus aberration created by the refraction within the tube is shown on Figure 6.2 in green. The non-deflected rays are shown for comparison in black. The deviation of the rays created by the astigmatism is not shown.

2. **On the illumination path:** the light sheet, normally coplanar to the imaging plane of the microscope, can be deflected by the sample or the tube. As a result, the light sheet is shifted ahead or behind of its ideal location, leading to a perceived defocus aberration on the emission path. This is illustrated, in Figure 6.2, with the blue rays<sup>1</sup>. This effect is, of course, amplified at the edge of the tube.

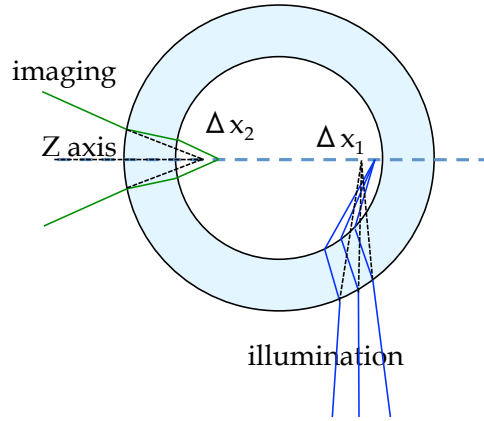


Figure 6.2: Tube geometry used to hold the zebrafish.

The phase aberration function  $\Psi$  can be obtained by calculating the optical path difference (OPD) between a ray passing at the normalised radial coordinate

<sup>1</sup>Normally, on Figure 6.2, the foci of each set of rays coincide but we have drawn them separately here for clarity. The z-axis is shown, which is the scanning axis.

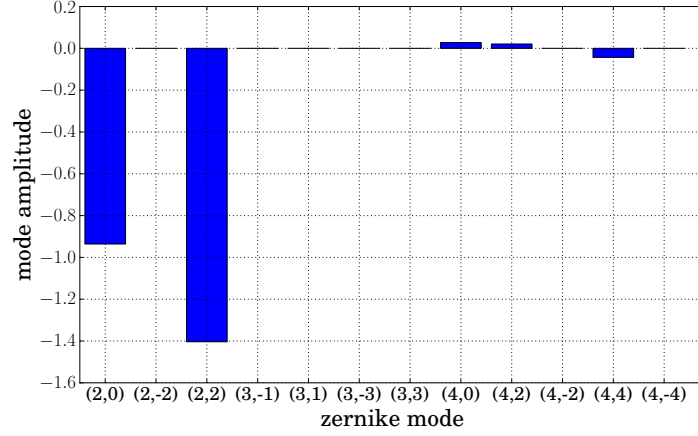


Figure 6.3: Aberration created at the centre of the cylindrical tube expressed as the first 15 coefficients (piston, tip and tilt excluded), for parameters  $\epsilon = 0.25\text{mm}$ ,  $R = 0.5\text{mm}$ ,  $n_1 = 1.3334$ ,  $n_2 = 1.47$ ,  $d = 0.5\text{mm}$  and  $NA = 0.61$ . Defocus (2,0), and astigmatism (2,2) are the main contributors.

$\rho$  in the pupil and the chief ray ( $\rho = 0$ ). The phase aberration is a function of:

- $\epsilon$ , thickness of the pipette - the tube thickness is 0.25mm in the experiment
- $R$  the radius of the inner tube - the inner tube radius is 0.5mm in the experiment
- $n_2$  the refractive index of the tube - the glass refractive index is 1.47 in the experiment
- $NA = n_1 \sin(\Theta)$ , the numerical aperture of the imaging beam - the effective imaging NA is 0.61 in the experiment

$\Psi_{\epsilon,R,n_2,NA}$  is also a function of the focus position  $(y, z)$  within the tube, with  $y$  being the lateral position and  $z$  the depth, the normalised radius<sup>1</sup>  $\rho$ , and the azimuthal angle  $\Phi$  as represented in Figure 6.4.

In the case of the planar interface as describe in [21], the phase aberration is a function only of  $\rho$  and  $z$ . Considering now a cylindrical tube, the phase

<sup>1</sup>If we assume that the objective lens satisfies the sine condition, then  $\rho = \sin\theta/\sin\Theta$ .

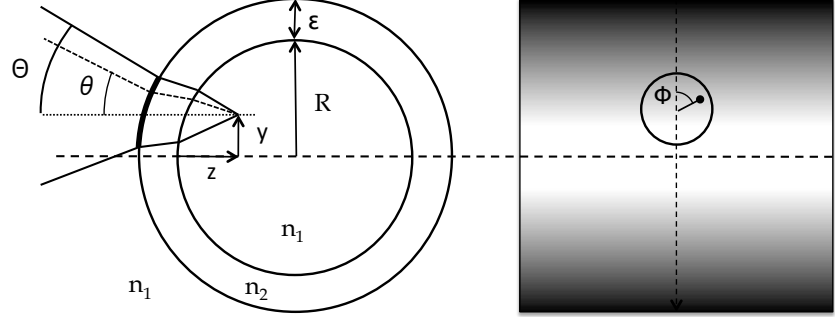


Figure 6.4: Optical and mechanical parameters contributing to the SPIM aberrations. Left view: Cross section of the cylindrical tube. The cone represents the imaging beam. Right view: cylindrical tube seen from the side.

aberration varies, on top of  $\rho$  and  $z$ , also with the azimuthal angle  $\Phi$  and the lateral position  $y$ . The phase aberration can then be expressed as a set of Zernike polynomials,

$$\Psi_{\epsilon, R, n_2, NA}(y, z, \rho, \phi) = \sum_{j=0}^{\infty} a_j(\epsilon, R, n_2, NA, y, z) Z_j(\rho, \phi), \quad (6.1)$$

where  $a_j$  is the amplitude of the  $j^{th}$  Zernike mode  $Z$ . The phase function at the centre of the cylindrical tube ( $y = 0$ ;  $z = R$ ) is decomposed into the first 12 Zernike coefficients (piston, tip and tilt excluded) and plotted in Figure 6.3. An analytical formulation of  $\Psi$  can be obtained by propagating a perfect spherical wavefront through the cylindrical interfaces. This solution yields the most accurate result but on the other hands leads strenuous calculations. Here we used a raytracing software, which computed the wavefront aberration  $\Psi$  by calculating the optical path difference (referenced to the chief ray) for a propagated grid of ray (uniformly distributed at the entrance pupil of the system). The value of each Zernike mode is then obtained by fitting the wavefront aberration with the reference mode.

The eq. (6.1) shows the dependency of the phase aberration with the system's parameters. In the next two sections, we will specifically investigate how the 2 main mode amplitudes, defocus (2,0) and astigmatism (2,2), may vary with:

1. the position  $(y, z)$  within the tube, for fixed system's parameters (same as for the tube used in the experimental part)
2. the system's parameters  $(\epsilon, R, n_2, NA)$ , for a fixed position in the tube ( $y = 0, z = R$ )

All simulations are done at wavelength  $0.55 \mu m$  close to the emission wavelength of the GFP used in our transgenic model.

### 6.2.1 Astigmatism induced by the sample holder

First, the astigmatism variation with the position within the tube is investigated and then subsequently, for a fixed position at the centre of the tube, the astigmatism variations with the system's parameters  $(\epsilon, R, n_2, NA)$  are assessed.

#### Astigmatism variations as a function of the position in the tube

Astigmatism variations are represented in Figure 6.5. Here, the light sheet enters the tube from the bottom, and the fluorescence light is collected on the left of the image. The increasing depth (z axis) is from the left to the right of the figure. Astigmatism increases significantly at the top and the bottom edge where the imaging beam is travelling through highly inclined surfaces.

#### Astigmatism as a function of the system's optical and geometrical parameters

Astigmatism variations with the system's parameters, around their nominal values, are plotted on Figure 6.6 and given at the centre of the tube.



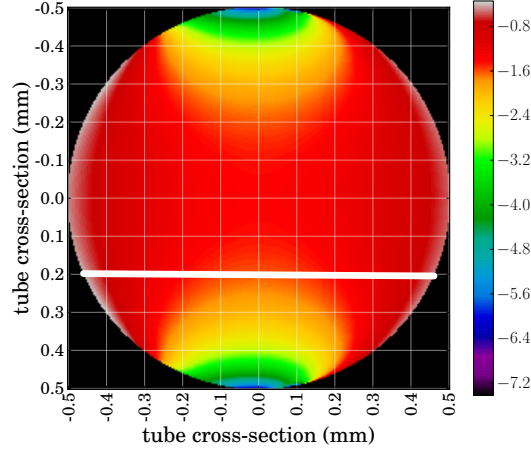


Figure 6.5: Variation of astigmatism in the tube (the horizontal and vertical axes represents the  $z$  and the  $y$  positions respectively as in Figure 6.4) considering that the illumination beam is propagating into the tube from the bottom to the top and the imaging objective is located on the left. The white line represents the location of the Z scan performed in the experimental part with the beads. Simulation obtained with Zemax. The scale bar represents the Zernike coefficient amplitude of mode  $(2, 2)$  in  $\lambda$  RMS.

The level of defocus is independent of the tube inner radius (plot in magenta). While the inner radius is changed, the outer radius is accordingly adjusted so it remains coaxial to the inner wall of the tube. Regarding the thickness of the tube  $\epsilon$  (plot in green), the variation is linear over the investigated range. The Astigmatism is null when the refractive index (plot in blue) of the tube matches the water immersion refractive index. Finally, the astigmatism increases with the NA (plot in brown) following a parabolic variation.

### 6.2.2 Defocus induced by the sample holder

In a light sheet microscope, the defocus is created by the difference in axial position, between the light sheet and the imaging plane of the microscope. As we did previously with astigmatism, we first investigate how the defocus may vary according to the position within the tube (by separating contribution from

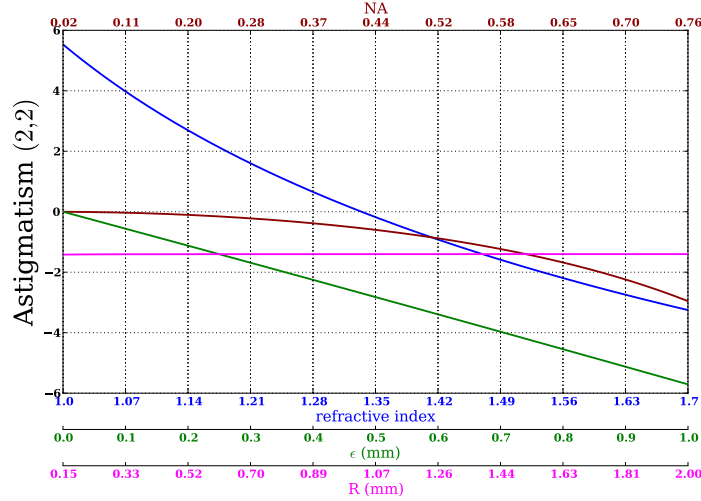


Figure 6.6: Variation of astigmatism with NA (brown), glass tube refractive index (blue), tube thickness (green) and inner radius (magenta).

illumination and imaging paths) and then, for a fixed position at the centre of the tube, we investigate the influence of the system's parameters. The centre of the tube is the only position where the illumination beam is not deflected on either side of the imaging plane by the curvature of the tube. For this reason, only the contribution on the imaging path will be considered.

### Defocus as a function of the position in the tube

Defocus, in Figure 6.7, is the result of a contribution on the imaging path, created by the refraction in the glass tube walls (top left Figure) and a contribution on the illumination path, and perceived as a defocus term on the imaging path (top right Figure). Both contributions are combined by taking the difference<sup>1</sup> and the result is represented on the bottom Figure.

The defocus on the imaging path is obtained the same way as for the astigmatism in the previous section, by computing the optical path difference (ref-

<sup>1</sup>We take the difference because the global defocus is related to the distance between the light sheet position and the imaging plane position

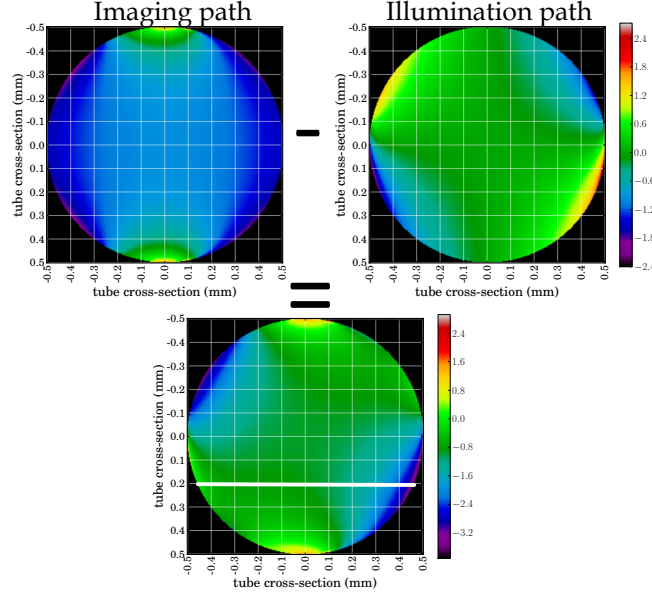


Figure 6.7: Variation of defocus in the tube (the horizontal and vertical axes represent the  $z$  and the  $y$  positions respectively as represented in Figure 6.4). The illumination beam is propagating into the tube from the bottom to the top and the imaging objective is located on the left. The top left image corresponds to the defocus coefficient created on the imaging path only. The top right image represents the defocus as seen on the imaging path but created only by the illumination. The bottom image represents the global contribution. The white line represents the location of the  $Z$  scan performed in the experimental part with the beads. The scale bar represents the Zernike coefficient amplitude of mode  $(2, 0)$  in  $\lambda$  RMS. Simulation obtained with Zemax.

erenced to the chief ray) for a propagated grid of ray uniformly distributed at the entrance pupil. The Zernike modal coefficient is then computed by fitting the wavefront aberration with the reference mode. The defocus on the illumination arm is assessed by first computing the chief ray lateral deviation by the optical system at the illumination objective plan. This deviation is calculated by taking the difference in the chief ray position with and without the cylindrical tube. In this particular case, the deviation is null at the centre and increases significantly at the edge. As the lateral deviation in the illumination plane is equivalent to an axial deviation on the imaging path, and as the axial

deviation is also proportional to the defocus amplitude, the lateral distortion of the light sheet in the illumination plane is then converted to an axial shift on the imaging axis, and subsequently to a defocus aberration. The coefficient of proportionality between the defocus amplitude and the axial position is just a function of the numerical aperture. In our case, for an imaging NA of 0.61, the coefficient is :  $73.2 \lambda \text{ RMS/mm}$ . This coefficient has been obtained with Zemax.

The defocus on the imaging path (top of Figure 6.7) increases at the top and bottom of the tube, as the effective thickness of the glass, as seen by the imaging beam, is also increasing. The induced defocus on the illumination path comes from the distortion of the light sheet due to the cylinder curved surface resulting in an axial shift along the emission path. This perceived defocus is null at the centre of the tube, where the illumination beam is not laterally deviated. However, this effect is maximised at both edges of the tube (left and right of the cross section), where the light sheet beam travels through highly inclined surfaces.

#### **Defocus as a function of the system's optical and geometrical parameters**

The defocus variation with the system's parameters is computed the same way as astigmatism. The result is given in Figure 6.8. Interestingly, the parameters have the same influence on the defocus as on the astigmatism.

### **6.3 Experimental set-up**

The AO SPIM optical diagram is represented in 6.9. A water filled chamber encloses the excitation and emission objectives as well as the sample, held either in a borosilicate glass tube (dimensions given in the previous section) or in a

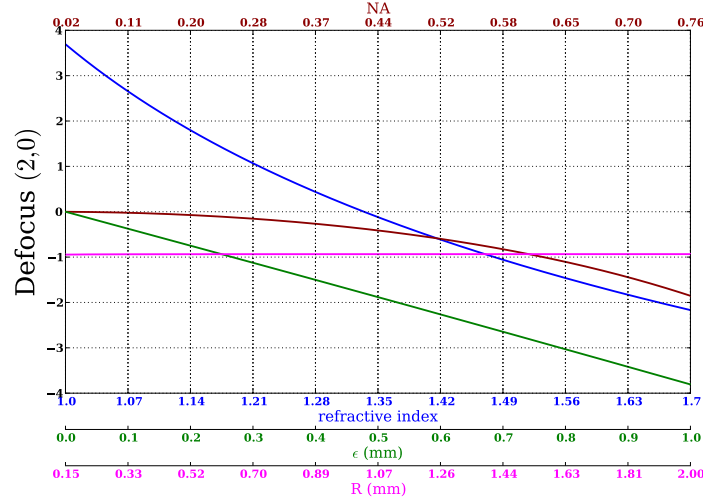


Figure 6.8: Variation of defocus with NA (brown), glass tube refractive index (blue), tube thickness (green) and inner radius (magenta).

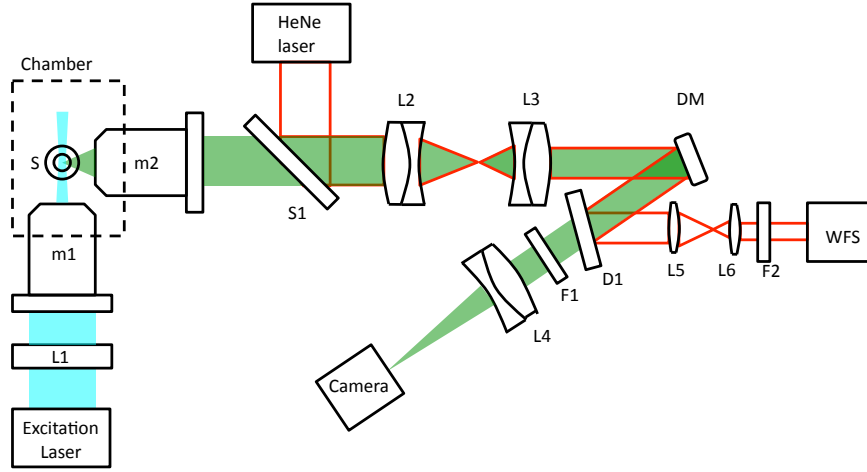


Figure 6.9: Optical Configuration showing the AO SPIM. The illumination light is shown in blue - to the left, and the imaging light is shown in green, to the right. The calibration beam is in red. The symbols are explained in detail in the text.

FEP tube (Adtech Polymer Engineering FI 1.3 x 1.6). The excitation source is a 15mW, 488nm solid state laser. The beam is expanded (not represented) and incident onto a cylindrical lens L1 ( $f = 50$  mm,  $\Phi = 25.4$  mm). A light

sheet is formed at the object plane of a Nikon CFI Plan Fluor 10x 0.3NA. The fluorescence is collected through a Nikon CFI75 LWD 16x 0.80 NA. The beam is then relayed onto a Mirao 52-e deformable mirror (DM) (15mm aperture, 52 magnetic actuators) with the help of 2 achromatic doublets L2 ( $f = 250\text{mm}$ ,  $\Phi = 25.4\text{ mm}$ ) and L3 ( $f = 200\text{mm}$ ,  $\Phi = 25.4\text{ mm}$ ) working in a  $4f$  configuration. An image is formed onto the science camera using L4 ( $f = 250\text{mm}$ ,  $\Phi = 25.4\text{ mm}$ ). F1 is an emission filter. The effective NA of the emission path is 0.61, because the 1-inch diameter beam exiting the microscope objective is vignetted by the 15mm diameter DM aperture. A HeNe laser (633 nm) is used to measure the DM shape. The DM calibration beam is separated from the fluorescence beam by a dichroic D1, and relayed onto a Shack-Hartmann WFS ( $f = 5\text{mm}$ ,  $40 \times 32$  sub-apertures, pitch 150 microns) via a  $4f$  relay composed of L5 ( $f = 400\text{mm}$ ,  $\Phi = 25.4\text{ mm}$ ) and L6 ( $f = 75\text{mm}$ ,  $\Phi = 25.4\text{ mm}$ ). F2 is a 633nm interferential filter.

## 6.4 Aberration measurement using fluorescent beads in a glass pipette

$2\text{ }\mu\text{m}$  fluorescent beads embedded in 0.5% agarose are placed in a borosilicate glass pipette. The sample is scanned in depth at  $20\text{ }\mu\text{m}$  intervals, from the front to the back of the pipette and the images are corrected using the modal wavefront sensorless algorithm and the resulted wavefronts are calculated. Typical before and after images are shown in Figure 6.10.

The before image is recorded with the DM flat, confirmed using the Shack-Hartmann wavefront sensor and HeNe calibration beam. The one-dimensionally elongated spot reveals that the main aberration is astigmatism, created by the cylindrical geometry. The variation in the normalised metric value during the

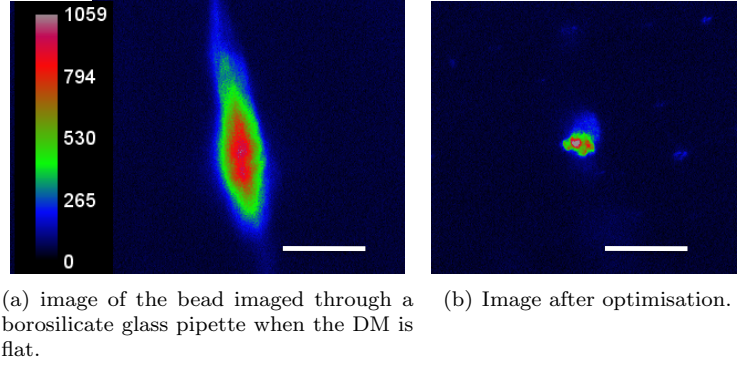


Figure 6.10: Typical optimisation of beads image in a borosilicate tube. The white scale bar represents  $20 \mu m$ .

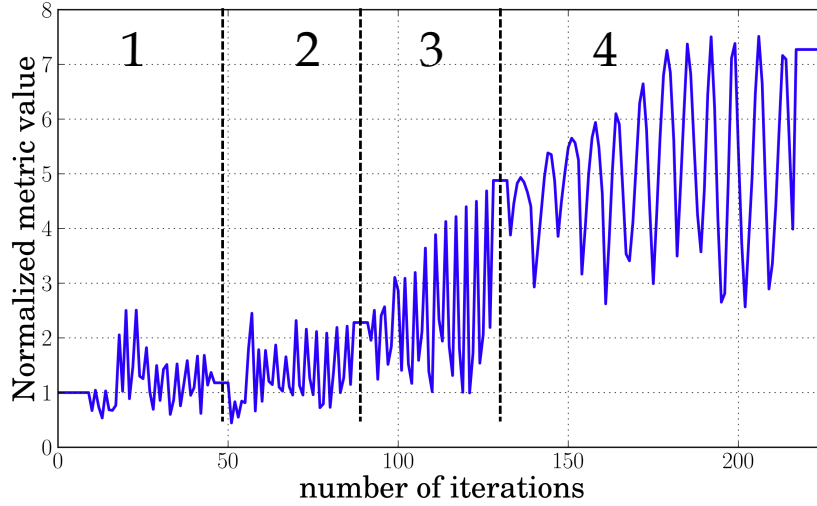


Figure 6.11: Variation of the metric during the 4 optimisation runs (different zones are described in the text).

full optimisation process is shown in Figure 6.11. Four areas have been delimited by vertical dashed lines, each corresponding to a single optimisation run performed on 12 Zernike modes (4-15). For each mode,  $P$  images are recorded, and for each image a specific mode amplitude is produced. In zone 1,  $P = 3$  images per mode were recorded, with Zernike amplitudes varying from -2.5 to 2.5 waves RMS in order to make a coarse estimate of the aberrations. In zone 2

again  $P = 3$  but with a reduced amplitude range (from -0.5 to 0.5 waves RMS) with the starting shape of the mirror being determined by the result calculated from zone 1. Zone 3 is a re-run of zone 2 - but using the starting values from zone 2. Then a final run was performed (zone 4) with  $P = 7$  points per mode and the amplitude varying from -0.25 to +0.25 wave RMS. In zone 1, 2 and 3 the standard deviation metric is used due to its relatively high sensitivity in the presence of a large amount of aberration, as demonstrated in chapter 4. Fourier metric is used in zone 4, where most of the aberrations have already been corrected, for the final optimisation run.

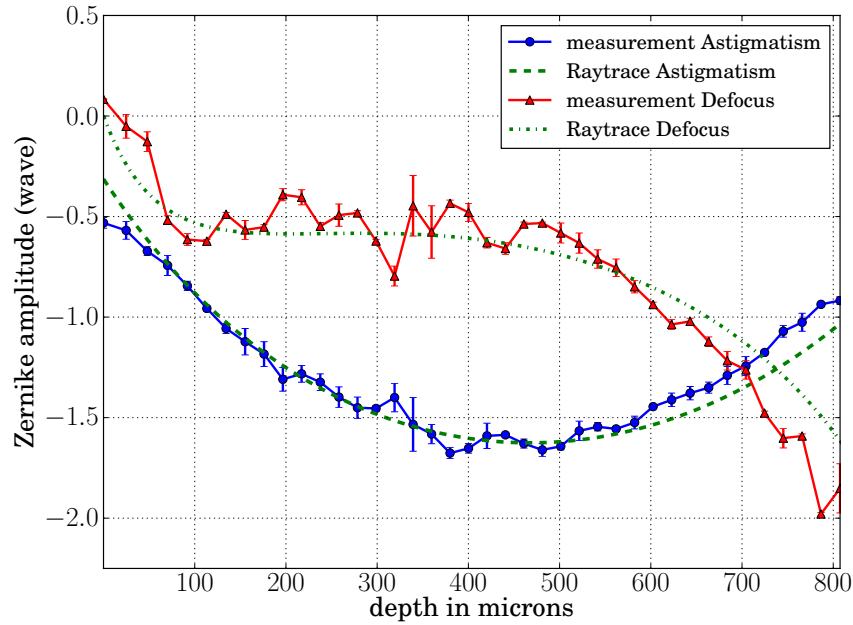


Figure 6.12: Measured and simulated focus and astigmatism variation with depth at a wavelength of 550 nm.

Figure 6.12 compares the simulated (green plots) and measured astigmatism in blue, and defocus in red, with depth. Both simulated green dashed lines are sections located on the white line in Figures 6.5 and 6.7. The 0.2mm decentre



between the tube and the  $z$  translation axis occurred during the measurement. The error bars were calculated during the final run (zone 4), and are here to give a representation of the peak localisation uncertainty. In essence, this uncertainty is here defined as the absolute difference between the measured amplitude giving the highest metric and the amplitude calculated with the fit. This method overestimates the peak localisation error, but supplies an easy way to visualise how far the Lorentzian maximum was from the measurement giving the highest metric. For both astigmatism and defocus, there is a good fit between measurement and simulation. As expected with the glass pipette, astigmatism is the main aberration, reaching a maximum (1.6 waves RMS) at the centre of the cylinder. Regarding defocus, the fit between simulation and measurement confirms that illumination and imaging jointly contribute to defocus, and that the model accurately describes the effect.

## 6.5 Experimental results

### 6.5.1 Aberration correction in zebrafish placed in a glass pipette

The fluorescent beads used for the aberration measurement in the glass tube are replaced by an *ex-vivo* GFP transgenic zebrafish. A  $z$ -stack of images of the pectoral fin is recorded at ten axial positions, uniformly spaced over a depth of  $82\ \mu\text{m}$ . This part of the specimen has brightly labelled features within a fine structure, and has the advantage of being placed on the side of the fish. For each of the ten depths an optimisation is performed and the mirror shape recorded after using the final Fourier metric optimisation. As the features change along the  $z$ -stack, the ROI is accordingly moved such that it remained centred on a portion of the image that contained fine structure. A second  $z$ -stack with finer

axial resolution was then recorded over the same depth range using 100 axial positions in the axial direction. The mirror shape was changed based upon the results of the previous low sampling stack - using the closest optimised image. For each of the 100 points along the stack, in addition to the optimised image (Figure 6.13 (c)), two additional images were recorded using a flat mirror shape (Figure 6.13 (a)), and with system-only aberration correction (Figure 6.13 (b)) (where system refers to the optics and the mounting pipette), corresponding to a mirror shape optimised using beads, when positioned at a depth of  $200\text{ }\mu\text{m}$  from the first surface of the cylinder.

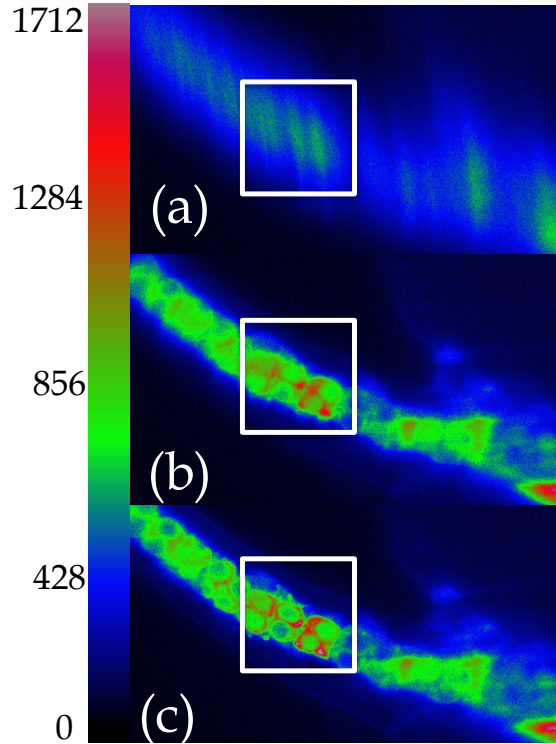


Figure 6.13: AO in SPIM with a zebrafish in a glass borosilicate pipette. (a,b,c) are images taken for a flat mirror shape, a mirror shape optimised for the system aberrations, and for a mirror shape optimised directly on the fish. The white square corresponds to the ROI on which the optimisation is performed and is 24 microns wide.

On Figure 6.14, the three metric values - corresponding to "with AO", "without AO" and "system aberration correction only" - normalised to the "without AO" case are plotted as a function of depth. The green vertical dashed line shows when the mirror shape has been changed. This mirror shape remains the same until the next vertical green dashed line. As the imaging goes deeper into the fish, the ROI on which the optimisation has been performed is moved to a region with more details. The vertical dashed purple line shows when this ROI has been repositioned. There is of course, no relation between all metric values before and after this purple line because different part of the fish are observed. On average over the stack, the metric improves by 380% from the AO "off" image (blue) to the AO "on" image (black).

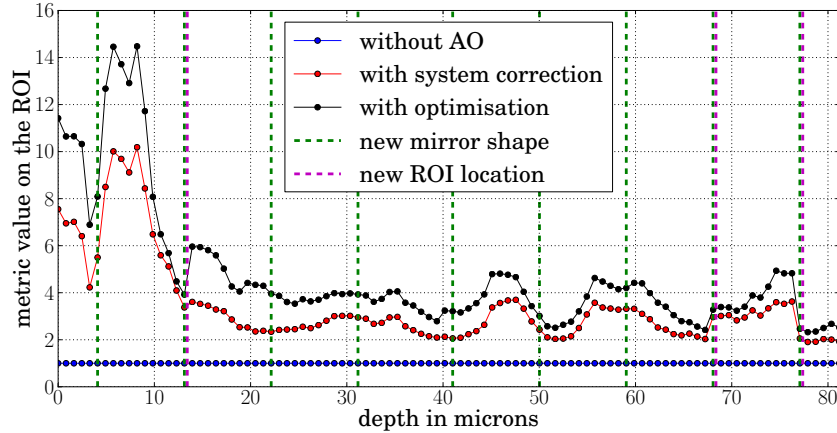


Figure 6.14: Metric normalised to the uncorrected values during the z-stack, as a function of imaging depth, when the mirror is flat (blue), and optimised (black). The green vertical lines correspond to where the mirror has been optimised. The purple vertical line shows when the ROI has been moved.

Figure 6.15 gives the amplitude of the first 12 Zernike modes (Piston, Tip and Tilt excluded) generated on the mirror during the z-stack. Clearly the aberrations do change as a function of depth - but they are also noticeably dominated by system aberrations. The exposure time was between 13 ms and

27 ms per frame depending on the brightness of the feature and to perform an optimisation of 12 modes, with 3 images per modes took about 15 seconds. Our system was not, however, optimised for speed.

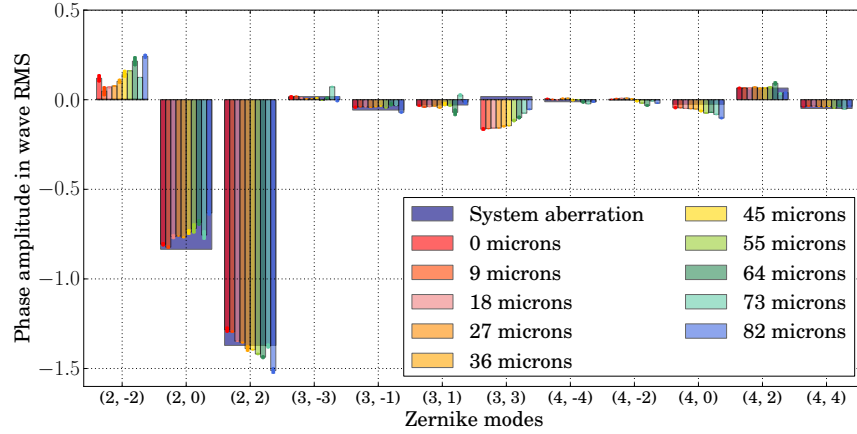


Figure 6.15: Zernike mode amplitude at different depth. Mode (2, 0) and mode (2, 2) are focus and astigmatism, respectively.

### 6.5.2 Aberration correction in zebrafish when placed in an index-matched polymer tube

FEP (fluorinated ethylene propylene) polymer tubing that is refractive index-matched to the water can be used [46] to minimise system aberrations. However, refractive index inhomogeneities in the tube and, in the case of deep imaging, sample induced aberrations still contribute to the image quality and contrast degradation. As with the glass pipette, a calibration was made by optimising using a bead approximately positioned at the centre of the tube (Adtech Polymer Engineering FI 1.3x1.6). Once complete the zebrafish was placed in the polymer tube filled with water and we then followed the same procedure as with the glass tube. First a calibration stack over 80  $\mu m$  composed of ten optimised sections was performed and the mirror shape recorded for each depth. Subsequently,

another stack composed of 100 images was recorded using the optimised mirror shape for a given depth determined from the previous calibration, as before.

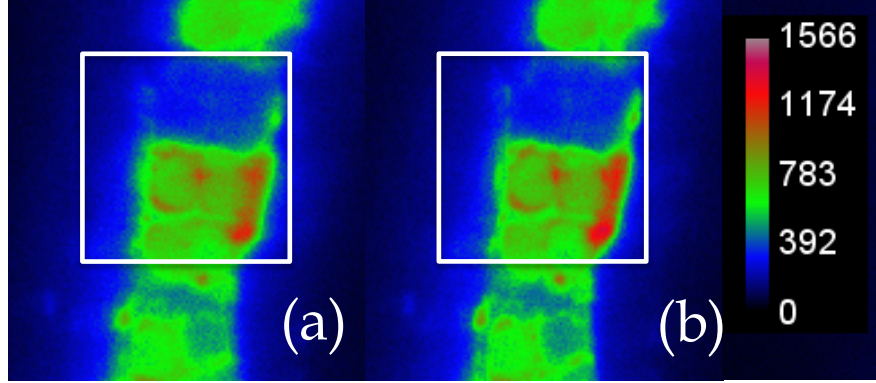


Figure 6.16: Optimisation on zebrafish in a refractive index matching FEP mounting tube. The images show part of the pectoral fin. (a,b) are images taken for a flat mirror shape and for a mirror shape optimised directly on the fish. As discussed in the text - the improvements here are marginal (although clearer in the original data than that shown here). The white square corresponds to the ROI on which the optimisation is performed and is  $19\ \mu\text{m}$  wide.

Figure 6.16 shows images with the AO "off" and "on" respectively. The optimised image presents brighter features. In Figure 6.17, the metric values for the uncorrected, system-only correction, and full correction are shown. The vertical green and purple dashed lines show respectively when the mirror shape has changed, and when the ROI has been displaced. The optimisation leads to higher metric values, except in the range  $[4 - 12\ \mu\text{m}]$  where a saturated localised spot has confused the metric. The error bars represent the standard deviation on the metric value calculated for four images taken at each depth and normalised by the uncorrected case. The error bars are 0.026 on average. The average improvement in metric value is  $10\% \pm 2.6\%$  over the whole stack.

The Zernike mode amplitudes are given in Figure 6.18 for each depth. The contribution of each mode remains small, as compared, for example, with the Maréchal criterion ( $\lambda/14$  RMS), which indicates that the wavefront distortion

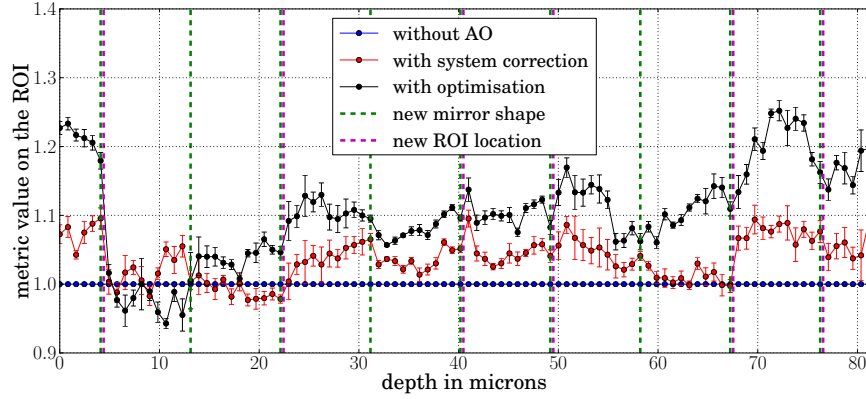


Figure 6.17: metrics normalised to the uncorrected metric (blue) for the case of system only correction (red) and full sample correction (black) . The green vertical lines correspond to where the mirror has been optimised. The purple vertical line shows when the ROI has been moved.

is low. The error on the Lorentzian fit, is, on average 0.013 waves RMS.

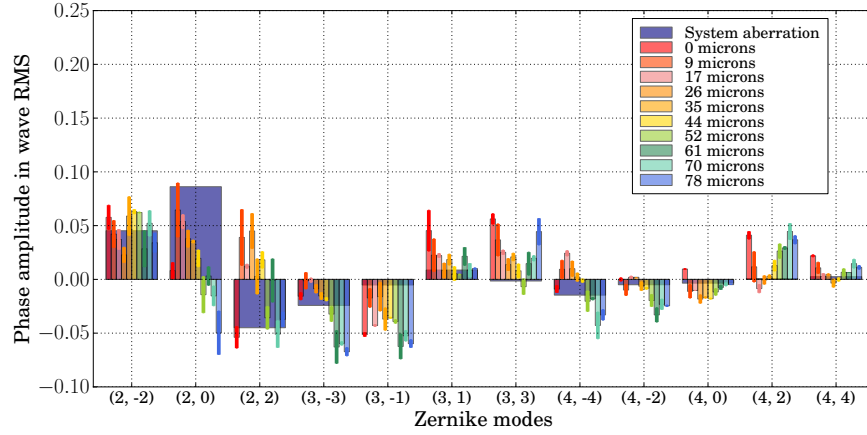


Figure 6.18: Zernike mode amplitude at different depths in the FEP tube.

We calculated the Rayleigh range of the illumination beam to be around  $7 \mu m$  which would give a field of view (defined here as an area over which the illumination beam is at its minimum thickness) of around  $14 \mu m$ . This is clearly smaller than the field of view shown in the results presented in Figures 6.13 and 6.16 and is one of the reasons for the fall off in image quality away from the

centre. In general, the degradation of the imaging performance away from the central point is of great interest in AO - and is also an area, which is relatively unexplored in microscopy. The lateral resolution of the system (in the centre of the field of view) is diffraction limited at  $1\ \mu m$  (given by  $2.44\lambda / (2N.A.)$ ). The axial resolution is harder to measure. In theory, it is governed by the thickness of the illumination sheet, which is around  $2\ \mu m$  assuming there is no broadening of the illumination beam. In practice, when observing the beads we could make an upper bound estimate based on the fact that when we viewed one bead we did not see light contamination from neighbouring beads in the axial direction. The spacing of the beads was typically  $8\ \mu m$  and so we can say the axial resolution is between  $2$  and  $8\ \mu m$ .

In the next section, we will demonstrate the combination of AO with a heart synchronisation system, in order to validate AO correction images within the living heart.

## 6.6 Dynamic correction of aberration in a live zebrafish heart

The heart synchronisation (HS) technique has been described and demonstrated in [78, 79]. The implementation of HS in the SPIM, requires the addition of a high frequency camera and a brightfield illumination, to sample the heart beat at a high temporal resolution so the science camera and laser can be triggered at the precise moment in the heart cycle.

The AO SPIM performances, discussed in the previous section, rely partly on the choice of the image metric. However, we have seen in chapter 4 that the metric, as well as giving a scalar representation of the blur level in the image,

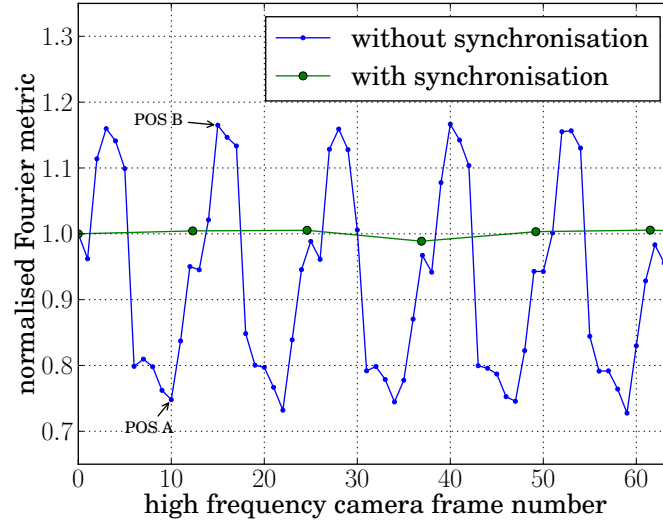
is also sensitive to image content. As a result, when applied to images of a moving heart, changes due to aberrations or due to object structure are indistinguishable based on metric variation only, leading to failure in optimisation. The effect of the beating heart on the Fourier metric is shown in Figure 6.19(a). The normalised Fourier metric is plotted with (green plot) and without (blue plot) synchronisation. Without synchronisation, the metric oscillates at the heart beat frequency, and its variation amplitude covers a range of 40%. The minimum and maximum correspond to the extreme positions of the heart, either left ventricle contracted (Figure 6.19(b)) or expanded (Figure 6.19(c)). With synchronisation activated, the periodic pattern disappears and the metric varies by less than 2%. The 2% residual variation is mainly due to the residual jitter, which comes from variations in the brightfield image, due to the varying flow of blood cells on each frame.

### 6.6.1 Implementation

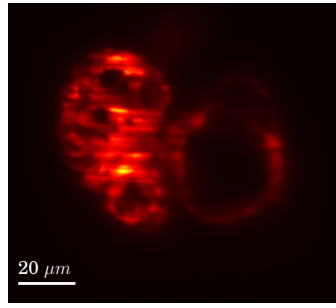
The implementation of HS to the AO SPIM is explained in diagram 6.20. The nominal HS module, as described in [78, 79] is represented in black. A free running monitoring camera (with high frame rate) monitors the heart cycle using a bright field illumination. The PC processes the data and, based on the bright field images, predicts the moment when the heart will be in the correct position within the cycle. Using a FPGA timing controller, a trigger pulse is then sent to the excitation laser and fluorescence-imaging camera. Due to the relatively slow heart period (about 200 ms), the system has enough time within a period to compute the next required mirror shape and apply it to the mirror. By the time the new trigger pulse is emitted, the PC has ensured that the mirror shape has been correctly applied and is stable.

The next section experimentally investigates how a residual motion in the

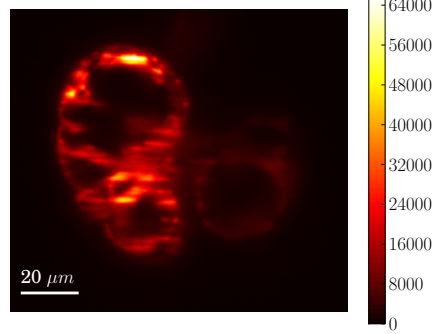




(a) Normalised metric value with or without synchronisation



(b) Position A in the cycle



(c) Position B in the cycle

Figure 6.19: Example of normalised metric variation with or without synchronisation. (b) and (c) shows the 2 heart ventricles in their extreme positions.

image after synchronisation is translated into a wavefront error, through modal optimisation.

### 6.6.2 Metric sensitivity to image variation

The frame to frame residual motion or variation in the synchronised image limits the accuracy of the wavefront correction, particularly when using modal

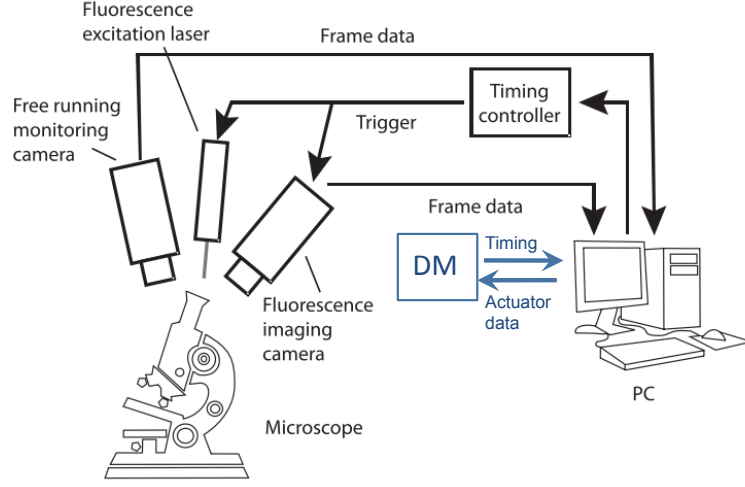


Figure 6.20: Heart synchronisation module in black. The DM is represented in blue, and is running in parallel. The description is given in the text.

optimisation. When an aberration is produced onto the mirror in the form of a mode, at given amplitude during the modal optimisation procedure (described in chapter 3), the metric value is subsequently changed. If at the same time, the images exhibit some small changes due to sample motion or synchronisation jitter, the modal amplitude computed with the function fit will be marred by a significant error. In the following, we estimate this error through measurement and compare how the error varies depending on the choice of the metrics.

	FFT	Stand. Dev. Im.	Intensity Sqrt.	Sobel	Wavelet
STD	0.048	0.084	0.081	0.044	0.061

Table 6.1: Modal amplitude standard deviation measured in Figure 6.21 for the 5 selected metrics.

This error estimation is done with a statistical approach : The position of the metric maximum for a given mode, using a modal optimisation is repeatedly measured (about 35 measurements for each considered mode). For each individual measurement, the mode amplitude is obtained using a modal optimisation based on 3 bias positions  $(-2, 0, +2\lambda \text{ RMS})$  and a Lorentzian fit as

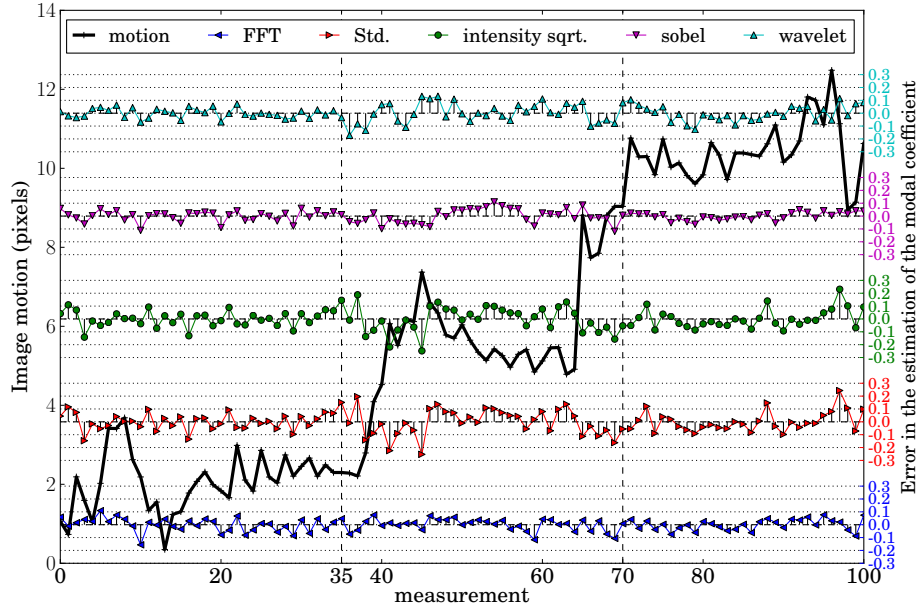


Figure 6.21: Right vertical axis - Variation in the estimation of the defocus and astigmatism modal amplitude over 101 measurements using modal optimisation (based on 3 images). Each point gives the difference between the measurement (defined as being the location of the Lorentian maximum which best fits the 3 samples) and the average of the 101 measurements. The different colours correspond to the different metrics. Left vertical axis - the frame to frame image motion (black solid line plot) is represented.

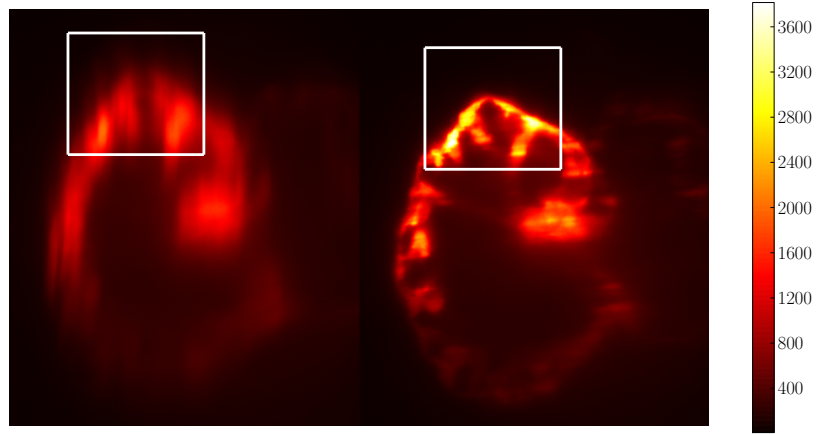
described earlier. On Figure 6.21, the difference between the measured modal amplitude and the average (computed over the whole dataset) is represented at each measurement for the 5 different metrics (which are colour coded - except the black curve which does not represent a metric and is explained later). The dispersion in the measurement gives information about the error in the estimation of the mode amplitude due to the small variation in the synchronised images. The first 35 measurements are evaluating the astigmatism  $(2, -2)$ , the next 35 assess defocus  $(2, 0)$ , and the last 31 measurements estimate astigmatism  $(2, 2)$ . An offset has been added to separate the 5 different metrics. On the right vertical axis, the difference to the average is plotted in wave RMS.

The transversal frame to frame motion is also plotted on the same figure, and appears on the left vertical axis in pixel units. The transversal sample motion is assessed using cross-correlation between the frame corresponding to the modal amplitude 0 (flat mirror shape) and a reference image (Here the first image is used).

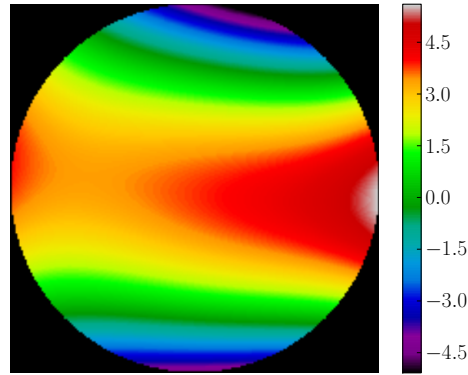
In table 6.1, the standard deviation for each metric is given and compared. The metrics leading to the smallest dispersion (about  $0.05\lambda\text{RMS}$ ), are Sobel and Fourier filters. Intensity squared and standard deviation of the image give the largest dispersion in the measurement.

### 6.6.3 Results

The AO SPIM is now tested with images of a live, beating zebrafish's heart following the same procedure as described in section 6.5. The metric used for the optimisation is the Sobel filter, so the error in the wavefront aberration estimation is minimal. Zebrafish embryos used in this experiment are four days old, expressing green fluorescent protein within their cardiomyocytes  $\text{tg}(\text{myl7:gfp})$ . The embryo is lightly anaesthetised with ethyl 3-aminobenzoate methanesulfonic acid (Tricaine<sup>TM</sup>). In the first part of the experiment, the embryo is placed in a glass tube to confirm that the system is able to correct large aberrations, then the fish is placed in the FEP tube for correction of weaker levels of aberration. Figure 6.22(a) shows the before (left) and after (right) optimisation images obtained when the fish is placed in a glass tube. The modal optimisation is based on the first 12 Lukosz modes. The aberration correction (Figure 6.22(b)) measured on the mirror with the help of the wavefront sensor, is composed of a mix of astigmatism (1.8 wave RMS) and defocus (2.1 wave RMS). The white square represents the ROI on which optimisations have been performed.



(a) Live zebrafish heart section. - Left: Image taken with synchronisation but with AO off. Right: Image with synchronisation and AO on. The horizontal side of the white rectangle is  $64 \mu m$ .

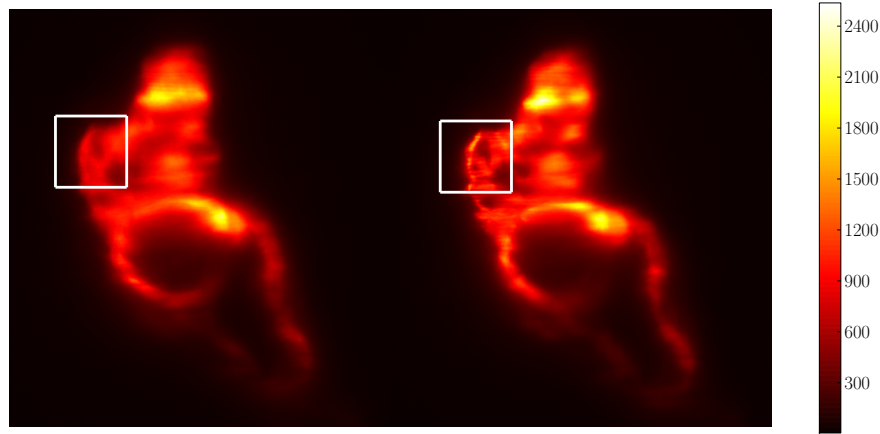


(b) wavefront created by the optimised shape of the mirror

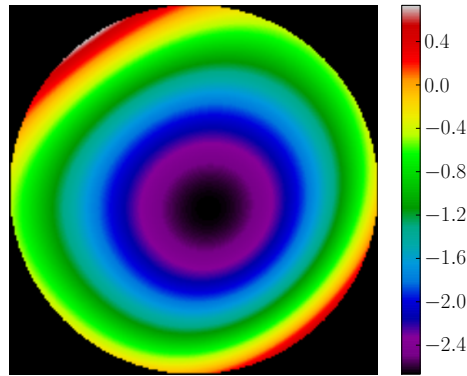
Figure 6.22: Live heart AO optimisation with synchronisation when imaged in a glass tube.

Figure 6.23(a) shows the before (left) and after (right) optimisation images of a live heart section in a FEP tube. The aberration correction (Figure 6.23(b)) is mainly composed of defocus (1.5 wave RMS), which is most likely to be induced by the ovoid shape of the fish heart. The light sheet was first manually adjusted to be coplanar to the image plane of the microscope objective when imaging

the top of the heart, and this adjustment was left unchanged while moving deeper into the heart at a depth of approximately 50 microns when the image on Figure 6.23(a) was obtained.



(a) Live zebrafish heart section. - Left: Image taken with synchronisation but with AO off. Right: Image with synchronisation and AO on. The side of the white square is  $38 \mu m$ .



(b) wavefront created by the optimised shape of the mirror

Figure 6.23: Live heart AO optimisation with synchronisation when imaged in a FEP tube

## 6.7 Conclusion

Aberrations in a cylindrical borosilicate tube have been analysed, and simulated results compared with experimental measurement showing a good fit and confirming the suitability of the model. The aberration, in such geometry, is mainly composed of astigmatism and defocus. We showed that distortion effects of the light sheet contribute to defocus on the imaging path. This effect can be problematic in terms of image quality while doing a z-scan through a sample, because the light sheet position is shifted by varying amounts at different axial positions, hence, introducing a different and unpredictable level of defocus. One solution is to readjust the light sheet position for each depth. However, we have shown how AO can be used, which has the further advantage of correcting aberration on the imaging path as well. We have demonstrated that the correction of aberrations using AO on the emission path of a SPIM microscope enables sharper and more contrasted images. We have demonstrated modal wavefront sensorless AO correction of live, beating zebrafish heart images, using heart synchronisation to decouple sample motion from aberrations. Aberration correction in the living heart has been achieved when the fish was placed in a glass tube, generating high level of system aberration, but also in refractive index matched FEP tube, where sample aberrations dominate. Through the use of heart synchronisation we are thus able to obtain a sequence of images where the underlying features are constant, thereby ensuring that any change in metric value is entirely due to the effects of the changing mirror shape, rather than being contaminated by sample motion. In this way we are able to perform image optimisation in a periodically moving sample where otherwise it would not be possible. We note that the frame to frame residual motion or variation of the image defines a limit to the wavefront measurement and correction based on modal AO optimisation. This becomes problematic, in particular, for the correction of weak aberrations

where the metric's variation caused by the aberration is at the same level as variations caused by changes in the image content. Sobel filter as a metric has been demonstrated, among the selected range of metrics, to lead to the smallest error in wavefront aberration indirect measurement, and this metric should be particularly favoured for image optimisation in a living, moving environment.



## Chapter 7

# Conclusion

This chapter summarises the key results achieved and then discusses possible avenues of further explorations.

### 7.1 Summary

This thesis is concerned with the correction of aberrations in non scanning wide-field microscopes and, in particular, light sheet microscopes for the delivery of high quality images of zebrafish's hearts. All results and discussion presented in this thesis should not be restricted to widefield microscopy techniques, as they also remain valid and relevant for scanning point microscopy. Methods described are mainly based on a wavefront sensorless approach (chapters 4 and 6) but also encompass a complete sensed configuration based on a novel approach using the backscattered light from a sample as an artificial guide star.

In chapter 4, 5 different metrics have been numerically and experimentally compared, with a view to better understanding the process behind image optimisation. We find that, despite the fact that all metrics have their maximum sensitivities for PSF blur level around 1 to 1.5 pixels RMS, they all exhibit

different characteristics. Depending on the level of aberration, the complexity of the object, and the noise level, some metrics are more suitable than others. On the other hand, we experimentally saw that for simple low order aberration and object structure, the choice of the metric is not so important. The reason is that, due to the simple shape of the metric function in the variable space, all routes chosen by the algorithm lead to the same solution.

In chapter 5, we demonstrate that backscattered light from the sample can be used to provide the feed-back of a wavefront sensor thus enabling real time aberration correction. The improvement in imaging performance is compared to a sensorless adaptive optics system controlled via an image optimisation routine. The samples are imaged without fluorescence to ensure that photobleaching and other potential variations did not affect the comparisons in system performance, though the method is equally applicable for fluorescence microscopy. Optimisation using an image sharpness metric gives slightly sharper images but takes significantly longer. In this experiment, a first novel approach is to use an independent laser probe which can be positioned anywhere in the field of view (FOV) (assuming the observed region of the sample presents enough backscattered light), allowing optimisation using a common reference wavefront, with the accuracy of the loop being limited by variation across the sub-aperture images induced by the elongation of the guide star. A second key method is to use image optimisation to define the null position for the wavefront sensor, leading to a system calibration in situ without the need to remove the sample.

Finally in chapter 6, we report on the first implementation of AO on the emission path of a SPIM microscope. We show how aberrations occur from the sample mounting tube and quantify these aberrations both experimentally and computationally. A wavefront sensorless approach is taken to imaging a green fluorescent protein (GFP) labelled transgenic zebrafish. We obtain improvement in

image quality whilst recording a 3D z-stack and show how the aberrations come from varying depths in the fish. We demonstrate wavefront sensorless modal AO correction applied to a live, beating zebrafish heart, using heart synchronisation to decouple sample motion from aberrations in the metric variations. We measure the impact on the wavefront correction of the image residual motion and show in what proportion the metric influences the wavefront accuracy.

## 7.2 Future work

In light of the results presented in this thesis and given the many possibilities offered by the SPIM design we suggest a number of ideas that may be interesting investigating in future work.

### 7.2.1 Implementation of AO on the illumination path of a SPIM

We have seen in this thesis, the advantage of using AO on the imaging path of a SPIM. There are also numerous benefits in using AO on the illumination path, because AO may control the light sheet thickness by removing some unwanted aberrations, and could also control the position of the narrowest part of the light sheet over selected areas of a large sample.

#### Optimisation of the light sheet thickness - High NA illumination

The type of aberration created along the illumination path has various effects on the light sheet and the overall image quality:

- defocus in the aberration induces a shift of the light sheet waist along the illumination axis - The shift can be detrimental for example while doing

a z-stack, when the narrowest part of the sheet is moved away from the desired region inducing a loss of axial resolution.

- tilt of the light sheet out of the imaging plane induces a varying level of defocus for each lateral position in the field of view
- and finally, higher order aberrations along the illumination path create a broadening of the light sheet, which leads to a degradation of the axial resolution

The effect of these aberrations is worsened when a high numerical aperture objective is used on the illumination. The high numerical aperture inherently leads to a shorter section thickness but also depth of focus (or Rayleigh range) limiting the high axial resolution over a limited FOV. The accurate position of the waist both along the illumination and imaging axis has then a crucial importance. Each can be controlled with a suitable adjustment on the illumination arm. The control of the position of the beam waist along the illumination optical axis can be achieved with the help of a DM which has the additional advantage of also enabling a correction of higher order aberrations.

We suggest the use of a large stroke DM placed on the excitation path to produce an artificial defocus and enable the adjustment of the position of the narrow part of the light sheet anywhere in the FOV. An interesting configuration would be to synchronise the rolling shutter of the Scientific CMOS with the DM (gradually applying a defocus) so only the narrowest part of the light sheet is imaged onto the detector and the other part is confocally rejected on one axis. The Figure 7.1 describes the concept.

In [82], Baumgart et al use the rolling shutter of a scientific CMOS synchronised with the scanned line of a light sheet microscope, and demonstrate the production of enhanced images with better resolution and contrast by reducing the background light caused by scattering. Here, we propose an alternative solution

where the light sheet is produced this time by a cylindrical lens, and where the rolling shutter of the SCMOS is aligned and parallel to the narrowest part of the light sheet. By changing the focus (with the DM) on the illumination path, the waist of the light sheet is scanned along the FOV and synchronised with the rolling shutter producing an image of a thin section on an extended FOV. The concept is explained in Figure 7.1.

As the beam is gradually scanned, the narrowest part of the light sheet enters deeper into the sample. The illumination beam may also be subjected to aberration, and these aberrations may change with a varying amount as the light sheet is axially scanned. Thus, on top of the defocus mode produced by the DM, an additional correction may be required when imaging deeper part of the sample (region on the right of the sample on Figure 7.1).

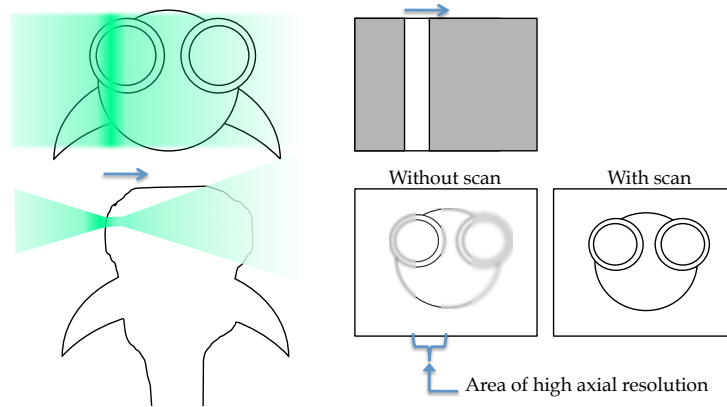


Figure 7.1: Top left view : The light sheet is in the plane of the drawing and is scanned from left to right. The sample is observed from the imaging direction - Top right view : The rolling shutter is synchronised with the scan of defocus applied to the light sheet so the narrowest part of the sheet is imaged onto the camera and the other part rejected. Bottom left view : section of the light sheet, showing the position of the beam waist. - Bottom right view : image on the camera of the fish section observed without (left) and with (right) scanning of the light sheet along the excitation axis.

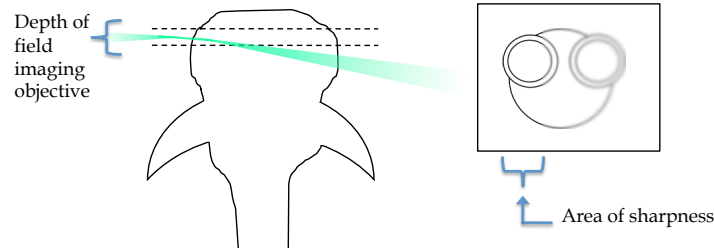
### **Optimisation of the light sheet position - low NA illumination**

When a low NA illumination is used, the light sheet becomes relatively broad (a few microns) and the main source of image degradation on the illumination comes from the light sheet being deviated by surfaces on the path rather than the broadening caused by aberrations. By the time the excitation sheet reaches the region of observation, it has been moved out of the imaging plane by sample surfaces, creating a perceived defocus aberration as discussed in chapter chapter 6. Figure 7.2(a) illustrates the problem and Figure 7.2(b) suggests a solution to remove the light sheet tilt.

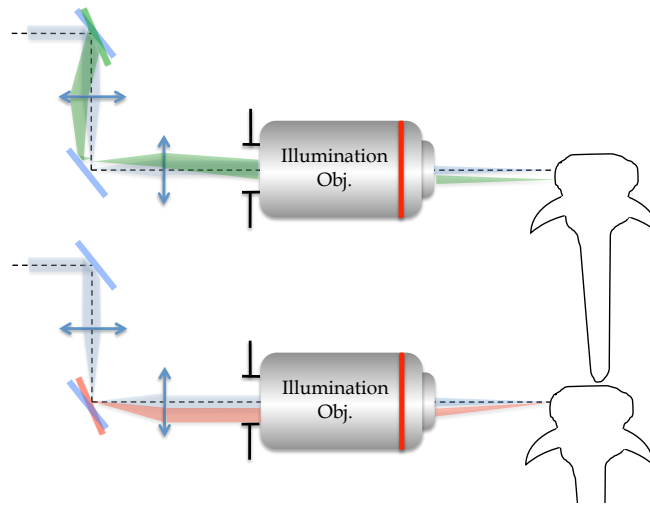
We propose a solution combining 2 tilt mirrors to give a total control of the light sheet tilt and "depth" position. One is placed in the imaging plane and the other in the pupil plane. This solution implies the use of a high NA illumination microscope working with a limited diameter input beam, so the difference between the working NA and the available one is used to compensate for the tilt of the light sheet produced by the surface within the sample. As the tilt of the light sheet is produced at an arbitrary point along the propagation direction (which is more likely to occur at the entrance of the sample), depending on where the light sheet is straightened up, there might be a residual shift between the corrected light sheet position and the imaging plane. The mirror conjugated to the imaging plane (in a 2f configuration) is then used to translate the light sheet along the optical axis of the imaging objective.

### **7.2.2 the combined use of structured illumination with AO**

Although AO has great potential to correct aberrations, it does not correct effects of scattering which occur along both illumination and imaging paths. The suggested solution using the rolling shutter described earlier, filters part



(a) Aberrations in a light sheet microscope due to deviation of the light sheet - Left view : the light sheet entering the sample from the left is deviated by a surface creating an angle between the light sheet and the imaging plane. - Right view : effect of the tilt perceived on the image, the image is seen sharp on the left and the blur is increasing to the right.



(b) Solution for the correction of the light sheet tilt and position - Top view : A mirror with a controlled tilted is placed in the conjugate plane to the back aperture for axial adjustment of the light sheet position along the imaging axis. - Bottom view : Another mirror with a controlled tilt is placed in the conjugate plane to the sample, for adjustment of the light sheet tilt.

Figure 7.2: Tilt correction of the illumination - the beam is represented in the axis of the cylindrical lens with no optical power.

of the scattering light by rejecting the out of focus light only along one axis and it does not suppress it totally. Solutions employing structured illumination [83] on the light sheet have been successfully employed on a line scanned light sheet illumination microscope, but not yet on a design using a cylindrical lens.

Designs with a cylindrical lens offers many advantages. These are :

- faster, because all pixels of the camera are exposed at the same time.
- simpler in their implementations, because a scanning system requires additional and expensive optics

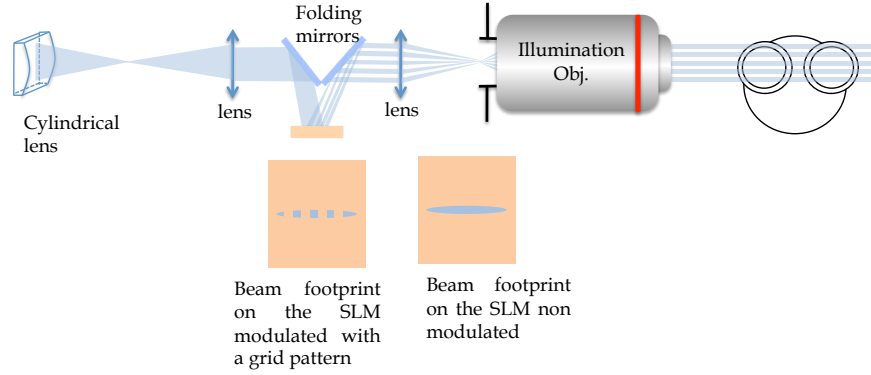


Figure 7.3: Implementation of HiLo background rejection on a non-scanning light sheet microscope. The cylindrical lens produces a line which is relayed onto the back aperture of the illumination microscope via a 4f relay. At the focal distance of each lens, a reflective SLM is placed and used in amplitude modulation only.

A configuration using a cylindrical lens and structured illumination (HiLo background rejection) is suggested in Figure 7.3. The line of focus created at the focus of the cylindrical lens is relayed onto the back aperture of the illumination objective. The grid pattern in the light sheet is produced by a SLM placed between the two relay lenses, at the focal distance. Two alternative signals are sequentially applied to the SLM : One with a grid pattern and one with no modulation. The background is removed by post-processing on the 2 acquired images as described in [83].

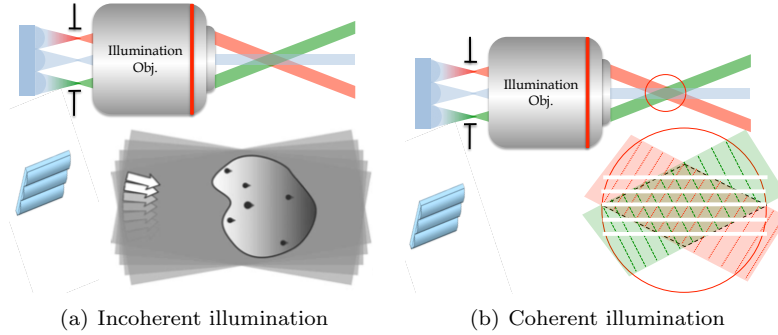
The combined use of structure illumination with the light sheet and AO on the imaging arm is an alternative field of investigation. Where HiLo offers a way of optimising the axial resolution, AO optimises the lateral resolution.



### 7.2.3 Shadow reduction with a static optical device

Solutions to mitigate the shadows which occur when the light sheet encounters a localised absorbent or scattered region within the sample have been proposed quickly after the first SPIM design was released, and these solutions generally imply a scanning device such as the galvanometer mirror. In [84], the light sheet created by a cylindrical lens is scanned in its own plane around the centre of the FOV. As the light sheet is scanned at a much higher frequency than the exposure time, the shadow artefacts are averaged on a range of angle resulting in a significant reduction of the shadow contrast. In [85], Fahrbach *et al.* use the self-reconstruction properties of Bessel beams on a line scanned light sheet design to also significantly reduce the effect of the shadows.

We suggest here the use of a cylindrical micro lens array to obtain a similar averaging effect. The concept is explained in Figure 7.4(a) and implies the use of a low coherence source with a view to keep a uniform (as opposed to structured) illumination in the light sheet plane. In Figure 7.4(b), the resulting horizontal fringe pattern created by two incident beams is shown in the case of a coherent source. As most of the excitation sources in light sheet microscopy are lasers and therefore highly coherent sources, a solution to reduce the contrast of the fringes would consist in rotating the polarisation on each line of micro lenses.



With only 2 lines of cylindrical micro lenses, a perfectly uniform beam can be achieved with 2 orthogonally polarised beams. For more than 2 beams, the reduction of the shadow becomes more obvious as more angles are averaged together, but interference fringes may also occur, spatially modulating the light sheet.

#### 7.2.4 A reversible SPIM

Multiview reconstruction [74] can be obtained by rotating the sample around a vertical axis and acquiring images from a single or two opposite imaging objectives [86]. We suggest here a simple configuration which consists in using two identical imaging objectives (with a large NA) as an imaging and illumination objective as represented in Figure 7.4. The fluorescence is separated from the excitation beam by a dichroic mirror (DM). The cylindrical lens (CL) is placed before the DM, so it does not affect the fluorescence imaging beam. The excitation beam diameter is adjusted separately, to obtain the desired light sheet thickness. The advantage of this configuration is that both paths can be used at the same time, generating a non sequential multiview without the need of additional optics. The fact that no rotation is needed to have 2 orthographic views makes this design very attractive for fast sample imaging (Live heart imaging for example).

#### 7.2.5 The use of the light sheet to create a localised artificial guide star for direct wavefront sensing

Another direction, which requires investigation, is the option offered by direct wavefront sensing in a light sheet microscope. The idea is to use the light sheet to create a localised spot or illuminated region in the ROI, which can be subsequently employed as an artificial guide star. As previously discussed, the fact that the light sheet is decoupled from the imaging path is an advantage

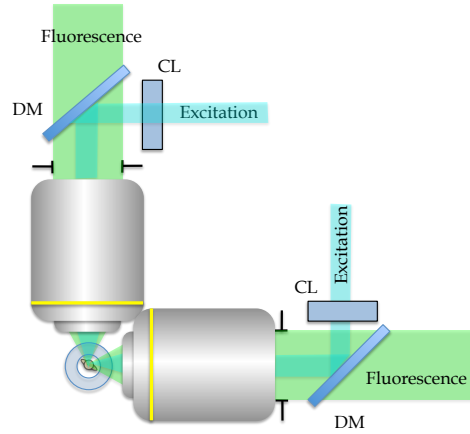


Figure 7.4: concept of a reversible SPIM - DM refers to Dichroic mirror, and CL refers to cylindrical lens. The two identical objectives allows the visualisation of the sample along two orthogonal views and can also simultaneously produce a light sheet with the help of an illumination system placed behind the CL.

and can be easily added to the illumination arm. The principle is explained in Figure 7.5. Direct wavefront sensing will afford real time 3D correction of the

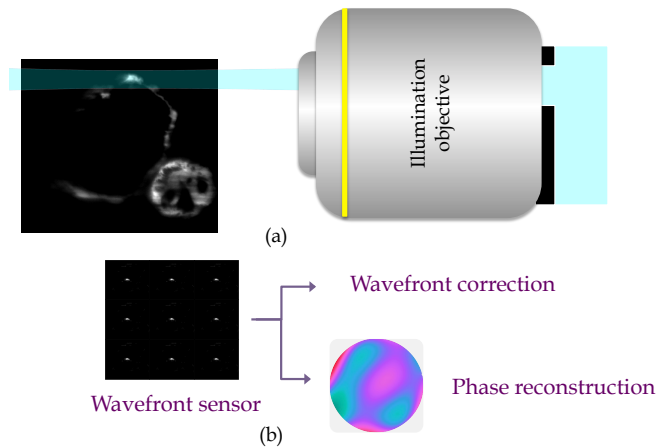


Figure 7.5: (a) A portion of the light sheet is used to illuminate an isolated feature in the heart section, creating an artificial guide star. (b) The feature is used by the wavefront sensor for feedback of the DM.

aberration. In the particular case of the live beating heart imaging, even 4D

correction can ultimately be achieved by correcting the aberration at a specific depth and time in the heart cycle, as the aberration may periodically change with the heart beat phase.

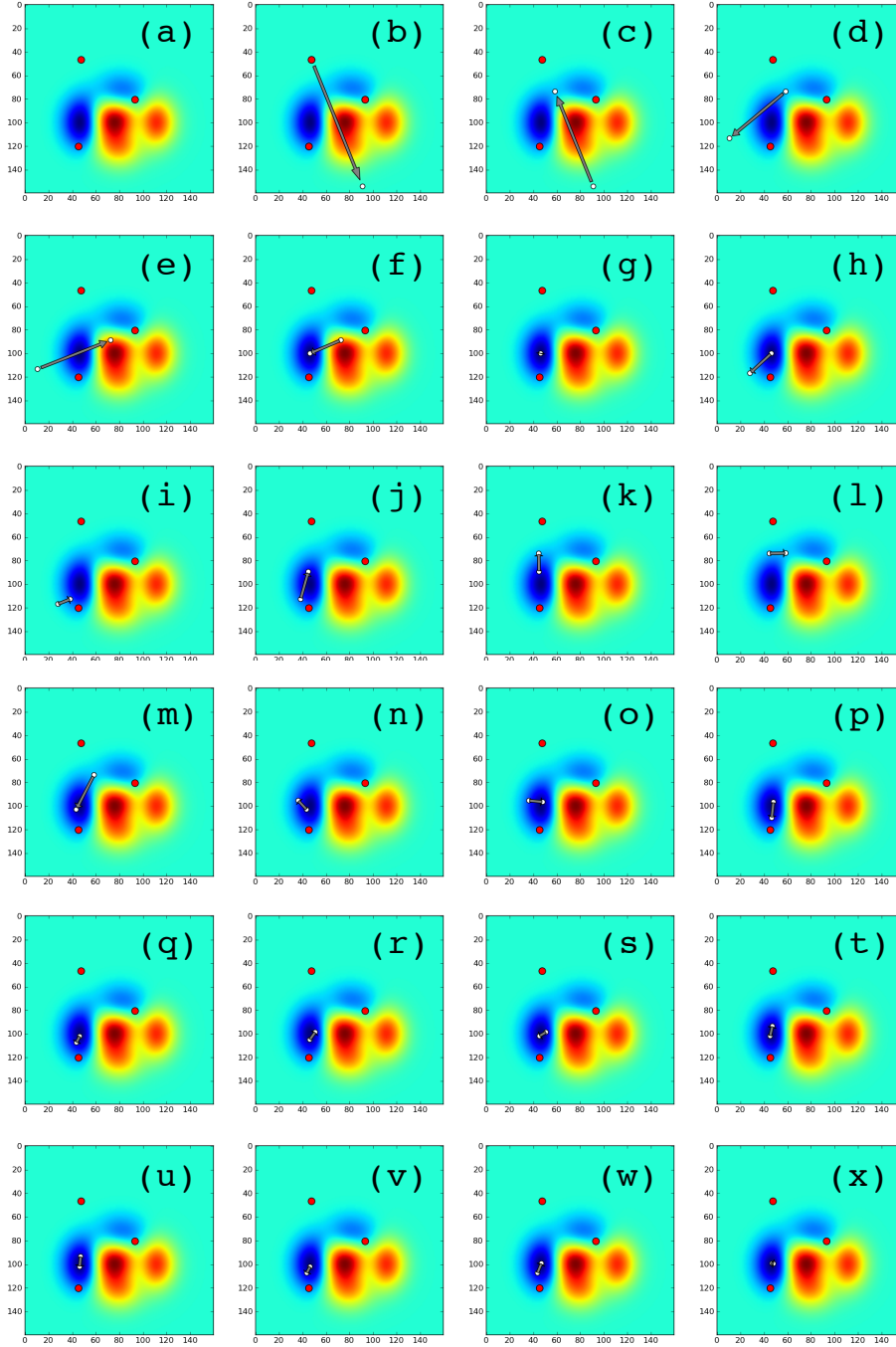
# Appendices

## Annexe A

# Step by step simplex optimisation in a 2D configuration

This annex details a simplex optimisation step by step in a 2 dimensional space. The minimum to be found is the blue dip on the left of the image. In (a), the 3 red points are the starting positions which have been randomly determined. There are 3 starting points as the example is given in a 2D space. The simplex always requires  $N + 1$  starting positions with  $N$  being the dimension. To be efficient, the initial guesses have to encompass a large area which preferably (but not necessarily) includes the minimum. In (b), the worst point (the one exhibiting the highest value among the starting points - top red point) among the initial guesses is removed, and a mirrored point is then included in the dataset. Its position is calculated by taking the symmetric of the worst point with respect to the centre of mass of the 2 other points. The arrow defines the

direction of motion from the worst point to a newly computed position. As the mirrored point in (b) is not better than the  $2^{nd}$  worst point (it even has a higher value than the previous point), a contraction from the initial worst point in (a) is done in (c). The position of the new point is then calculated by taking half of the distance between the worst point in A and the centre of mass of the 2 others. Another iteration is called with a new set of initial guesses, which are two of the initial starting position (red) and the new contracted point. The worst point becomes the red initial starting point on the right. In (d), a mirrored point is computed with the worst point among the 3 positions. In (e), as the mirrored point is not better than the  $2^{nd}$  worst, then a contraction is done around the best point, which is the initial bottom red starting point. from (g) to the (x), the algorithm proceeds to the following transformation: mirror, expansion, and contraction until the tolerance or the specified number of iteration is satisfied.





# Bibliography

- [1] C. Huygens. *Traité de la Lumière*. Leyden, 1690.
- [2] M. Born and E. Wolf. *Principles of Optics*. Pergamon, 1980.
- [3] J. W. Goodman. *Introduction to Fourier Optics*. McGraw-Hill, 1968.
- [4] B. Richards and E. Wolf. Electromagnetic Diffraction in Optical Systems. II. Structure of the Image Field in an Aplanatic System. *Proc. R. Soc. Lond. A*, 253(1274):358–379, 1959.
- [5] B. W. Smith, D. G. Flagello, J. R. Summa, and L. F. Fuller. Comparison of scalar and vector diffraction modeling for deep-uv lithography. *Proc. SPIE*, 1927:847–857, 1993.
- [6] R. J. Noll. Zernike polynomials and atmospheric turbulence. *J. Opt. Soc. Am*, 24(1):139–55, 1976.
- [7] W. Lukosz. Der einfluß der aberrationen auf die optische übertragungsfunktion bei kleinen orts-frequenzen. *Optica Acta*, 10:1–19, 1963.
- [8] J. Braat. Polynomial expansion of severely aberrated wave fronts. *J. Opt. Soc. Am. A*, 4(4):643, 1987.
- [9] J. S. Loomis. Evaluation of optical aberrations in point images. *Appl. Opt.*, 31(13):2211–22, 1992.
- [10] D. Débarre, M. J. Booth, and T. Wilson. Image based adaptive optics through optimisation of low spatial frequencies. *Opt. Express*, 15(13):8176, 2007.
- [11] Y. Tian, K. Shieh, and C. F. Wildsoet. Performance of focus measures in the presence of nondefocus aberrations. *J. Opt. Soc. Am. A*, 24(12):B165, 2007.
- [12] M. Subbarao and T.S. Choi. Focusing techniques. *Proc. SPIE*, 1823, 1992.
- [13] R. Ferzli and L. J. Karam. No-reference objective wavelet based noise immune image sharpness metric. In *IEEE International Conference on Image Processing 2005*, pages I–405. IEEE, 2005.

- [14] J. Kautsky and J. Flusser. A new wavelet-based measure of image focus. *Pattern Recogn. Lett.*, 23:1785–1794, 2002.
- [15] R. A. Muller and A. Buffington. Real-time correction of atmospherically degraded telescope images through image sharpening. *J. Opt. Soc. Am.*, 64(9), 1974.
- [16] A. Buffington, F. S. Crawford, R. A. Muller, and A. J. Schwemin. Correction of atmospheric distortion with an image-sharpening telescope. *J. Opt. Soc. Am.*, 67(3):298–303, 1977.
- [17] N. P. Doble, G. D. Love, D. F. Buscher, R. M. Myers, and A. Purvis. The use of image quality metrics for correction of non-common path errors in the electra adaptive optics system. *Proc. SPIE*, 3749:785–86, 1999.
- [18] M. Langlois, C. Saunter, C. Dunlop, R. Myers, and G. Love. Multiconjugate adaptive optics: laboratory experience. *Opt. Express*, 12(8):1689–99, 2004.
- [19] J. R. Fienup and J. J. Miller. Aberration correction by maximizing generalized sharpness metrics. *J. Opt. Soc. Am. A*, 20(4):609–20, 2003.
- [20] K. N. Walker and R. K. Tyson. Wavefront correction using a Fourier-based image sharpness metric. *Proc. SPIE*, 7468:74680O, 2009.
- [21] M. J. Booth, M.A. Neil, and T. Wilson. Aberration correction for confocal imaging in refractive-index-mismatched media. *J. Microsc.*, 192(2):90–98, 1998.
- [22] P. Marsh, D. Burns, and J. Girkin. Practical implementation of adaptive optics in multiphoton microscopy. *Opt. Express*, 11(10):1123–1130, 2003.
- [23] N. Olivier, D. Débarre, and E. Beaurepaire. Dynamic aberration correction for multiharmonic microscopy. *Opt. Lett.*, 34(20):3145–3147, 2009.
- [24] A. Jesacher, A. Thayil, K. Grieve, D. Débarre, T. Watanabe, T. Wilson, S. Srinivas, and M. Booth. Adaptive harmonic generation microscopy of mammalian embryos. *Opt. Lett.*, 34(20):3154–3156, 2009.
- [25] T. J. Gould, D. Burke, J. Bewersdorf, and M. J. Booth. Adaptive optics enables 3D STED microscopy in aberrating specimens. *Opt. Express*, 20(19):20998–1009, 2012.
- [26] I. Izeddin, M. El Beheiry, J. Andilla, D. Ciepielewski, X. Darzacq, and M. Dahan. PSF shaping using adaptive optics for three-dimensional single-molecule super-resolution imaging and tracking. *Opt. Express*, 20(5):4957–67, 2012.
- [27] D. Débarre, E. J. Botcherby, M. J. Booth, and T. Wilson. Adaptive optics for structured illumination microscopy. *Opt. Express*, 16(13):9290–305, 2008.

- [28] M. Minsky. Microscopy apparatus, 1961.
- [29] Y. A. Rovensky and G. V. Saparin. *Handbook of Biological Confocal Microscopy*. Springer, 3rd edition, 2006.
- [30] M. Göppert-Mayer. Über elementarakte mit zwei quantensprüngen. *Annalen der Physik*, 401(3):273–294, 1931.
- [31] W. Kaiser and C. G. B. Garrett. Two-photon excitation in  $\text{CaF}_2: \text{Eu}^{2+}$ . *Phys. Rev. Lett.*, 7(6):229–232, 1961.
- [32] J. Huiskens and D. Y. R. Stainier. Selective plane illumination microscopy techniques in developmental biology. *Development*, 136(12):1963–75, 2009.
- [33] M. Neil, R. Juskaitis, and T. Wilson. Method of obtaining optical sectioning by using structured light in a conventional microscope. *Opt. Lett.*, 22(24):1905–7, 1997.
- [34] M. J Booth. Adaptive optics in microscopy. *Phil. Trans. R. Soc. A*, 365(1861):2829–43, 2007.
- [35] J. M Girkin, S. Poland, and A. J Wright. Adaptive optics for deeper imaging of biological samples. *Curr. Opin. Biotechnol.*, 20(1):106–10, 2009.
- [36] C. J. R. Sheppard and P. Torok. Effects of specimen refractive index on confocal imaging. *J. Microsc.*, 185(3):366–374, 1997.
- [37] M. J. Booth and T. Wilson. Strategies for the compensation of specimen-induced spherical aberration in confocal microscopy of skin. *J. Microsc.*, 200(Pt 1):68–74, 2000.
- [38] M. Schwertner, M. J. Booth, and T. Wilson. Simple optimization procedure for objective lens correction collar setting. *J. Microsc.*, 217(3):184–7, 2005.
- [39] C. Bourgenot, C. D. Saunter, J. M. Taylor, J. M. Girkin, and G. D. Love. 3D adaptive optics in a light sheet microscope. *Opt. Express*, 20(12):13252–61, 2012.
- [40] M. Schwertner, M. Booth, and T. Wilson. Characterizing specimen induced aberrations for high NA adaptive optical microscopy. *Opt. Express*, 12(26):6540–52, 2004.
- [41] R. Aviles-espinosa, J. Andilla, R. Porcar-guezenec, O. E. Olarte, M. Nieto, X. Levecq, D. Artigas, and P. Loza-alvarez. Measurement and correction of in vivo sample aberrations employing a nonlinear guide-star in two-photon excited fluorescence microscopy. *Opt. Express*, 2(11):1339–1352, 2011.
- [42] X. Tao, B. Fernandez, O. Azucena, M. Fu, D. Garcia, Y. Zuo, D. C. Chen, and J. Kubby. Adaptive optics confocal microscopy using direct wavefront sensing. *Opt. Lett.*, 36(7):1062–1064, 2011.

- [43] N. Ji, Takashi R. Sato, and E. Betzig. Characterization and adaptive optical correction of aberrations during in vivo imaging in the mouse cortex. *Proc. Natl. Acad. Sci. U S A.*, 109(1):22–7, 2012.
- [44] R. Arimoto and J. M. Murray. A common aberration with water-immersion objective lenses. *J. Microsc.*, 216(1):49–51, 2004.
- [45] E. G. Reynaud, U. Kržič, K. Greger, and E. H. K. Stelzer. Light sheet based fluorescence microscopy : More dimensions , more photons , and less photodamage Light sheet-based fluorescence microscopy : more dimensions , more photons , and less photodamage. *HFSP Journal*, 2(5):266–275, 2008.
- [46] A. M. Petzold, V. M. Bedell, N. J. Boczek, J. J. Essner, D. Balciunas, K. J. Clark, and S. C. Ekker. SCORE Imaging : Specimen in a Corrected Optical. *Zebrafish*, 7(2), 2010.
- [47] C. Paterson, I. Munro, and J. Dainty. A low cost adaptive optics system using a membrane mirror. *Opt. Express*, 6(9):175–85, 2000.
- [48] O. Azucena, J. Crest, S. Kotadia, W. Sullivan, X. Tao, M. Reinig, D. Gavel, S. Olivier, and J. Kubby. Adaptive optics wide-field microscopy using direct wavefront sensing. *Opt. Lett.*, 36(6):825–7, 2011.
- [49] X. Tao, J. Crest, S. Kotadia, O. Azucena, D. C Chen, W. Sullivan, and J. Kubby. Live imaging using adaptive optics with fluorescent protein guide-stars. *Opt. Express*, 20(14):15969–82, 2012.
- [50] J. W. Cha, J. Ballesta, and P. T. C. So. Shack-Hartmann wavefront-sensor-based adaptive optics system for multiphoton microscopy. *J. Biomed. Opt.*, 15(4):046022, 2010.
- [51] M. Rueckel, J. A. Mack-Bucher, and W. Denk. Adaptive wavefront correction in two-photon microscopy using coherence-gated wavefront sensing. *Proc. Natl. Acad. Sci. U S A.*, 103(46):17137–42, 2006.
- [52] B. M. Hanser, M. G. L. Gustafsson, D. Agard, and J. W. Sedat. Phase-retrieved pupil functions in wide-field fluorescence microscopy. *J. Microsc.*, 216(Pt 1):32–48, 2004.
- [53] D Débarre, T Vieille, and E Beaurepaire. Simple characterisation of a deformable mirror inside a high numerical aperture microscope using phase diversity. *J. Microsc.*, 244(2):136–43, 2011.
- [54] R. W. Gerchberg and W. O. Saxton. A practical algorithm for the determination of the phase from image and diffraction plane pictures. *Optik*, 35:237–246, 1972.
- [55] L. Sherman, J. Y. Ye, O. Albert, and T. B. Norris. Adaptive correction of depth-induced aberrations in multiphoton scanning microscopy using a deformable mirror. *J. Microsc.*, 206(1):65–71, 2002.

- [56] L. P. Murray. Wavefront correction through image sharpness maximisation. *Proc. SPIE*, 5823:40–47, 2005.
- [57] A. J. Wright, D. Burns, B. a Patterson, S. P. Poland, G. J. Valentine, and J. M. Girkin. Exploration of the optimisation algorithms used in the implementation of adaptive optics in confocal and multiphoton microscopy. *Microsc. Res. Tech.*, 67(1):36–44, 2005.
- [58] M. J. Booth, M. Neil, R. Juskaitis, and T. Wilson. Adaptive aberration correction in a confocal microscope. *Proc. Natl. Acad. Sci. U S A.*, 99(9):5788–92, 2002.
- [59] A. Facomprez, E. Beaurepaire, and D. Débarre. Accuracy of correction in modal sensorless adaptive optics. *Opt. Express*, 20(3):2598–612, 2012.
- [60] M. Booth. Wave front sensor-less adaptive optics: a model-based approach using sphere packings. *Opt. Express*, 14(4):1339–52, 2006.
- [61] P. Vermeulen, E. Muro, T. Pons, V. Lorientte, and A. Fragola. Adaptive optics for fluorescence wide-field microscopy using spectrally independent guide star and markers. *J. Biomed. Opt.*, 16(7):076019, 2011.
- [62] P. Artal, S. Marcos, R. Navarro, and D. R. Williams. Odd aberrations and double-pass. *J. Opt. Soc. Am. A*, 12(2), 1995.
- [63] L. Diaz-Santana and J. C. Dainty. Effects of retinal scattering in the ocular double-pass process. *J. Opt. Soc. Am. A*, 18(7):1437–44, 2001.
- [64] J. Liang, B. Grimm, S. Goelz, and J. F. Bille. Objective measurement of wave aberrations of the human eye with the use of a Hartmann-Shack wave-front sensor. *J. Opt. Soc. Am. A*, 11(7), 1994.
- [65] H. Hofer, P. Artal, B. Singer, J. L. Aragón, and D. R. Williams. Dynamics of the eye’s wave aberration. *J. Opt. Soc. Am. A*, 18(3):497–506, 2001.
- [66] S. L. Jacques, J. R. Roman, and K. Lee. Imaging superficial tissues with polarized light. *Lasers Surg. Med.*, 26(2):119–29, 2000.
- [67] G. J. V. Blokland and D. V. Norren. Intensity and polarization of light scattered at small angles from the human fovea. *Vision res.*, 26(3), 1986.
- [68] V. Albanis, E. N. Ribak, and Y. Carmon. Speckle reduction in ocular wave-front sensing. *Opt. Express*, 428(2002):419–428, 2007.
- [69] D. Ren and B. Dong. Demonstration of portable solar adaptive optics system. *Opt. Eng.*, 51(10):101705–1–101705–4, 2012.
- [70] L. A. Poyneer and B. Macintosh. Spatially filtered wave-front sensor for high-order adaptive optics. *J. Opt. Soc. Am. A*, 21(5):810–819, 2004.

- [71] M. Booth, T. Wilson, H. Sun, T. Ota, and S. Kawata. Methods for the characterization of deformable membrane mirrors. *Appl. Opt.*, 44(24):5131–5139, 2005.
- [72] C. Robert, J.-M. Conan, D. Gratadour, C. Petit, and T. Fusco. Shack-Hartmann tomographic wavefront reconstruction using LGS: analysis of spot elongation and fratricide effect. *1st AO4ELT conference - Adaptive Optics for Extremely Large Telescopes*, 05010, 2010.
- [73] K. J. Jones. NA variability and LGS elongation: impact on wavefront error. *Proc. SPIE*, 8149:81490E–81490E–9, 2011.
- [74] J. Huiskens, J. Swoger, F. Del Bene, J. Wittbrodt, and E. H. K. Stelzer. Optical sectioning deep inside live embryos by selective plane illumination microscopy. *Science*, 305(5686):1007–1009, 2004.
- [75] K. Greger, J. Swoger, and E. H. K. Stelzer. Basic building units and properties of a fluorescence single plane illumination microscope. *Rev. Sci. Instrum.*, 78(2):023705, 2007.
- [76] J. Bakkers. Zebrafish as a model to study cardiac development and human cardiac disease. *Cardiovasc. Res.*, 91(2):279–88, 2011.
- [77] A. J. Hill, H. Teraoka, W. Heideman, and R. E. Peterson. Zebrafish as a model vertebrate for investigating chemical toxicity. *Toxicol. Sci.*, 86(1):6–19, 2005.
- [78] J. M. Taylor, C. D. Saunter, G. D. Love, J. M. Girkin, D. J. Henderson, and B. Chaudhry. Real-time optical gating for three-dimensional beating heart imaging. *J. Biomed. Opt.*, 16(11):116021, 2011.
- [79] J. M. Taylor, J. M. Girkin, and G. D. Love. High-resolution 3d optical microscopy inside the beating zebrafish heart using prospective optical gating. *Biomed. Opt. Express*, 3(12):3043–3053, 2012.
- [80] P. J. Verveer, J. Swoger, and F. Pampaloni. High-resolution three-dimensional imaging of large specimens with light sheet based microscopy. *Nat. Meth.*, 4(4):311–313, 2007.
- [81] J. Mertz. Optical sectioning microscopy with planar or structured illumination. *Nat. Meth.*, 8(10):811–819, 2011.
- [82] E. Baumgart and U. Kubitscheck. Scanned light sheet microscopy with confocal slit detection. *Opt. Express*, 20(19):21805–21814, 2012.
- [83] J. Mertz and J. Kim. Scanning light-sheet microscopy in the whole mouse brain with HiLo background rejection. *J. Biomed. Opt.*, 15(1):016027, 2012.
- [84] J. Huiskens and D. Y. R. Stainier. Even fluorescence excitation by multi-directional selective plane illumination microscopy (mSPIM). *Opt. Lett.*, 32(17):2608–10, 2007.

- [85] F. Fahrbach, P. Simon, and A. Rohrbach. Microscopy with self-reconstructing beams. *Nature Photon.*, 4:0–5, 2010.
- [86] M. Weber and J. Huiskens. Omnidirectional microscopy. *Nat. Methods*, 9(7):656–7, 2012.